



Advancements in the Aerosol Robotic Network (AERONET) Version 3 Database – Automated Near Real-Time Quality Control Algorithm with Improved Cloud Screening for Sun Photometer Aerosol Optical Depth (AOD) Measurements

David M. Giles^{1,2}, Alexander Sinyuk^{1,2}, Mikhail S. Sorokin^{1,2}, Joel S. Schafer^{1,2}, Alexander Smirnov^{1,2}, Ilya Slutsker^{1,2}, Thomas F. Eck^{2,3}, Brent N. Holben², Jasper Lewis^{2,4}, James Campbell⁵, Ellsworth J. Welton², Sergey Korkin^{2,3}, and Alexei Lyapustin²

¹Science Systems and Applications Inc. (SSAI), Lanham, MD 20706, USA

²NASA Goddard Space Flight Center (GSFC), Greenbelt, MD 20771, USA

³Universities Space Research Association (USRA), Columbia, MD 21046, USA

⁴Joint Center for Earth Systems Technology, University of Maryland, Baltimore County, Baltimore, MD 21250, USA

⁵Marine Meteorology Division, Naval Research Laboratory (NRL), Monterey, CA 93943, USA

Correspondence: David M. Giles (David.M.Giles@nasa.gov)



Abstract. The Aerosol Robotic Network (AERONET) provides highly accurate, ground-truth measurements of the aerosol optical depth (AOD) using Cimel Electronique Sun/Sky radiometers for more than 25 years. In Version 2 (V2) of the AERONET database, the near real-time AOD was semi-automatically quality controlled utilizing mainly cloud screening methodology, while additional AOD data contaminated by clouds or affected by instrument anomalies were removed manually before attaining quality assured status (Level 2.0). The large growth in the number of AERONET sites over the past 25 years resulted in significant burden to manually quality control millions of measurements in a consistent manner. The AERONET Version 3 (V3) algorithm provides fully automatic cloud screening and instrument anomaly quality controls. All of these new algorithm updates apply to near real-time data as well as post-field deployment processed data, and AERONET reprocessed the database in 2018. A full algorithm redevelopment provided the opportunity to improve data inputs and corrections such as unique filter specific temperature characterizations for all visible and near-infrared wavelengths, updated gaseous and water vapor absorption coefficients, and ancillary data sets. The Level 2.0 AOD quality assured data set is now available within a month after post-field calibration, reducing the lag time from up to several months. Near real-time estimated uncertainty is determined using data qualified as V3 Level 2.0 AOD and considering the difference between the AOD computed with the pre-field calibration and AOD computed with pre-field and post-field calibration. This assessment provides a near real-time uncertainty estimate where average differences of AOD suggest a +0.02 bias and one sigma uncertainty of 0.02, spectrally, but the bias and uncertainty can be significantly larger for specific instrument deployments. Long-term monthly averages analyzed for the entire V3 and V2 databases produced average differences (V3–V2) of +0.002 with a ± 0.02 standard deviation, yet monthly averages calculated using time-matched observations in both databases were analyzed to compute an average difference of -0.002 with a ± 0.004 standard deviation. The high statistical agreement in multi-year monthly averaged AOD validates the advanced automatic data quality control algorithms and suggests that migrating research to the V3 database will corroborate most V2 research conclusions and likely lead to more accurate results in some cases.



40 1 Introduction

41 Space-based, airborne, and surface-based Earth observing platforms can remotely retrieve or measure aerosol
42 abundance. Each method has its own assumptions and dependencies in which the aerosol total column abundance
43 quantified by aerosol optical depth (AOD) introduces uncertainty in the retrieval or measurement. At the forefront,
44 ground based Sun photometry has been considered the ground truth in the measurement of AOD given minimal
45 assumptions, reliable calibration, and weak dependency on trace gases at carefully selected wavelength bands thus
46 resulting in highly accurate data (Holben et al., 1998). Meanwhile, AOD inferred from other observing platforms
47 such as satellite retrievals provide quantitative AOD but with significantly higher uncertainty (Remer et al., 2005; Li
48 et al., 2009; Levy et al., 2010; Sayer et al., 2013). Further, in situ measurements lack the ability to provide a reliable
49 columnar AOD due to the requirement of measuring aerosols vertically in each layer while not perturbing or
50 modifying the particle properties during the measurement (Redemann et al., 2003; Andrews et al., 2017). Light
51 Detection and Ranging (LIDAR) is fundamental in the determination of the vertical aerosol extinction distribution
52 (Welton et al., 2000; Omar et al., 2013). Quantification of columnar AOD from ground-based LIDAR, for example,
53 may be less reliable due to low signal to noise ratio during the daylight hours at high altitudes and below the overlap
54 region in which the aerosols very near the surface are poorly observed by LIDAR. Satellite retrieval issues include
55 determining the AOD for very high aerosol loading episodes, cloud adjacency effects, land/water mask depiction,
56 surface reflectance, highly varying topography, and aerosol type assumptions (Levy et al., 2010; Levy et al., 2013;
57 Omar et al., 2013). With each of these measurement platforms, uncertainties exist with AOD; however, these
58 concerns are minimized with AOD measurements from surface based Sun photometry such as from the federated
59 Aerosol Robotic Network (AERONET). Ground-based Sun photometry, a passive remote sensing technique, is
60 robust in measuring collimated direct sunlight routinely during the daytime in mainly cloud-free conditions (Shaw
61 1983; Holben et al., 1998). While these surface-based measurements are only point measurements, the federated
62 AERONET provides measurements of columnar AOD and aerosol characteristics over an expansive and diverse
63 geographic area of the Earth's surface at high temporal resolution.

64
65 Standardization of Sun photometer instrumentation, calibration, and freely available data dissemination of AOD and
66 related aerosol databases highlights the success of the federated AERONET. For more than 25 years, the
67 AERONET federation has expanded due to the investments and efforts of NASA (GSFC), University of Lille
68 (PHOTONS/ACTRIS), and University of Valladolid (RIMA/ACTRIS) and other subnetworks (e.g., AEROCAN,
69 AeroSpan, AeroSibnet, CARSNET) and collaborators at agencies, institutes, universities, and individual scientists
70 worldwide. Conceived in the late 1980s, AERONET's primary objective was to provide an aerosol database for
71 validation of Earth Observing System (EOS) satellite retrievals of AOD and atmospheric correction. In addition to
72 columnar direct Sun AOD, sky radiances were used to infer aerosol characteristics initially from Nakajima et al.
73 (1996) (SkyRad.PAK) and later by the Dubovik and King (2000) inversion algorithm to obtain products such as
74 aerosol volume size distribution, complex index of refraction, single scattering albedo, and phase functions.

75



76 AERONET is a network of autonomously operated Cimel Electronique Sun/sky photometers used to measure Sun
77 collimated direct beam irradiance and directional sky radiance and provide scientific quality column integrated
78 aerosol properties of AOD and aerosol microphysical and radiative properties (Holben et al., 1998). The
79 development and growth of the program relies on imposing standardization of instrumentation, measurement
80 protocols, calibration, data distribution and processing algorithms derived from the best scientific knowledge
81 available. This instrument network design has led to a growth from two instruments in 1993 to over 600 in 2018.
82 During that time, improvements were made to the Cimel instruments to provide weather-hardy, robust
83 measurements in a variety of extreme conditions. While the basic optical technology has evolved progressively
84 from analog to digital processing over the past 25 years, the most recent Sun/sky/lunar CE318 Model T instruments
85 provide a number of new capabilities in measurement protocols, integrity, and customizability.

86
87 All of the slightly varying models of the Cimel instruments can have measurement anomalies affecting direct Sun
88 measurements which include measurements in the presence of clouds, various obstructions in the instrument's field
89 of view, or systematic instrumental issues such as electrical connections, high dark currents, and clock shifts to
90 name a few. Some of these issues depend on instrument model and, for more than a decade, these anomalies have
91 been removed semi-automatically utilizing the cloud screening method developed by Smirnov et al. (2000) and
92 further quality controlled by an analyst to remove additional cloud contaminated data and instrument artifacts from
93 the database. Chew et al. (2011) identified up to 0.03 AOD bias at Singapore due to optically thin cirrus clouds for
94 Version 2 Level 2.0 data. Coincidentally, Huang et al. (2011) examined how cirrus clouds could contaminate AOD
95 measurements up to 25% (on average) of the data in April at Phimai, Thailand, in the Version 2 Level 2.0 data set.
96 The number of AERONET sites has increased to more than 600 sites in the network as of 2018 and the labor
97 intensive effort of quality controlling hundreds of thousands of measurements manually had resulted in a significant
98 delay of quality assured data (Level 2.0) in the AERONET Version 2 database.

99
100 With these issues at hand, the cloud screening quality control procedure was reassessed as well as all other aspects
101 of the AERONET processing algorithm including instrument temperature characterization, ancillary data set
102 updates, and further quality control automation. Utilizing these improvements, the Version 3 Level 2.0 quality
103 controlled dataset requires only the pre-field and post-field calibrations to be applied to the data so these data can
104 now be released within a month of the final post-field instrument calibration instead being of delayed up to several
105 months. As encouraged by the AERONET community, automatic quality controls in Version 3 are now also applied
106 to near real-time Level 1.5 AOD products allowing for improved data quality necessary for numerous applications
107 such as numerical weather prediction, atmospheric transport models, satellite evaluation, data synergism, and air
108 quality.

109
110 The AERONET Version 3 processing algorithm marks a significant improvement in the quality controls of the Sun
111 photometer AOD measurements particularly in near real-time. The revised AERONET algorithm is introduced by
112 first reviewing the calculations made to compute the AOD plus changes in the input data sets and the resulting



113 calculation of optical depth components. Next, the preprocessing steps and data prescreening are discussed for the
 114 Version 3 quality control algorithm. Cloud screening and instrument quality control algorithm changes are
 115 discussed with reference to Smirnov et al. (2000), and the solar aureole cirrus cloud screening quality control is
 116 introduced for the first time. The automation of instrument anomaly quality controls and additional cloud screening
 117 is described in the subsequent sections. Lastly, the AERONET Version 2 and Version 3 database results are
 118 analyzed for the entire data set as well as for selected sites.

119 2 Aerosol Optical Depth Computation

120 Sun photometry is a passive remote sensing measurement technique in which mainly collimated light generally not
 121 scattered or absorbed by the atmosphere illuminates a photodiode detector and this light energy is converted to a
 122 digital signal. The digital signal (V) measured by the instrument is proportional to the solar irradiance. The relative
 123 solar calibration is derived from the Langley method (Ångström 1970; Shaw et al., 1973) utilizing the digital counts
 124 from the instrument versus the optical air mass to obtain the calibration coefficient (V_o) by choosing the intercept
 125 where optical air mass is zero at the top of the atmosphere (Shaw, 1983). The relative extraterrestrial solar
 126 irradiance is proportional to V_o . As shown by Holben et al. (1998) and for completeness in this discussion, the Beer-
 127 Lambert-Bouguer law converted to instrument digital counts is shown in Eq. (1):

$$V(\lambda) = V_o(\lambda) * d^2 * \exp[-\tau(\lambda)_{Total} * m], \quad (1)$$

129 where $V(\lambda)$ is the measured spectral voltage of the instrument dependent on the wavelength (λ), $V_o(\lambda)$ is the relative
 130 extraterrestrial spectral calibration coefficient dependent on λ , d is the ratio of the average to the actual Earth-Sun
 131 distance (Michalsky, 1988; USNO, 2018), $\tau(\lambda)_{Total}$ is the total optical depth, and m is the optical air mass, which is
 132 strongly dependent on the secant of the solar zenith angle (Kasten and Young, 1989). For the Cimel Sun
 133 photometer, the voltage signal is expressed as integer digital counts or digital number (DN). The error in the $\tau(\lambda)_{Total}$
 134 is dependent on the optical air mass (m) by $\delta\tau$ proportional to m^{-1} and hence the AOD computation error will be
 135 maximum at $m=1$ (Hamonou et al., 1999). The absolute uncertainty in the AOD measurement can be described as
 136 Eq. (2), with calibration uncertainty of V_o being the overwhelmingly dominant error source:

$$\delta\tau = \frac{1}{m} * \left(\frac{\delta V}{V} + \frac{\delta V_o}{V_o} + \tau * \delta m \right) \cong \frac{1}{m} * \frac{\delta V_o}{V_o} \quad (2)$$

138
 139 The spectral aerosol optical depth (AOD; $\tau(\lambda)_{Aerosol}$) should be computed from the cloud-free spectral total optical
 140 depth ($\tau(\lambda)_{Total}$) and the subtraction of the contributions of Rayleigh scattering optical depth and spectrally dependent
 141 atmospheric trace gases as shown in Eq. (3).

$$\tau(\lambda)_{Aerosol} = \tau(\lambda)_{Total} - \tau(\lambda)_{Rayleigh} - \tau(\lambda)_{H_2O} - \tau(\lambda)_{O_3} - \tau(\lambda)_{NO_2} - \tau(\lambda)_{CO_2} - \tau(\lambda)_{CH_4} \quad (3)$$



143

144 Table 1 provides a list of the spectral corrections used in the calculation of AOD and precipitable water from
 145 935nm. The nominal standard aerosol wavelengths are 340nm, 380nm, 440nm, 500nm, 675nm, 870nm, 1020nm,
 146 and 1640nm. For wavelengths shorter than and equal to 1020nm, these channels are measured using a Silicon
 147 photodiode detector with a spectral range from 320nm to 1100nm. If the Cimel instrument has an InGaAs detector
 148 with a 900nm to 1700nm spectral range, then the 1640nm wavelength is measured along with a redundant 1020nm
 149 measurement used to compare instrument optical characteristics between detectors, lenses, and collimator tubes.
 150 The Cimel SEAPRISM instrument models, which are deployed on ocean or lake platforms as part of the
 151 AERONET-Ocean Color component to retrieve normalized water leaving radiances at 8–12 additional visible band
 152 wavelengths for ocean and lake remote sensing studies, are similarly corrected for atmospheric effects (Zibordi et
 153 al., 2010).

154

155 Rayleigh optical depth calculations require the use of the station pressure (Bodhaine et al., 1999) as well as the
 156 optical air mass (Kasten and Young 1989). To determine AERONET site station pressure (P_s), the NCEP/NCAR
 157 reanalysis mean sea level pressure and geopotential heights at standard levels (1000hPa, 925hPa, 850hPa, 700hPa,
 158 and 600hPa) are fitted by a quadratic function in logarithmic space to infer the station pressure at the corresponding
 159 interpolated geopotential height. The NCEP/NCAR reanalysis data are available routinely at six hourly temporal
 160 resolution and 2.5 degrees spatial resolution (Kalnay et al., 1996). Errors in the station pressure are generally less
 161 than 2hPa when the station elevation is accurate and the weather conditions are benign (i.e., atmospheric pressure
 162 tends to be stable), since aerosol measurements are typically performed in mainly cloud-free conditions.

163

164 The 935nm wavelength is used to determine the water vapor optical depth contribution, which is consequently
 165 subtracted from the longer aerosol wavelengths (i.e., 709nm SEAPRISM, 1020nm, and 1640nm). The AOD at
 166 935nm is extrapolated based on the Ångström exponent (AE) computed from the linear regression of the AOD and
 167 wavelengths in logarithmic space within the range of 440–870nm excluding channels affected by water vapor
 168 absorption (Eck et al., 1999). To extract the precipitable water (PW) in cm from the 935nm measurements, the
 169 Rayleigh optical depth and the AOD components need to be subtracted from the total optical depth at 935nm. As a
 170 result, the dimensionless column water vapor abundance (u) is obtained using the following equations:

171

$$T_W = \ln[T_{935nm[Measured]}] - \ln[T_{935nm[Extrapolated]}] \quad (4)$$

$$-\ln[T_W] = \ln[V_{o\ 935nm} * d^{-2}] - \ln[V_{935nm}] - m * (\tau_{935nm\ AOD} + \tau_{935nm\ Rayleigh}) \quad (5)$$

$$\ln\left[\frac{T_W}{C}\right] = -A * (m_W * u)^B \quad (6)$$



$$u = \frac{\left[\frac{\ln T_W}{-A} \right]^{1/B}}{m_W} \quad (7)$$

172

173 where T_W is the water vapor transmission and constants A and B are absorption constants unique to the particular
174 935nm filter, C is an absorption constant assumed to be equal to one (Ingold et al., 2000), d and m are defined in Eq.
175 (1), m_W is the water vapor optical air mass (Kasten et al., 1965), and u is the total column water vapor abundance
176 (Schmid et al., 2001; Smirnov et al., 2004). The total column water vapor abundance (u) is converted to total
177 column water content or PW by using the normalization factor ($u_o=10 \text{ kg/m}^2$) and dividing it by the mean value of
178 water density ($p_o=1000 \text{ kg/m}^3$) to obtain water column height units of cm (Bruegge et al., 1992; Ingold et al., 2000).

179

180 In the calculation of the filter dependent A and B constants, the water vapor absorption optical thickness is
181 determined by the integration of water vapor extinction coefficient over height from the bottom to the top of the
182 atmosphere. This calculation requires the following inputs to determine the extinction at each height: HITRAN
183 spectral lines with assumed US1976 model standard atmosphere temperature and pressure profiles; the absorption
184 continuum look up table from the Atmospheric and Environmental Research (AER) Radiative Transfer Working
185 Group (Clough et al., 1989; Mlawer et al., 2012); and Total Internal Partition Sums that define the shape and
186 position of lines dependent on temperature (Gamache et al., 2017). Nine defined total column water vapor amounts
187 (0.5 cm, 1.0 cm, 1.5 cm, 2.0 cm, 2.5 cm, 3.0 cm, 4.0 cm, 5.0 cm, and 6.5 cm) are used to generate water vapor
188 absorption optical depth lookup tables. From these lookup tables, transmittances are calculated based on the
189 bandpass and averaged spectral solar irradiance for the quiet Sun obtained from the University of Colorado
190 LASP/NRL2 model (Coddington et al., 2016) to generate filter-specific A and B coefficients. The one sigma
191 uncertainty in the calculation of PW in cm is expected to be less than 10% compared to GPS precipitable water
192 retrievals (Halthore et al., 1997). The spectral water vapor optical thickness ($\tau_{H_2O}(\lambda)$) is determined by computing
193 the average of all A and B constants from the suite of filters affected by water vapor absorption (i.e., 709nm
194 SEAPRISM, 935nm, 1020nm, and 1640nm) in the AERONET database. The $\tau_{H_2O}(\lambda)$ is also dependent on the
195 dimensionless total column water vapor abundance (Michalsky et al., 1995; Schmid et al., 1996):

196

$$\tau_{H_2O}(\lambda) = \bar{A}(\lambda) + \bar{B}(\lambda) * u \quad (8)$$

197

198 The contribution of ozone (O_3) optical depth is determined utilizing the total column Total Ozone Mapping
199 Spectrometer (TOMS) monthly average climatology (1978–2004) of O_3 concentration at $1.00^\circ \times 1.25^\circ$ spatial
200 resolution, the O_3 optical air mass using O_3 scale height adjustment by latitude (Komhyr et al., 1989), and the O_3
201 absorption coefficient (Burrows et al., 1999). The OMI O_3 data set is not used here due to instrument sampling
202 anomalies (McPeters et al., 2015). While the TOMS O_3 data set is extensive and generally characterizes the
203 distribution of O_3 , recent changes in concentration could introduce some minor uncertainty in AOD. Similarly, the
204 nitrogen dioxide (NO_2) optical depth is calculated using the total column OMI monthly average climatology (2004–
205 2013) of NO_2 concentration at $0.25^\circ \times 0.25^\circ$ spatial resolution and the NO_2 absorption coefficient (Burrows et al.,



1998). Tropospheric NO₂ is highly variable spatially due to various source emissions and stratospheric NO₂ concentrations are more stable spatially than the tropospheric NO₂ (Boersma et al., 2004), therefore, regions with high tropospheric NO₂ emission will tend to have greater proclivity for deviating from climatological means. Further, NO₂ can vary significantly on the diurnal scale (Boersma et al., 2008). Improved satellite observations, models, or collocation with surface-based PANDORA instruments measuring temporal total column O₃ and NO₂ may assist in reducing the uncertainty and determination of the total column NO₂ optical depth contribution in later versions of the algorithm (Herman et al., 2009; Tzortziou et al. 2012). Concentrations for carbon dioxide (CO₂) and methane (CH₄) are assumed constant and optical depths are computed based on the HITRAN-derived absorption coefficients of 0.0087 and 0.0047 for the 1640nm filter, respectively, and adjusted to the station elevation.

The calibration of the AOD measurements is traced to a Langley measurement performed by a reference instrument. The reference instruments obtain a calibration based on the Langley method morning only analyses based on typically 4 to 20 days of data performed at a mountaintop calibration sites. The primary mountaintop calibration sites in AERONET are located at Mauna Loa Observatory (19.536° N, 155.576° W, 3402 m) on the island of Hawaii and Izana Observatory (28.309° N, 16.499° W, 2401 m) on the island of Tenerife in the Canary Islands (Toledano et al., 2018). These reference instruments are routinely monitored for stability and typically recalibrated every three to eight months. Reference instruments rotate between mountaintop calibration sites and inter-calibration facilities at NASA GSFC (38.993° N, 76.839° W, 87 m) in Maryland, Carpentras (44.083° N, 5.058° E, 107 m) in France, and Valladolid (41.664° N, 4.706° W, 705 m) in Spain, where reference instruments operate simultaneously with field instruments to obtain pre-field and post-field deployment calibrations. For periods when the AOD is low ($\tau_{440nm} < 0.2$), optical air mass is low ($m < 2$), and aerosol loading is stable, the reference Cimel calibration may be transferred to field instruments (Holben et al., 1998).

The Version 2 processing used default temperature corrections based on three sensor head temperature (T_S) ranges ($T_S < 21^\circ\text{C}$, $21^\circ\text{C} \leq T_S \leq 32^\circ\text{C}$, and $T_S > 32^\circ\text{C}$) using a constant nominal temperature sensitivity only for the 1020nm filter direct Sun measurements. In Version 3, measurement temperature sensitivity has been updated for all wavelengths $\geq 400\text{nm}$ and all measurement types (i.e., direct solar, sky, water, and lunar viewing measurements). Beginning in 2010, the temperature sensitivity was characterized for almost all wavelengths uniquely for each Cimel instrument. The temperature effect on signal is a function of the combined sensitivity of the detector and the filter material itself. If any Cimel data relying on a filter was in use prior to 2010 and the filter was not temperature characterized, then the default values for the filter and manufacturer type are applied, if established. Filters in the ultraviolet (i.e., 340nm and 380nm) are not measured for temperature dependence because of low integrating sphere radiance output at these wavelengths. Due to temperature dependence of the field instrument and the reference instrument, the Sun and sky calibration transfer needs to be adjusted by computing the ratio of the Cimel temperature coefficients for each wavelength and for the temperature observed at the time of the calibration. In addition, when the AOD is computed for field instruments, the sensor head temperature is measured for each direct Sun measurement so these



242 data can be adjusted to the temperature response of the instrument optics (i.e., combined effect of the detector and
243 filters) and electronics.

244

245 The temperature response is measured at the AERONET calibration facilities using an integrating sphere and a
246 temperature chamber where the temperature is varied from -40°C to $+50^{\circ}\text{C}$. The wavelength dependent
247 temperature coefficient is typically determined from the slope of ordinary least squares regression fit of the digital
248 voltage counts versus the sensor head temperature reading. For this relationship, the second order polynomial fit is
249 computed for 1020nm, while other filters use either a linear or second order polynomial fit (depending on the larger
250 correlation coefficient). For Cimel Model 4 and some Model 5 instruments with two Silicon photodiode detectors,
251 the digital counts for solar aureole and sky instrument gains are used to determine temperature coefficients for each
252 detector. Some Model 5 and all Model T instruments perform the direct Sun and sky measurements on the same
253 detector (Silicon or InGaAs) and typically utilize the solar aureole gain digital counts.

254

255 According to Holben et al. (1998), all instruments generally perform measurements sequentially from longer
256 wavelength to the shortest wavelength filters on a rotating filter wheel inside the sensor head, which positions each
257 filter in front of the photodiode detector and behind the sensor head lenses and collimator tube. The robotically
258 controlled sensor head points automatically at the Sun based on the time and geolocation of the instrument. The
259 laboratory tuned 4-quadrant detector provides nearly perfect solar and lunar tracking to one motor step or $\sim 0.1^{\circ}$
260 immediately following the geographic pointing. A dual tube external collimator with internal baffles attached to the
261 top of the sensor head reduces stray light effects into the sensor head 1.2° field of view optical train.

262

263 The instrument performs measurements of the Sun using measurement triplets, that is, performing the series of
264 measurements of all filters at time hh:m0:00 (time notation for hours, minutes, seconds), where for duration of about
265 eight seconds, and then repeating these measurements at hh:m0:30 and hh:m1:00. The resulting one-minute
266 averaged measurement sequence is defined as a triplet measurement and the maximum to minimum range of these
267 measurements is termed the triplet variability. The triplet measurement advantageously allows for separation of
268 homogeneously dispersed aerosols versus highly temporally variable clouds. The triplet measurements are
269 performed either every 15 minutes for older Model 4 instruments or every three minutes for newer Model 5 and
270 Model T instruments increasing the temporal availability of the AOD measurements in the AERONET database.

271 3 Automatic Quality Controls of Sun Photometrically Measured Aerosol Optical Depth

272 The AERONET database has provided three distinct levels for data quality: Level 1.0, Level 1.5, and Level 2.0. In
273 Version 2, Level 1.0 was defined as prescreened data, Level 1.5 represented near real-time automatically cloud-
274 cleared data, and Level 2.0 signified automatically cloud-cleared, manually quality controlled data set with pre and
275 post-field calibrations applied. In Version 3, the definitions have been modified substantially for Level 1.5 and
276 Level 2.0. Version 3 Level 1.5 now represents near real-time automatic cloud screening and automatic instrument
277 anomaly quality controls and Level 2.0 additionally applies pre-field and post-field calibrations. The Version 3 fully



278 automated cloud screening and quality control checks eliminate the need for manual quality control and cloud
279 screening by an analyst and increases the timeliness of quality assured data. Note that in all cases each subsequent
280 data quality level requires the previous data level to be available as input (e.g., Level 1.5 requires Level 1.0 and
281 Level 2.0 requires Level 1.5). The following sections will describe these new definitions and automatic quality
282 controls in detail and the impact these new quality assurance measures have on the AERONET database.

283

284 3.1 Preprocessing Steps and Prescreening

285 Most preprocessing data quality criteria operate on voltage (V, expressed as the integer digital number (DN)) or
286 sensor head temperature (T_s). The impact of these conditions may immediately remove data from Level 1.0
287 consideration or later only impact Level 1.5 and Level 2.0 AOD. Each quality control section describes the
288 reasoning for the screening at the specified data quality level. Digital count anomalies typically result from
289 anomalous electronic issues such as very low or high battery voltages, malfunctioning amplifiers, or loose
290 connections of internal control box components. These digital count anomalies mostly affect older instruments
291 (Cimel Models 4 (CE318-1) and 5 (CE318N)), while several of these connection issues have been mitigated in the
292 newest instruments (Cimel Model T (CE318-T)).

293 3.1.1 Electronic Instability

294 Cimel Model 4 instruments use a 16-bit analog/digital (A/D) converter in the processing unit in which the analog
295 signal from the sensor head detector to the control box is subject to electronic noise. Cimel Model 5 instruments use
296 a 16-bit A/D converter inside the sensor head and the instrument invokes electronic chopping to reduce electronic
297 noise. Cimel Model T instruments utilize an increased quantization from 16 bits to 24 bits, which significantly
298 reduces noise effects. Cimel Model 5 and Model T instruments internally adjust for the dark current (V_D) with each
299 measurement and no separate record is logged. Cimel Model 4 instruments perform V_D measurements after each
300 sky scan (approximately hourly) for each spectrally dependent instrument gain parameter (i.e., Sun, aureole, and
301 sky). Large V_D values generally represent significant instrument electronic instability. Quality controls applied to the
302 V_D will remove the entire day for Model 4 instrument data from all of the quality levels for either of the following
303 conditions: 1) a single dark current measurement is greater than 100 counts for greater than N-1 wavelengths, where
304 N is the total number of wavelengths or 2) more than three dark current measurements are greater than 100 counts
305 for three or more wavelengths.

306

307 Amplifiers in the Cimel Model 4 instruments can produce unphysical increases in the digital counts or decreases in
308 the AOD for the 340nm and 380nm wavelengths at large optical air mass (Fig. 1). These instability issues are
309 evaluated simply using a relative threshold with respect to the available visible wavelength AOD measurements. If
310 the τ_{380} is greater than $0.5 * \tau_{340}$ and ($\tau_{440} + \tau_{500 \text{ or } 675} < \tau_{380} + \tau_{340} - 2.0$), then the triplet measurements for 340nm and
311 380nm are removed from the database for Level 1.5 and subsequent levels. These quality controls are limited to
312 Model 4 instruments that were not manufactured after 2001; however, the early AERONET database (1993–2005)



contains much of these data. New Cimel Model T instruments are replacing Model 4 instruments but over 40 Model 4 instruments remain active in 2018.

The instrument may rarely malfunction by producing constant digital voltages for triplet measurements and the result of keeping these data in the database leads to unphysical variations in the AOD. A frequency analysis is performed to determine if any digital number (DN) values occur more than 10 times in a day. If more than 50% of the DNs are from the same triplet measurement, then this measurement is identified as an anomalous measurement. If more than 50% of the triplet measurements in the day are considered anomalous, then the entire day will be removed from Levels 1.5 and 2.0.

3.1.2 Radiometer Sensitivity Evaluation

The Cimel 4-quadrant solar near infrared detector requires enough sensitivity to track the Sun and a DN threshold of 100 in the near infrared is needed to have sufficient signal. Near infrared wavelengths (e.g., 1020nm) typically have a higher measured solar DN(V) due to higher atmospheric transmission in the presence of fine mode dominated aerosols even in very high aerosol loading conditions. When the DN ($V_{870\text{nm}}$ or $V_{1020\text{nm}}$) is less than 100 counts for any measurement of the solar triplet, then the entire solar triplet AOD will be removed for all wavelengths from Level 1.0 and subsequent levels due to potential solar tracking accuracy issues.

Version 2 data processing assessed the instrument electronic and diffuse light sensitivity by defining a digital number (DN) of 10 to remove solar AOD triplet measurements. Electronic issues impact Cimel Model 4 instruments in the UV and short visible wavelengths due to high DN(V_D). Scattered diffuse light into the collimated field of view can affect all instruments and produce unusual AOD changes with optical air mass especially when the aerosol loading is high and optical air mass is large. The signal to noise ratio of the Cimel instrument requires setting a minimum threshold for the determination of the solar measured DN(V) to limit the effect of diffuse radiance in the instrument field of view (Sinyuk et al., 2012). When a dark current DN(V_D) (e.g., ~50–100) is nearly equal to or larger than the measured solar DN(V) (e.g., ~25–50) will result in V and τ decreasing with increasing optical air mass. All wavelengths are evaluated to determine if the measured solar DN(V) (subtracted from the closest temporal dark current DN(V_D) for Model 4 instruments only) is less than DN(V_O)/1500, then the identified wavelength will be removed from all AOD levels. A threshold of 1500 is calculated from a DN of 15000, a typical average DN(V_O) for Cimel Models 4 and 5, normalized to a minimum signal DN of 10. The maximum product of AOD times optical air mass ($\tau_m = \tau * m$) of approximately 7.3 is computed by the natural logarithm of 1500 (i.e., $\ln(15000/10)$) for Cimel Model T instruments. For non-Model T instruments, the 100 DN threshold for 870nm and 1020nm limits the τ_m to approximately 5.0 (i.e., $\ln(15000/100)$) for only those two wavelengths. The τ_m maximum threshold applies to all channels; however, the signal count can decrease significantly with optical air mass and depend on the wavelength dependence of V_O . For values exceeding the τ_m maximum threshold, the diffuse radiation increases the signal and, as a result, unfiltered AODs show a decrease in magnitude as optical air mass increases for



high AOD even when $DN(V_D)$ equals zero. A measured solar $DN(V)$ lower than the ratio $DN(V_O)/1500$ threshold will result in the removal of the solar triplet AOD for the specific wavelength (Fig. 2).

3.1.3 Digital Voltage Triplet Variance

As mentioned in Sect. 2, the Cimel instrument performs a direct Sun triplet measurement at regular intervals throughout the day. A variance threshold is applied based on the root mean square (RMS) differences of the triplet measurements relative to the mean of these three values. If the $(RMS/mean)*100\%$ of the triplet values is greater than 16%, then these data are not qualified as Level 1.0 AOD (Eck et al., 2014). The temporal variance threshold is sensitive to clouds with large spatial-temporal variance in cloud optical depth and optically thick clouds such as cumulus clouds as well as issues due to poor tracking of the instrument.

3.1.4 Sensor Head Temperature Anomaly Identification

Each Cimel instrument has a fixed resistance (Model 4) or band gap (Models 5 and T) temperature sensor inside the optical head within 0.5 cm of the detector, filter wheel, and optical train assembly. As discussed in Sect. 2, the instrument optics and digital counts can have dependence to the sensor head temperature (T_S) which is saved with each measurement triplet. Sensor head temperatures may be erroneous due to instrument electronic instability or communication issues. These potentially unphysical values of T_S are evaluated by a number of algorithm steps such as checks for 1) constant T_S values, 3) unphysical extreme high or low T_S , 4) potentially physical yet anomalously low T_S with respect to the NCEP/NCAR reanalysis ambient temperatures, and 5) unphysical T_S decreases or increases (dips). When the algorithm removes a T_S reading or the T_S measurement is missing, an assessment is made on the instrument temperature response based on $\pm 15^\circ\text{C}$ of the NCEP/NCAR reanalysis temperature for the date and location to determine whether the temperature characterization coefficient for a specific wavelength would result in a change of AOD by more than 0.02. If this condition is met for a specific wavelength, then data associated with this wavelength-specific triplet measurement will be removed at Level 1.5 and subsequent levels while preserving other less temperature dependent spectral triplet measurements.

3.1.5 Eclipse Circumstance Screening

During episodic solar or lunar eclipses, AOD will increase to the maximum obscuration of the eclipse at a particular location on the Earth's surface. The AOD increases due to the reduction of the irradiance due to the celestial body (Moon or Earth) obscuring the calibrated light source (Sun or Moon). While any one point on Earth infrequently experiences an eclipse, when an eclipse episode does occur, the eclipse can affect many locations nearly simultaneously making manual removal tedious at sites distributed globally. To automate the removal of eclipse episodes, the NASA solar and lunar eclipse databases are queried for eclipse circumstances based on geographic position of the site to produce a table of eclipse episodes starting from 1992. The eclipse tool utilizes established Besselian elements based on the Five Millennium Canon of Solar Eclipses: -1999 to +3000 (Espenak and Meeus 2006) to quantify the geometric and temporal position of the celestial bodies (Sun, Earth, and Moon), determine the type of eclipse (e.g., partial, annular, total), and predict times of the various stages of the solar or lunar eclipse. For



the Version 3 database, the eclipse site-specific tables are used to discretely remove triplet measurements affected by any stage of the eclipse circumstance. For example, during a solar eclipse, solar triplets will be removed between the partial eclipse first contact to the partial eclipse last contact regardless of the eclipse obscuration or magnitude for Level 1.5 data and subsequent levels (Fig. 3). The partial eclipse first contact is defined as the time at which the penumbral shadow is visible at a point on the Earth's surface and the partial eclipse last contact is defined as the time at which the penumbral shadow is no longer visible a point on the Earth's surface. Efforts to retain AOD during solar eclipse episodes have been attempted by the authors in which up to 95% of the AOD can be corrected based on adjusting calibration coefficients by the eclipse obscuration. However, spectral calibration coefficients also need to be adjusted to account for the solar atmosphere spectral irradiance, which becomes more dominant during the solar eclipse episode and is a topic of further investigation.

3.1.6 Very High AOD Retention

Cloud screening procedures in the next section may inadvertently remove aerosol in very high aerosol loading cases due to biomass burning smoke and urban pollution as discussed by Smirnov et al. (2000). For Version 3, each triplet reaching Level 1.0 is evaluated for possible retention in the event that a specific Level 1.5 cloud screening procedure removes the triplet. When the AOD measurement for 870nm is >0.5 and AOD 1020nm >0.0 , these conditions will potentially qualify the triplet for very high AOD retention. Further analysis is performed on those qualified triplets to remove the effect of heavily cloud-contaminated data using the AE for the wavelength ranges of 675–1020nm or 870–1020nm (Eck et al., 1999). If the $AE_{675-1020nm} > 1.2$ (or $AE_{870-1020nm} > 1.3$, if AOD_{675nm} is not available), and the AE for the same range is less than 3.0, then the triplet qualifies for very high AOD retention and the triplet can be retained at Level 1.5 even if the measurement does not pass Level 1.5 cloud screening quality control steps in Sect. 3.2.

3.1.7 Total Potential Daily Measurements

Cloud screening methods in Sect. 3.2 may incompletely remove all cloud-contaminated points and leave data fragments. To mitigate this issue, a methodology was developed based on the total number of potential measurements in the day and calculated AE values. The total number of potential measurements in the day is defined as the number of triplet measurements plus the number of humidity status reports (i.e., wet sensor activations). If the number of remaining measurements after all screening steps in Sect. 3.2 are performed is less than three measurements or 10% of the potential measurements (whichever is greater), then the algorithm will remove the remaining measurements. This condition is repeated after each cloud screening step in Sect. 3.2 and will only be activated when the very high AOD restoration is not triggered (see Sect. 3.1.6) or when the $AE_{440-870nm}$ is less than 1.0 for a triplet measurement indicating large particles such as clouds may contaminate the remaining measurements.



414 3.1.8 Optical Air Mass Range

415 The basic Cimel Sun photometer Sun and sky measurement protocols were specified to NASA requirements in
 416 Hoblen et al. (1992, 1998, and 2006), and have only been slightly modified since that time for improved
 417 measurement capability of the Model 5 and Model T instruments. All instruments systematically perform direct Sun
 418 measurements between the optical air mass (m) of 7.0 in the morning and m of 7.0 in the evening. In Version 2 and
 419 earlier databases, AERONET data processing limited the Level 1.5 and Level 2.0 AOD computation from m of 5.0
 420 in the morning to m of 5.0 in the evening. The m limitation may avoid potential error in the computation of the
 421 optical air mass at large solar zenith angles (Russell et al., 1993) and possible increased cloud contamination
 422 (Smirnov et al., 2000). For Version 2 and 3 processing, the Kasten and Young 1989 formulation was used to
 423 account for very small differences in the optical air mass calculations at high solar zenith angles. Noting that the
 424 AOD error ($\delta\tau/m$) has a minimum at large m (conversely a maximum at solar noon), the maximum m of 5.0 was
 425 extended to m of 7.0 in Version 3 processing. The larger optical air mass range leads to an increase in the number of
 426 solar measurements occurring in the early morning and the early evening contributing to additional AOD
 427 measurements used for input for almucantar and hybrid inversions plus an increase in AOD measurement at high
 428 latitude sites when solar zenith angles may be large even at solar noon. The impact on the cloud screening
 429 performance appears to be minimal for measurements closer to the horizon. The fidelity of the Version 3 cloud
 430 screening (see Sect. 3.2) AODs supports the extended optical air mass range for Level 2.0.

431 3.2 Level 1.5 AOD Cloud Screening Quality Controls

432 As discussed in Sect. 3.1, several preprocessed criteria and parameters are necessary to quality control the AOD data
 433 quality in near real-time (NRT). Cloud screening procedures proposed by Smirnov et al. (2000) were designated to
 434 remove or reduce cloud contaminated AOD measurements. However, these procedures also had the effect of
 435 surreptitiously removing occasionally other non-cloud anomalies such as repeated AOD diurnal dependence when
 436 AOD had a large maximum at midday and minimum at high optical air masses due to environmental impacts on the
 437 optical characteristics of the instrument (e.g., moisture on the sensor head lens or spider webs in the collimator
 438 tube). While these cloud screening methods have been implemented for about 25 years, the state of knowledge has
 439 progressed over this period and thus necessitates review and modification of cloud screening quality control
 440 procedures (Kaufman et al. 2005, Chew et al., 2011; Huang et al., 2011). The calculation of the AOD at Level 1.0
 441 essentially represents the following in Eq. (9):

$$442 \tau_{app\ Total} = \frac{1}{\Gamma_{anomaly}} \left(\tau_{aerosol} + \frac{\tau_{cirrus}}{C_{cirrus}} + \tau_{liquid\ cloud} + \tau_{eclipse} \right) \quad (9)$$

443
 444 where $\tau_{app\ Total}$ is the apparent total optical depth, which at this point in the data processing, may be affected by the
 445 contributions of liquid cloud droplets ($\tau_{liquid\ cloud}$), cirrus amplification factor (C_{cirrus}) applied to the cirrus crystal
 446 optical depth (τ_{cirrus}) due to strong forward scattering into the field of view of the instrument, solar or lunar eclipses
 447 ($\tau_{eclipse}$), and instrument anomalies ($\Gamma_{anomaly}$ adjustment factor). Given cloud free conditions and perfect instrument



operation, the additional non-aerosol τ components would be zero and C_{cirrus} and Γ_{anomaly} would be one. However, the Cimel Sun photometer always attempts to measure the Sun if it can be tracked regardless of the total optical depth magnitude.

Clouds are a major factor in the effort to quality control remotely sensed aerosol data (Smirnov et al. 2000; Martins et al. 2002; Kaufman et al., 2005; Chew et al., 2011; Kahn and Gaitley 2015). A significant portion of the liquid cloud contribution is removed by the prescreening prior to Level 1.0 as discussed in Sect. 3.1.3. The $\tau_{\text{app Total}}$ should be adjusted based on a multiplier dependent on the cirrus crystal size ($\tau_{\text{correct}} = C_{\text{cirrus}} * \tau_{\text{app Total}}$) according to Kinne et al. (1999). While this cirrus coefficient (C_{cirrus}) is not specifically modelled by Kinne et al. (1999) for the Cimel instrument field of view half angle of 0.6° , this multiplier is likely to be close to one for small cirrus crystals (e.g., $r_{\text{eff}} = 6\mu\text{m} - 16\mu\text{m}$), but near two for larger cirrus crystal sizes (e.g., $r_{\text{eff}} = 25\mu\text{m} - 177\mu\text{m}$). These adjustment factors would result in the reduction of the $\tau_{\text{app Total}}$ due to forward scattering in the presence of cirrus. On the other hand, liquid water cloud droplets would significantly increase the $\tau_{\text{app Total}}$ in a manner similar to large dust particles.

Cimel instruments also may have internal and external anomalous conditions that modify the optical characteristics or response of the instrument resulting in amplification or dampening impacts (Γ_{anomaly}) of varying magnitudes on the computation of the $\tau_{\text{app Total}}$. These anomaly adjustments can be difficult to quantify and can have strong dependence on optical air mass (m) or the sensor head temperature (T_s). As a result, the following sections will describe the mechanisms in which these additional cloud and anomaly components are automatically eliminated or reduced as close to zero as possible to provide a quality assured AOD (τ_{aerosol}) after final calibration is applied (see Sect. 4) across the global AERONET database.

3.2.1 Cloud Screening Quality Controls

As Level 1.0 AOD data may have cloud contamination, these data should be considered as potentially cloud contaminated where the triplet measurement represents the apparent AOD ($\tau_{\text{app aerosol}}$) as defined in the previous section. Table 2 provides a summary of the cloud screening quality control changes from Version 2 to Version 3 and these changes are discussed in detail below and Sect. 3.2.2.

Cimel triplet measurements are performed typically every three minutes (every 15 minutes for older instrument types) and these triplet measurements can detect rapid changes in the $\tau_{\text{app aerosol}}$ by analyzing the maximum to minimum variability (i.e., the $\Delta\tau_{\text{app aerosol}}\{\text{MAX-MIN}\}$). Assuming that spatial and temporal variance of aerosols plus clouds is much greater than aerosols alone, in many cases, $\Delta\tau_{\text{aerosol}}$ would be near zero and $\Delta\tau_{\text{cloud}}$ should be much larger than zero when especially liquid phase cloud droplets exist. For Version 2 and earlier databases, Smirnov et al. (2000) methodology utilized all available wavelengths to perform $\tau_{\text{app aerosol}}$ triplet screening for cloud contamination. Therefore, large triplet variability would indicate the presence of clouds due to large $\Delta\tau_{\text{cloud}}$. Analyses (e.g., Eck et al., 2018) have shown that removing the entire triplet measurement when only one or more of the shorter wavelengths indicates a large variation ($\Delta\tau_{\text{aerosol}}(\lambda)$ much greater than zero) may not be the most robust



approach. For example, in cases of highly variable fine mode aerosols such as smoke can produce large triplet variability as a result of the inhomogeneous nature of the aerosol plume especially for shorter wavelengths (e.g., 340nm, 380nm, 440nm) where fine mode dominated aerosol particles can have radii similar to short wavelength measurements.

Considering these factors, several potential techniques were explored utilizing various wavelength combinations and utilizing the Spectral Deconvolution algorithm (SDA) fine and coarse mode triplet separation (O'Neill et al., 2001, 2003). While the SDA algorithm derived triplets for coarse mode AODs relative change tended to show utility in cloud removal, the SDA algorithm itself could not be applied universally to the AERONET database to due anomalous results in which fine and coarse mode AODs can have a negative relationship when the number of available wavelengths or wavelength range is not satisfied. Anomalies in SDA retrievals can occur when the uncertainty in AOD is relatively large near solar noon compared to the magnitude of AOD as is sometimes the case when only the pre-field deployment calibration has been applied. Upon further consideration of the triplet variability technique, analyses indicated that using the three longest standard AERONET wavelengths (i.e., 675nm, 870nm, 1020nm) could be used to remove a triplet measurement when they have high triplet variability that exceeds 0.01 or $0.015 \times \text{AOD}$ (whichever is greater). The reduction in the threshold of the triplet variability criterion is proportional to the magnitude decrease AOD uncertainty compared to UV wavelengths (0.02) to those of visible and near infrared wavelengths (0.01).

While Smirnov et al. (2000) did not impose an Ångström exponent limitation; Version 3 processing constrains the $\text{AE}_{440-870\text{nm}}$ of Level 1.5 data to be within -1.0 and $+3.0$. In general, the $\text{AE}_{440-870\text{nm}}$ values outside this range are unphysical and should not be used due to the inconsistency of the AOD spectral dependence. These inconsistencies typically occur at very low optical depth (<0.05) where the uncertainty of the AOD may be up to 100% of the actual value thus producing AE values that are invalid.

The AOD time series smoothness uses a number of numerical methods and fits dependent on the application. For an AOD time series, rapid and large increases are usually the result of cloud contamination. In Version 2 and prior versions, a technique proposed by Smirnov et al. (2000) to implement a smoothness methodology similar to Dubovik et al. (1995). In this scheme, the triplet measurements were considered as discrete points and differences in logarithm of $\tau_{\text{app aerosol}}$ and relative difference in times between those measurements were utilized to calculate the first derivative differences in which an arbitrary parameter D (similar to the norm of the second derivative) is calculated. In Version 2 and earlier versions, when the value of D was greater than 16 for an AOD measurement time sequence for 500 nm or 440nm, then this triplet was removed from the data set. Further, the smoothness procedure was repeated or measurements were rejected for the day if less than three triplets remained for the day as discussed in Smirnov et al. (2000). While the $D=16$ threshold was empirically derived, the smoothness parameter is somewhat arbitrary in origin and operates in logarithmic coordinates rather than natural ones. For example, the distribution of aerosol measurements in a single day is typically normally distributed rather than logarithmically



distributed. Further, the D parameter smoothness procedure was not always successful at removing cloud-contaminated data and this may be related to the fact that the empirically derived D parameter was tuned for 15-minute triplet measurement intervals rather than three-minute intervals now commonly observed in the network. Therefore, an approach adhering to the relative change in the total optical depth with time is feasible and a more straightforward physical quantification of the change in $\tau_{\text{app aerosol}}$ with time.

The AOD time series smoothness in Version 3 evaluates the same $\tau_{\text{app aerosol}}$ 500nm wavelength (or 440nm if 500nm is not available). The Version 3 smoothness method computes the relative rate of change of $\tau_{\text{app aerosol}}$ per minute and if $\Delta\tau_{\text{app aerosol}}/\Delta t > 0.01$ per minute, then the larger triplet measurement in the pair is removed and the smoothness procedure will continue to remove triplets until measurement pairs in the day do not surpass the smoothness threshold. The selection of this threshold of 0.01 per minute hinges on the premise that the triplet average does not change rapidly within one minute. The Version 3 smoothness procedure could be affected by extreme changes in AOD due to anomalous aerosol plumes (e.g., biomass burning or desert dust plumes) where no temporal gradient exists.

After the cirrus cloud screening quality control (to be discussed in the Sect. 3.2.2), triplets are evaluated for spurious or isolated measurements remaining during the day after applying the cloud screening quality control procedures. So-called “standalone points” may be relevant given the ability of the instrument to perform measurements in cloud breaks or gaps. Here, the definition of a standalone triplet is when no triplets are available within 1 hour of the measurement. If the $AE_{440-870\text{nm}}$ is greater than 1.0, the algorithm retains the triplet measurement; otherwise, the measurement will be removed from the data set. Finally, daily averaged data are evaluated for temporal stability using the AOD stability during the day at 500nm (or 440nm) and daily outlier triplets using the 3-sigma check for AOD at 500nm (or 440nm) and $AE_{440-870\text{nm}}$ to be within ± 3 standard deviations (Smirnov et al. 2000). At this point in the quality control algorithm, the remaining triplet measurements are not expected to have a major component of τ_{cloud} or τ_{cirrus} .

3.2.2 Novel Cirrus Removal Method Utilizing Solar Aureole Curvature

Utilizing satellite and surface-based LIDAR, studies have shown the AERONET Version 2 Level 2.0 AOD data are impacted by homogeneous optically thin cirrus clouds with a bias up to 0.03 in AOD (DeVore et al., 2009; Chew et al., 2011; Huang et al., 2011). The optically thin cirrus bias can influence radiative forcing calculations and satellite validation when clouds contaminate the measurement (DeVore et al., 2012). In addressing the shortcoming of Smirnov et al. (2000) and manual checks in which the identification of optically thin cirrus clouds give relatively weak signal in the AOD or AE, the authors leveraged high angular resolution radiance measurements routinely performed in the solar aureole region (3.2° – 6.0° scattering angle range). While cirrus detection may be possible with other scattering angle ranges, Cimel Sun photometer radiance measurements do not presently have high enough angular resolution from 6.0° – 35.0° to reliably and consistently detect cirrus induced atmospheric phenomena (e.g.,



solar halos and sun dogs), since these events depend on cirrus crystal shape and orientation and are not always detectable beyond levels of cloud optical depth variability.

559

The use of the solar aureole radiance (L_A ; $\mu\text{W}/\text{cm}^2/\text{sr}/\text{nm}$) with respect to the scattering angle (ϕ ; in radians) has been demonstrated using the Sun and Aureole Measurement (SAM) aureolegraph instrument to indicate the presence of large particles such as cirrus crystals (DeVore et al., 2009, 2012; Haapanala et al., 2017). The effect of the surface reflectance is much less than the radiance of the solar aureole so it is ignored; however, this may become important at very large solar zenith angles and bright surfaces such as snow (Eiden 1968). All Cimel instrument models perform solar aureole measurements at the nominal 1020nm wavelength. The Cimel performs solar triplet measurements directly on the solar disk, while solar aureole radiances are measured mainly during the almucantar, principal plane, and hybrid sky scans. These solar aureole measurements are performed hourly for Models 4 and 5 instruments during sky scan scenarios and for Model T instruments before each solar triplet as well as for the hourly almucantar and hybrid sky scan measurements.

570

The AERONET measurements of the solar aureole directional radiances (L_A) depend on the absolute calibration of the integrating sphere. The integrating spheres at the AERONET calibration centers provide an absolute calibration traceable to a NIST standard lamp hosted at the NASA GSFC calibration facility. The uncertainty in the radiance calibration is typically less than 3% due to systematic degradation in the lamp levels, changes in integrating sphere characteristics, and instrument spectral signal response. The solar aureole radiance magnitudes also depend on the instrument Sun sensitivity gain settings for each wavelength for Cimel Model 4 and 5 instruments, while the Model T instruments use an internal instrument gain switch applying to all wavelengths. The L_A measurements have calibration and temperature correction applied and are measured by all Cimel instruments at the 440nm, 675nm, 870nm, and 1020nm wavelengths. Due to lower AOD in fine mode aerosol loading situations, less Rayleigh scattering, and lower calibration uncertainty, the L_A measurements at 1020nm have less noise for evaluating cirrus cloud presence.

582

Given that the L_A measurements are performed at discrete ϕ , we calculate the ordinary least squares linear regression fit on logarithmic scale when more than three scattering angles are available to determine the intercept (a), slope (b), and the correlation coefficient (R). If R is less than or equal to 0.99, then we do not proceed to check for cirrus contamination. When R is greater than 0.99, the curvature (k_o) for the first available scattering angle (ϕ_o) in the 3.2° – 6.0° scattering angle range is calculated using the equation of curvature of the signed planar curve, which gives the rate of turning of the tangent vector in Eq. (10) (Kline 1998):

589

$$k = \frac{y''}{(1 + y'^2)^{\frac{3}{2}}} \quad (10)a$$

590



591 The curvature (k) can be formulated by assuming the Power Law function and its derivatives, and, in our
592 application, using the first scattering angle (φ_0) in radians for φ below:

593

$$y = a * \varphi^b \quad (10)b$$

$$y' = a * b * \varphi^{b-1} \quad (10)c$$

$$y'' = a * b * (b - 1) * \varphi^{b-2} \quad (10)d$$

594

595 According to the k formulation, the stronger the forward scattering peak, then the smaller the value of curvature
596 since the second derivative is small and the first derivative is large due to the steepness of the solar aureole
597 radiances. Further, the overall slope of curvature for all of the scattering angles (3.2° – 6.0°) can be calculated using
598 the assumption that $y'^2 \gg 1$ rendering the addition of 1 in the denominator of Eq. (10)a insignificant. The slope of
599 the logarithm of curvature versus logarithm of scattering angle is desired and this slope can be calculated using a
600 and b from the linear regression above by converting from logarithmic coordinates. Therefore, we derive the Eq.
601 (11 to determine the slope of curvature dependent only on the slope of the linear regression fit of L_A and φ on
602 logarithmic scale as follows:

603

$$\ln k = a + (1 - 2b) * \ln \varphi \quad (11)$$

604

605 Here, the slope of curvature (M) is defined as $(1-2b)$. The value of M will typically be positive since b will tend to
606 be negative due to the dimming of the solar aureole with increasing scattering angle. Alternatively, M can be
607 calculated numerically for each k and φ to obtain similar results. A small value of curvature (k_0) at the smallest
608 scattering angle available represents the possible existence of large particles producing a forward scattering peak.
609 The slope of curvature (M) represents the average characterization of the solar aureole shape across the scattering
610 angle 3.2° – 6.0° range where a large magnitude signifies the potential presence of large particles as curvature
611 increases with increasing scattering angle across the forward scattering peak.

612

613 The Micropulse LIDAR Network (MPLNET) is a global network of LIDARs monitoring the vertical distribution of
614 aerosols and clouds (Welton et al., 2000, 2002; Campbell et al., 2002). To determine the thresholds for these Sun
615 photometer solar aureole curvature parameters for different surface types and aerosol environments, the MPLNET
616 LIDAR cloud identification database was used at eight collocated AERONET sites as shown in Table 3. Multi-year
617 MPLNET LIDAR deployment data were analyzed and matched with AERONET observations when the solar zenith
618 angle was less than 30° to minimize the spatio-temporal differences of the zenith pointing LIDAR versus the
619 slantwise pointing of the Sun photometer in which sky condition can be quite different at large solar zenith angles.
620 The MPLNET cloud base height data product was matched with MERRA reanalysis vertical temperature profile
621 corresponding to the geopotential height pressure surface. When a cloud top temperature is less than -37°C , a cloud
622 is designated to be cirrus, while other non-cirrus clouds may contain liquid or mixed phase particles (Sassen and
623 Campbell, 2001; Campbell et al., 2015; Lewis et al., 2016). The partitioning the AERONET data set of solar



aureole radiances in terms cirrus clouds, non-cirrus clouds, all clouds, and clear (no cloud base detected) sky condition categories allowed for the empirical determination of potential thresholds for the curvature parameters. For each site, AERONET curvature parameters (k and M) were computed for almucantar and principal plane solar aureole (L_A) measurements (i.e., left and right scans separately) and further categorized based on the coincident LIDAR detected sky condition. These solar aureole radiances have calibration and temperature characterization applied for the 1020nm channel and these L_A measurements were only quality controlled based on the correlation threshold of 0.99 discussed above.

Figure 4a shows the number distribution of the k at NASA GSFC (38.99° N, 76.84° W) for each of the four LIDAR sky condition categories. The number of the potential clouds is large for magnitudes of k less than $2.0\text{E}-5$. Similarly, Fig. 4b and Fig. 4c show the number distributions of the M at NASA GSFC for each LIDAR sky condition category. In Fig. 4b, the number of potential clouds generally dominates when the M is greater than 4.3 with generally clear or possibly cloudy conditions when M is less than or equal to 4.3. Some overlapping of the categories for M may be related to the differences in the viewing geometry of the sky between the Sun photometer and the LIDAR or inhomogeneous cloud conditions.

Algorithmically combining the two thresholds of k and M produces a defined distribution of clear versus cloudy sky condition categories. When the threshold of $k < 2.0\text{E}-5$ is applied first, then the distribution of mainly cloudy conditions becomes more distinct as shown for NASA GSFC in Fig. 4c. The maximum in the number distribution for cirrus is near $M=4.6$ and the maximum in the number distribution of clear sky condition is at $M=4.3$ (Fig. 4c). At Singapore (1.29° N, 103.78° E), Fig. 5c suggests that the distinction of small aerosol particles and larger cirrus cloud ice crystals allows for adequate separation to identify an observation as cloud contaminated using a threshold of M greater than 4.3. Figure 6a shows the number distribution of the curvature at the first scattering angle for coincident AERONET and MPLNET observations at the SEDE BOKER (30.85° N, 34.78° E). Figure 6c shows the distinction is similarly distributed as GSFC and Singapore to potentially identified cirrus contaminated observations. For Fig. 6a, the clear sky condition category is much higher in number than other sky condition categories; however, the k values less than the first scattering angle threshold of $2\text{E}-5$ (shown by the orange vertical line) indicates a significant presence of dust particles rather than cirrus clouds due to forward scattering of dust. Note that as for Fig. 4 and Fig. 5, the x-axis of Fig. 6a is truncated to $1\text{E}-4$ but the number distribution continues at values near zero for larger first point curvatures. SEDE BOKER data in Fig. 6c exhibits a significant contribution of clear conditions are preserved indicating that this method does not appear to misidentify dust as cirrus at this mixed dust and urban pollution site.

When evaluating all of the collocated AERONET/MPLNET sites in Table 3 (Fig. 7), the maximum in the number distribution for cirrus is at $M=4.3$ after the $k < 2.0\text{E}-5$ threshold is applied with a relative minimum for the clear conditions for $M > 4.3$. Given this information, an empirical threshold of $M > 4.3$ can be established for maximizing the removal of cirrus clouds and minimizing removal of potentially clear data points. As mentioned previously, the



almucantar and principal plane sky scans are performed on an hourly basis. If cirrus clouds are homogeneously distributed in the sky, then this assumption allows for the application of the temporal screening of triplet measurements within 30 minutes of the solar aureole measurement time. As a result, a significant number of cirrus contaminated measurements for $M \leq 4.3$ are likely removed with this procedure given the normally distributed number distribution of cirrus identified solar aureole measurements around $M=4.3$. For the Cimel Model T instruments, sky scan aureole measurements are superseded by a special solar aureole scan (CCS) performed from 3.0° to 7.5° scattering angle range at 0.3° increments (left and right) after each triplet solar measurement; therefore, temporal screening for these triplet measurements is applied within two minutes of the CCS scan. Overall, the aureole curvature cirrus cloud screening quality control decreases the probability of a cirrus bias in the AOD data set globally by using this standard procedure. However, the Version 3 Level 1.5 AOD data set may still be influenced by optically thin or sub-visible cirrus clouds with ice crystals similar in diameter to coarse mode aerosols such as those found at polar latitudes or when solar aureole measurements are not available due to instrument malfunction or incomplete data transfer.

Figure 8 shows solar aureole radiances have significant nonlinearity with scattering angle when impacted by cirrus clouds while measurements without cirrus are more linear. The SEDE BOKER site is influenced by desert dust. Dust particles can affect the calculation of the k parameter to be close to the threshold of $2E-5$ even when cirrus clouds are not present (SEDE BOKER case 1); however, the overall slope is more linear for the non-cirrus case compared to the cirrus case (SEDE BOKER case 2). As a result, the M parameter is much lower and the algorithm action would be to preserve the SEDE BOKER Case 1 data and remove data for SEDE BOKER case 2. Note that the k parameter is quite low for SEDE BOKER Case 1 and in general dusty sites may frequently have k less than $2E-5$; therefore, the M curvature parameter is needed to prevent inadvertent removal of aerosol data. For fine mode at GSFC case 1 and Singapore, small values of k and large values of M result in removal of the cirrus-contaminated data. For comparison, the GSFC case 2 shows significant linearity when cirrus clouds are not present. The GSFC case 3 and Trinidad Head case show the variation in these curvature parameters at low optical depths in which only one of the curvature parameters indicates the possibility of cirrus clouds. While these two curvature parameters may be used independently in certain conditions, the current algorithm must employ both curvature parameter thresholds to avoid inadvertently identifying aerosols as clouds in dust and low aerosol loading conditions.

3.3 Level 1.5 Quality Controls to Screen Instrument Anomalies

While cloud-screening quality controls remove a significant portion of data impacted by cloud contamination and some instrument anomalies, a portion of the remaining AOD data set can be impacted by internal or external instrument anomalies. Most instrument anomalies can be removed utilizing the prescreening steps outlined in the Sect. 3.1, but a number of issues still exist which are more evident after the cloud screening quality controls have been applied to the data set. A data set with some clouds can mask or offset patterns in the AOD spectra that can clearly identify data anomalies dependent on optical air mass. For AERONET instruments, data anomalies either dependent on the optical air mass, the sensor head temperature, or leakage, degradation, or looseness of the optical



interference filter. Section 3.1 addresses the quality control procedure with respect to the instrument temperature dependence. Some instrument anomalies dependent on the optical air mass include deviations of the measurement time to the true time (i.e., time shift) and obstruction of light into the silicon or InGaAs detector (e.g., dust, moisture, spider webs). Measurements performed at high latitudes have a slowly varying optical air mass and thus optical air mass pattern recognition is more difficult. The AOD spectra may have optical air mass dependence for out of band leakage or degradation of transmittance due to irregularities in the optical filter composition or the AOD may have significant variability due to a loose filter inside the sensor head.

The retained spectral AOD measurements passing the quality controls from Sect. 3.1 and Sect. 3.2 are evaluated as input for the quality controls in the present section. The removal of nearly all of the clouds and most instrument anomalies from the previous steps allow for more defined pattern recognition. This section will discuss the pattern recognition techniques utilized for the time shift and AOD diurnal dependence, provide a description of the detector consistency, and AOD spectral dependence quality controls. Further, the AOD diurnal dependence algorithm can be used jointly with the detector consistency and AOD spectral dependence quality controls to remove anomalous data with more certainty. These quality controls can be applied for multiple days to remove data impacted by anomalies for more than one day even when clouds interrupt the day-to-day AOD pattern. The final data set is evaluated for the remaining number of observations in a day and deployment period.

3.3.1 Time Shift Screening

AERONET data are transferred by satellite Data Collection Platform (DCP), PC, or SIM card data transfer. The older Vitel satellite transmitters provided a handshake between the instrument and transmitter allowing for time adjustment and newer Sutron Satlink transmitters provide a GPS time stamp to each message. While time shift is not an issue for satellite transmissions, the time shift can become more significant for PC data transfer and even some instruments using SIM card data transfer. AERONET has developed a program called `cimel_https_connect` that can update the processing unit clock of Cimel Model 5 instruments. Older instruments (Model 4) and old non-AERONET data transfer software (e.g., Cimel ASTPwin) do not have the capability to synchronize the Cimel control box with the time-synced AERONET server. Most non-AERONET software requires the PC time to be updated from a timeserver or GPS system to provide accurate clock synchronization. Even some newer Model T instruments transferring data by PC or SIM can have faulty GPS modules in which the clock deviated significantly. Cimel Model T instruments may allow for the PC software (e.g., `cimelTS_https_connect`) updating the time and overriding the GPS module.

A Cimel clock that deviates from true time can result in an optical air mass calculation not appropriate for the actual time especially when the optical air mass varies relatively rapidly diurnally. This instrument anomaly can result in significant changes in the AOD, which affects all wavelengths but most greatly shorter wavelengths (e.g., 340nm, 380nm, and 440nm) at large optical air mass when it changes rapidly. In general, longer wavelength AODs (675nm, 870nm, and 1020nm) have less impact from erroneous optical air mass calculations due to less influence of



molecular (Rayleigh) scattering. As a result, AODs from the longer wavelengths tend to be more stable and AODs from the shorter wavelengths will tend to crossover the longer wavelengths only at one end of the day (near sunrise or near sunset). The timing of the wavelength crossover depends on whether the Cimel clock is too fast or too slow with respect to the actual time. For example, if the time is slow (fast) relative to the actual time, the temporally deviated optical air mass magnitude will be larger (smaller) than the actual optical air mass and thus the short wavelength AODs will be lower (higher) and possibly cross the longer wavelength AODs (significantly increase spectral dependence). In general, Cimel clock temporal deviations in AOD data can be identified using the following:

1. When the shortest available wavelength AOD crosses neighboring UV, visible, and NIR channel AODs near sunset and the short wavelength AOD is decreasing significantly relative a longer stable wavelength (e.g., 870nm) AOD, this condition indicates the Cimel clock is too fast (Fig. 9a).
2. When the shortest available wavelength AOD crosses neighboring UV, visible and NIR channel AODs near sunrise and the short wavelength AOD is increasing significantly relative to a longer stable wavelength (e.g., 870nm) AOD, this condition indicates the Cimel clock is too slow (Fig. 9b).

The AOD differences and trends are used for a specific optical air mass interval (2.5–7.0), where the temporal clock deviation amplifies the error in optical air mass calculations. Individual day screening is limited to mainly cloud free periods with low AOD in areas with significant variation in optical air mass from ~1.0–7.0.

The time shift algorithm is applied over a multi-day period. The algorithm scans the current day plus 19 days in the past (~3 week period) to determine if three or more days indicate the occurrence of a time shift. If the multi-day time shift criteria of three or more days are met, then data between the current day and the last occurrence of the time shift are removed from the field deployment. Although the Cimel clock could possibly be adjusted periodically, most time shift issues tend to occur at remote sites and this approach will maximize the removal of data over the multi-day period to minimize the negative impact on the data from the clock-shifted anomalies. Moderate to high aerosol loading can partly mask the temporal AOD time shift pattern and these data periods may not be removed completely unless they occur between periods of lower aerosol loading when the clock shift spectral AOD pattern is more defined.

3.3.2 Detector Consistency Quality Control

The instrument external collimator on the sensor head avoids stray light and reduces front lens contamination, while the internal sensor head defines the field of view of the instrument (nominally 1.2°) by the achromatic front lens, filter, and field stop before each detector. The external collimator is composed of two tubes and the aperture design varies slightly by instrument type. The Cimel Model 4 instrument type has two Silicon photodiode detectors in the sensor head to measure the Sun and sky while newer model instruments have one Silicon photodiode and one InGaAs photodiode detector to measure the Sun and sky on both detectors. One of the detectors could be impacted



by an obstruction such as a spider web, insect debris, or moisture. For Cimel Model 4 and some Model 5 instruments, the sky scan scenario performs two measurements at the 6° azimuth angle for the almucantar and 6° scattering angle for the principal plane at each wavelength over both detectors. For these older instruments, the solar aureole gain is used for the solar Silicon diode detector and the sky gain is used for the sky Silicon diode detector. These redundant measurements can allow for detection of the change in the relative signal but this method is currently more appropriate to use for quality controlling the inversion products due to uncertainty in sky calibration. Newer Model 5 and Model T instruments (with the solar and sky measurements performed on both detectors) do not have the redundant sky measurement; instead, these instruments have a redundant solar measurement at 1020nm in both collimator tubes, where each solar measurement of the triplet is performed within eight seconds of each other. The AOD 1020nm measurements on Silicon and InGaAs detectors can be compared directly to determine if an obstruction exists in front of either of the detectors. Applying a similar approach to Giles et al. (2012), the difference limit ($\Delta\tau_{Limit}$) can be computed using the optical air mass and AOD magnitude dependent formulation (Eq. (12)):

$$\Delta\tau_{Limit} = \frac{(0.04 + (0.02 * MIN[\tau_{1020nm}]))}{m} \quad (12)$$

where $MIN[\tau_{1020nm}]$ is the minimum of the AOD at 1020nm obtained from the redundant AOD 1020nm measurements on Silicon and InGaAs detectors and m is the optical air mass. The difference limit for an AOD 1020nm minimum of 1.0 will result in the 0.06/m 1020nm difference limit described in Giles et al. (2012). A more lenient approach is used here based on the AOD magnitude to prevent removal of data for low AOD at 1020nm. At low AOD, the average field instrument uncertainty (up to 0.01) becomes more significant while the maximum AOD error occurs at midday and differences due to their temperature dependency can contribute up to 0.02 AOD bias. Given the relative difference in the AOD 1020nm measurements, the maximum uncertainties in both 1020nm measurements must be considered. Therefore, the 0.02 threshold is derived from the average uncertainty (up to 0.01) and the 0.04 limit is derived from the maximum midday error in AOD and temperature dependency (up to 0.02). When more than 10% of the total measurements for the day exceed the $\Delta\tau_{Limit}$, data are removed in the following manner:

1. If the AOD 1020nm Silicon subtracted by the AOD 1020nm InGaAs detector is greater than $\Delta\tau_{Limit}$, then the Silicon side has an obstruction and the entire measurement is removed for both Silicon and InGaAs AOD data.
2. If AOD 1020nm Silicon subtracted by the AOD 1020nm InGaAs is less than $-\Delta\tau_{Limit}$, then the InGaAs detector has an obstruction and only the InGaAs AOD for 1020nm and 1640nm measurements are removed.
3. If the redundant AOD 1020nm values are nearly the same ($-\Delta\tau_{Limit} \geq \Delta\tau \geq \Delta\tau_{Limit}$), then an obstruction could possibly exist in the event that a substance (e.g., spider webs, dust, moisture) similarly obstruct both detectors.

For condition (3), this case is further evaluated by the AOD diurnal dependence quality control in the next section.



805 3.3.3 Aerosol Optical Depth Diurnal Dependence

806 The AERONET instrument has spectral calibrations made and typically applied both before and after field
807 deployment. When the instrument operates in the field, the pre-field spectral calibration applied to the near real-time
808 data is constant. If the calibration changes significantly during the instrument deployment, the error in the
809 computation of the AOD increases with decreasing optical air mass where the maximum error occurs when optical
810 air mass approaches one ($\delta\tau^*m$; Hamonou et al., 1999). As a result, an apparent diurnal dependence in the AOD can
811 occur depending on the magnitude of the deviation from the pre-field calibration. When both the pre-field and post-
812 field calibrations are applied and data still show a diurnal dependence in the AOD, then the deviation in the field
813 measurements is due to a non-linear change in the calibration coefficient since Level 2.0 data utilize a linear
814 interpolation between the pre-field and post-field calibration coefficients.

815

816 Midday maximum (concave pattern) or midday minimum (convex pattern) of AOD diurnal dependence can be
817 observed at any AOD magnitude but are typically more pronounced at lower aerosol loading due to calibration
818 offset (Cachorro et al., 2004) or instrument anomalies. Quality controls developed for the analysis of the AOD
819 diurnal dependence need to consider the impact of clouds and missing data to assess whether to remove these data
820 while minimizing the removal of data exhibiting true diurnal dependence. For example, one cloud-free day may
821 show diurnal dependence, but on another day, the morning or afternoon data may not be available due to missing
822 data during cloudy or rainy periods. The algorithm must have a sufficient number of observations to perform a
823 robust assessment of the AOD diurnal dependence.

824

825 Variation in the number of available measurements in a day due to clouds or instrument issues can limit the
826 application of a single day only approach. As a result, the morning and afternoon periods must have at least five
827 measurements separately and the analysis of the full day must have at least 10 measurements. To analyze the
828 diurnal dependence and reduce the impact of outliers, the GNU Scientific Library robust least squares (RLS) linear
829 regression fit is performed for AOD versus the inverse optical air mass (m^{-1} , where m is approximately the cosine of
830 the solar zenith angle). The slope and correlation coefficient (R) values derived from the linear fit are used as
831 thresholds to determine the magnitude and strength of the diurnal dependence (Table 4).

832

833 The nominal AERONET 440nm, 675nm, 870nm, and 1020nm wavelengths for the Silicon detector and 1640nm for
834 the InGaAs detector are assessed for diurnal dependence and potential removal of all spectral channels. An example
835 of the AOD diurnal dependence of 1020nm wavelength is shown in Fig. 10 at the Rio Branco (9.96° S, 67.87° W)
836 AERONET site where the site manager indicated spider webs were obstructing measurements. If data are removed
837 for the InGaAs detector, then only InGaAs detector data are removed, while removal of the Silicon detector data will
838 remove all data including InGaAs detector data, if any. The AOD diurnal dependence is classified as two
839 categories: independent and dependent. If the algorithm meets the strict thresholds for “independent” diurnal
840 dependence, then all channels exhibiting diurnal dependence can remove data for a day, except the 1020nm channel
841 since some old data with temperature defaults may exhibit false diurnal dependence. Otherwise, all of the above



842 channels are used for the “dependent” diurnal dependence quality control. The dependent diurnal quality control
843 relies on more lenient thresholds for the slope and R ; however, the removal of data generally requires that another
844 quality control flag is set such as the detector consistency quality control (Sect. 3.3.2), where an obstruction was
845 identified in front of one of the detectors or at least one additional qualified wavelength meeting the slope and R
846 thresholds. When a qualified wavelength indicates dependent AOD diurnal dependence for Day or both AM and
847 PM and AM and PM slopes are positive, then the entire day can qualify for independent removal. This methodology
848 allows for a more skilled approach in removing only data affected by instrumental anomalies while minimizing the
849 removal of data coincidentally producing a true diurnal dependence signature.

850

851 The AOD diurnal dependence identification can be complicated by changes in aerosol loading during the day, cloud
852 artifacts, and missing data. A multi-day scan must be performed to maximize the removal of data impacted by
853 instrument anomalies. A multi-day assessment example is provided in Fig. 11 for Rio Branco. Figure 11a shows
854 that the spectral AOD varies significantly diurnally for the period from 26 August to 5 September 2011, especially
855 for the 870nm and 1020nm near infrared wavelengths. Figure 11b shows evaluation of the slope and correlation
856 coefficient (R) for the AOD 1020nm daily variation, which shows 7 of the 10 days exceeding the thresholds (slope $>$
857 0.1 and $R > 0.94$) and wavelengths established in Table 4. For these data to qualify for dependent AOD diurnal
858 dependence removal, additional information is needed such as another qualified wavelength with slope and R
859 exceeding the thresholds. For this case, the AOD 870nm daily slope and correlation parameters (not shown) also
860 exceed the thresholds, which lead to the elimination of these data from Levels 1.5 and 2.0. Similar to the time shift
861 screening in Sect. 3.3.1, the AOD diurnal dependence algorithm scans the last 19 days including the current day to
862 determine the first occurrence and last occurrence of the dependent and independent AOD diurnal dependence.
863 When three or more days are identified, data are removed from the first occurrence to the last occurrence of AOD
864 diurnal dependence during the 20-day period. The multi-day screening allows for the elimination of data affected by
865 an obstruction in the instrument field of view even with moderately high aerosol loading in the NIR wavelengths
866 and when days with incomplete number of measurements from the established protocol due to clouds.

867 3.3.4 Reverse Spectral Dependence

868 While the majority of the cloud screening quality controls remove aerosol measurements contaminated by clouds,
869 some spurious points or slowly varying changes in cloud properties may still affect the data set at this point in the
870 algorithm. A new method (Fig. 12) utilizing the Ångström exponent (AE) is applied to the remaining data set for
871 evaluation of cloud contamination. Ångström exponents derived from anomalous AOD measurements due to
872 instrument artifacts may produce a similar signature. The spectral dependence among the wavelengths is now much
873 improved compared to Version 2 by removing temperature dependencies that influenced the calculation of the AE at
874 low AODs reducing the effect of improper spectral dependence due to temperature anomalies.

875

876 The AE is computed utilizing the ordinary least squares fit of the logarithms of AOD and wavelength for the ranges
877 of 440–870nm, 870–1640nm (if 1640nm is available), and the 870–1020nm (for Silicon detectors only) range (Eck



et al., 1999). The reverse spectral dependence algorithm in Fig. 12 removes cloud contaminated points utilizing these AE ranges depending on the instrument model. Figure 13 shows the removal of the anomalously high AOD at the Bratts Lake (50.20° N, 104.71° W) AERONET site in southwest Canada. In Fig. 13b, all negative and a few positive AE values are identified and the algorithm removes nearly all of the residual cloud contamination in this case. However, the penultimate and final measurements in Fig. 13c have slightly higher AOD than the previous hour of data, which may be due to marginal contamination by optically thin cirrus clouds. Additional algorithm development is still needed to further enhance the removal cloud contaminated data with small ice crystals while not removing dust aerosols.

3.3.5 Aerosol Optical Depth Spectral Dependence

The wavelength dependence of AOD typically is strong for fine mode aerosols (e.g., pollution or smoke) and weak for coarse mode aerosols (e.g., dust or sea salt). The AE provides an index of the strength of the spectral dependence related to the estimation of the possible aerosol size (Eck et al., 1999). In general, the $AE_{440-870nm}$ will typically provide values between approximately 0.0 and 3.0. These prospective values indicate no spectral dependence at $AE_{440-870nm}$ of 0.0 and very strong spectral dependence with an $AE_{440-870nm}$ near 3.0 (AE values of 3.0 have not been observed in good quality data with sufficiently high AOD). The spectral dependence can be used to evaluate the quality of each channel given that most channels in the measurement suite adhere to the stated AOD uncertainty of 0.01 for wavelengths $\geq 400nm$ and 0.02 for wavelengths $< 400nm$ (Eck et al., 1999). The fit of the AOD with wavelength on logarithmic scale should generally be linear for coarse mode dominated or fine/coarse mode particle mixtures. However, in moderate to high aerosol loading cases (especially when fine mode dominated), a quadratic or cubic assumption is needed to fit the data depending on the wavelength range under evaluation (Eck et al., 1999; O'Neill et al., 2008). The ordinary least squares (OLS) methodology is perturbed by the presence of outliers and therefore skews the fit towards outliers. If the boundary wavelengths are impacted by anomalies, the ordinary least squares can poorly fit other intermediate wavelengths.

In an effort to reduce the influence of outliers, the GNU Scientific Library (GSL Version 2.2.1 C compilation) robust least squares (RLS) technique is utilized to improve the removal of spectral AOD outliers. In general, the OLS technique is sensitive to the endpoints and to the number of points used in the regression. For example, the outlier detection will have less skill with a few points or anomalous endpoints. The RLS scheme uses an iterative approach with up to 100 passes using the Tukey biweight function and assigning the outliers a lower weight with each pass. The RLS approach allows for the more meticulous removal of wavelengths out of spectral dependence and more importantly preserves mid-visible wavelengths that could be removed incorrectly when utilizing the ordinary least squares method.

Outlier detection is performed utilizing the uncertainty of the AOD measurement and providing an allowable tolerance in the fit given potential irregular nature of the uncertainty (0.01 to 0.02). For wavelengths $\geq 400nm$ and $< 1600nm$, the allowable AOD difference between the measurements and fit for a candidate wavelength is



($0.02 \cdot \text{AOD}$)+0.02, based on the stated AOD uncertainty for these wavelengths (Holben et al., 1998; Eck et al., 1999). For wavelengths <400nm and 1640nm, the allowable AOD difference between the measurements and fit for a candidate wavelength is ($0.02 \cdot \text{AOD}$)+0.04, which is adjusted for greater uncertainty at the UV wavelengths and greater uncertainty in the larger spectral range to fit the 1640nm wavelength.

The spectral outlier procedure begins by identifying and removing any negative AOD values that are not within the allowable AOD difference from the RLS linear fit. Negative AOD due to slight calibration drift can be observed at very clean locations; otherwise, these negative values may be anomalous. The algorithm will evaluate each wavelength separately and compute the RLS linear fit based on the remaining wavelengths producing the slope, intercept, and R^2 values, where the slope and intercept are used to compute the AOD fit at the wavelength under evaluation. If the algorithm does not identify any wavelengths for removal, then the procedure is complete. If AOD is low ($\text{AOD}_{440\text{nm}} < 0.1$) and one wavelength AOD exceeds the maximum allowable difference, then the wavelength will be removed due to the linear fit deviation. However, if more than one wavelength has AOD marked for removal for the low AOD condition, then the wavelength with the largest departure from the linear fit to the measurement and largest R^2 will qualify for removal.

In the case of higher AOD ($\text{AOD}_{440\text{nm}} \geq 0.1$), the algorithm stores the information from the RLS linear fit and continues to perform a RLS quadratic fit ($400\text{nm} \leq \lambda \leq 1020\text{nm}$) or a RLS cubic fit ($\lambda = 1640\text{nm}$). If the candidate wavelength deviates from the allowable difference in fit to the measurements for the higher order fits, then the wavelength will be removed if it is identified as a wavelength that corresponds to the maximum deviation for the RLS linear fit. Figure 14 provides an example of this condition at the Osaka (34.65° N , 135.59° E) AERONET site. After each wavelength removal regardless of order of the fit, the algorithm repeats until no wavelength removals occur or when less than three wavelengths remain.

3.3.6 Large Aerosol Optical Depth Triplet Variability

In addition to growth of hygroscopic aerosols near cumulus cloud boundaries and large triplet variability at short wavelengths in highly variable fine mode plumes, a misaligned filter due to improper filter wheel movement or dust on the filter may produce large AOD triplet variability ($\text{AOD Max} - \text{AOD Min}$). The cloud screening triplet variability quality control removes the entire measurement when 675nm, 870nm, and 1020nm AOD triplets have large triplet variability exceeding the threshold (0.01 or $0.015 \cdot \text{AOD}$, whichever is greater). A situation may exist where one of those wavelengths or shorter wavelengths are impacted by a filter anomaly making it necessary to assess the large AOD triplet variability. If the triplet measurement is identified for high AOD retention (Sect. 3.1.6), then the following large adjacent triplet quality control is not performed because very high aerosol loading in fine mode events can lead to large triplet variability naturally. Occasionally, if the triplet is very large and exceeds the limit of $0.03 + 0.2 \cdot \text{AOD}$, then the wavelength is removed independently of the next longer wavelength.



To further screen anomalous triplets individually or the entire day, each triplet and wavelength is evaluated using the triplet variability from the shortest wavelength (e.g., 340nm) and the next longer wavelength (e.g., 380nm). The allowable triplet variability limit is computed based on the aerosol loading and the AOD triplet variability of the next longer wavelength: $0.03+0.02 \cdot \text{AOD} + \text{triplet_variability_of_next_longer_wave}$. If the total number of triplets for a wavelength exceeding the large triplet variability threshold is more than 25%, then the AOD measurements for the wavelength are removed completely for the entire day. Figure 15 shows the large triplet variability removal at the PEARL (80.05° N, 86.42° W) AERONET site in northern Canada. The triplets at shorter wavelengths may naturally exhibit relatively large triplet variability hence it is necessary to check the shorter wavelength in comparison to the next longer wavelength which typically will be more stable if clouds do not impact the measurements.

3.3.7 Remaining Measurements Evaluation

After the previous quality control algorithms have been applied, extraneous data points may remain and are identified for possible removal. A number of conditions have been implemented based on the total data removed for the day, number of wavelengths remaining for the day, and number of measurements for a wavelength for a deployment. These “cleanup” conditions below will remove all wavelengths in a day for any of the following conditions dependent on the “retain high AOD” from Sect. 3.1.6 and the number of wavelengths in a day:

1. If retain high AOD and less than two wavelengths remain in a day
2. If retain high AOD and two wavelengths but are not 870nm and 1020nm in a day
3. If not retain high AOD and less than three wavelengths remain in a day
4. If not retain high AOD and less than half of the wavelengths remain in a day

Each wavelength must be evaluated for remnant data artifacts. If greater than 50% of the total cloud screened AOD data for a wavelength in a day are removed, then AOD measurements for the candidate wavelength will be removed for the day. Further, a condition is implemented to remove specific wavelengths for an entire deployment. For example, if the number of measurements for a wavelength is less than 20% of the total cloud screened data set for a deployment, then all of the measurements for the specified wavelength will be removed for the deployment. These removal conditions are necessary to fully quality control the spectral AOD data set and avoid unphysically irregular and fragmented data sets.

3.4 Algorithm Performance Assessment

Data quality controls applied to the quality controlled Level 1.0 data set are evaluated for removal performance for each part of the Level 1.0 prescreening and Level 1.5 algorithm. The Level 1.0 prescreening is applied to about 84 million solar triplet measurements from 1993–2018. The radiometric sensitivity screening (see Sect. 3.1.2) for the DN of 1020nm removes about 36% and the digital voltage triplet variance greater than 0.16 (see Sect. 3.1.3) removes nearly 11% of the Level 1.0 data. The remaining Level 1.0 prescreening that check for radiometric sensitivity screening for DN of 870nm, extreme temperatures ($T_s \leq -40^\circ\text{C}$ or $T_s > 100^\circ\text{C}$), and bad measurement



984 configuration conditions remove approximately 0.5% of the Level 1.0 data. Therefore, nearly half (48%) of the
985 initial 84 million solar triplet measurements are removed by the Level 1.0 prescreening steps due to the presence of
986 clouds in the solar measurements that greatly reduce the signal (e.g., stratus clouds) or exhibit significant temporal
987 variability within the one minute triplet measurement sequence (e.g., cumulus clouds).

988

989 The Level 1.5 quality control algorithm is divided into the two main steps for cloud screening and instrument data
990 anomaly removal.

991 Figure 16 shows the percentage of the Level 1.0 data removed by the Level 1.5 cloud screening quality control.
992 Over 23% of the removal in the cloud screening algorithm was due to the large triplets at the long wavelengths
993 (675nm, 870nm and 1020nm). Nearly 5% of the removal of the Level 1.0 data was due to the presence of cirrus
994 clouds as detected by the solar aureole curvature algorithm and is significant since a cirrus contamination bias is
995 evident in the AOD in Version 2 Level 2.0 data set. The “Unqualified” category indicates data that are negative
996 AOD or lack the sufficient channels to participate in the cloud screening part of the algorithm and these
997 measurements are rejected from Level 1.5. After all of the data are cloud screened, about 66% of the Level 1.0 data
998 are passed to the second part of the Level 1.5 instrument quality control algorithm for examination of the instrument
999 anomalies and other spurious clouds and artifacts.

1000

1001 The second stage of the Level 1.5 quality control algorithm utilizes measurements passed from the cloud screening
1002 algorithm. While the cloud screening algorithm rejects the entire measurement in the presence of clouds, the
1003 instrument quality controls can also reject the entire measurement or remove data by wavelength depending on the
1004 anomalous condition.

1005 Figure 17 shows the removal of Level 1.5 cloud screened data due to mainly instrument anomalies for each
1006 wavelength. More than 2.5% of the data are removed due to the AOD diurnal dependence screening, about 2% for
1007 the time shift screening, and 1.5% for the AOD 1020nm difference screening. These three instrument quality
1008 control algorithms remove in general the most across all wavelengths. Some removal occurs significantly spectrally
1009 for the InGaAs channel (1640nm). The InGaAs channels can be affected in some instruments more significantly by
1010 water contamination as the InGaAs side of the collimator is facing away from the Sun when in the parked or resting
1011 position. Further, when the algorithm removes all of the Silicon channels, the remaining InGaAs channels are also
1012 removed since no other independent method exists to check the InGaAs channel data quality. The “Remaining”
1013 measurements removal shows that nearly 4% of the cloud screened data are removed from the InGaAs data set. The
1014 AOD spectral dependence removes more than 2% of the 340nm wavelength data, which tends to be the most
1015 unstable wavelength (due to filter degradation), and about 0.5% for all other wavelengths. The temperature
1016 screening removal of missing or anomalous temperatures mostly affects the Silicon 1020nm wavelength with nearly
1017 1% of the cloud-screened data removed due to its large temperature dependence compared to the other wavelengths.



1018 4 Assessment of the Quality Assurance Data Set

1019 The aerosol optical depth (AOD) data will be qualified for consideration of Level 2.0 once it passes the Level 1.5
1020 checks. To reach Level 2.0, these data must meet the following conditions:

- 1021 1. Data must have pre-field and post-field calibration applied; or in some cases, the pre-field deployment or
1022 post-field deployment calibration may be made constant for the deployment after evaluation of the best
1023 calibration values.
- 1024 2. Temperature characterization must be applied utilizing the temperature correction for the instrument or
1025 default values for each wavelength.
- 1026 3. Instrument must be designated as the primary instrument for the site.

1027
1028 Once the above conditions are met, these data are considered to reach Level 2.0. These Level 2.0 data are
1029 recommended for publication and use in various atmospheric applications. The automated algorithm attempts to
1030 preserve aerosol data while removing data artifacts. Some unusual atmospheric conditions (e.g., small cirrus
1031 particles $r < 5\mu\text{m}$) or rare instrument anomalies (e.g., loose filters or partially removed multi-da AOD diurnal
1032 dependence) affecting the AOD may rarely pass through the algorithm and users are advised to consider inspecting
1033 these data carefully when using them for detailed studies. Further, optical air mass dependent anomalies such as the
1034 time shift and AOD diurnal dependence quality controls may allow data to pass when aerosol loading is high or too
1035 few data exist to make an assessment. These quality controls can determine patterns more skillfully at lower aerosol
1036 loading which could result in retaining potentially contaminated high aerosol loading periods when the pattern may
1037 be less defined and does not meet the quality control thresholds.

1038
1039 The subsequent sections discuss the impact of the temperature characterization on the Version 3 Level 2.0 AOD data
1040 to quantify the change in regards to the Version 2 Level 2.0 data set. Further, the assessment of the Version 3 near
1041 real-time product is made to determine the average bias of the AOD based on the applied calibration. Finally, an
1042 analysis is made of the Version 3 Level 2.0 AOD long-term averages for select AERONET sites and these are
1043 compared to the Version 2 Level 2.0 AOD long-term averages.

1044

1045 4.1 Temperature Characterization Evaluation

1046 The accurate measurement of the spectral direct-beam Sun intensity (from which AOD is computed) depends on the
1047 sensor head temperature of the instrument as discussed in Sect. 2. The sensor head temperature can vary
1048 significantly since the optical head canister is heated by the Sun and can be much higher ($>10^\circ\text{C}$) than the ambient
1049 temperature especially near solar noon. The temperature sensitivity of the Silicon detector is more significant for
1050 the 1020nm filter due to the proximity to the edge of the spectral range of the detector in which temperature
1051 dependence becomes more significant. The temperature dependence for all wavelengths may vary due to the
1052 composition and/or manufacturing quality of the filters and/or detectors. Due to technical difficulty, the ultraviolet
1053 wavelength ($\lambda < 400\text{nm}$) filters have not been temperature characterized in Version 3; however, UV filters may have



a temperature dependence. Figure 18 shows the difference in the AOD temperature coefficients for Version 3 temperature correction applied to Version 3 data and Version 2 temperature correction applied to Version 3 AOD data from 1993–2018. The AOD varies most significantly for the Silicon 1020nm channel with a full range of ~ 0.02 for sensor head temperatures between -25°C and $+55^{\circ}\text{C}$. Notably, the shorter wavelength channels and the InGaAs wavelengths (i.e., 1020nm and 1640nm) do not show significant change in AOD less than 40°C . All of the wavelengths, except the Silicon 1020nm, show an AOD difference decrease from -0.005 to -0.010 for temperatures greater than 40°C , which may be due to changes in instrument characteristics (e.g., electronic instability in the instrument) at high temperatures. The decreasing AOD difference with increasing temperature may be related to the smaller number of observations at high temperatures and contribution by instruments with temperature characterization measurements that did not reach temperatures greater than 40°C . Temperature characterization has proven to be small yet necessary adjustment to the AOD computation and this improvement is especially exhibited in arctic regions or sites with very low aerosol loading in which the Version 3 AOD spectra have much less crossover allowing for the computation of more accurate Ångström exponents than in the Version 2 data set.

4.2 Level 1.5 Near Real-time Aerosol Optical Depth Bias and Uncertainty

The Version 3 near real-time data set provides improved data quality compared to Version 2 since the algorithm has improved cloud screening and instrument quality controls applied to the data. The data set can vary in the near real-time interval from current day up to one month as ancillary data sets are received and processed, hence, these database changes invoke reprocessing of the AOD throughout the near real-time phase. Once AOD data have been pre-field and post-field calibrated, then these data may be raised to Level 2.0 as described in Sect. 4. The near real-time data using only constant pre-field calibration is compared to the quality assured data set that uses both the pre-field and post-field calibrations applied to the data with the assumption of linear interpolation. Figure 19 shows the distribution by wavelength for this comparison of the near real-time and quality assured data set for the entire database of Level 2.0 qualified data excluding calibration site data and deployments using a copied pre-field or post-field calibration. These results are based on the Version 3 Level 2.0 data set in which the Level 1.5 algorithm scans the entire deployment. The AOD difference histograms were computed for optical air mass ranges ($1.0 \leq m < 7.0$ and $1.0 \leq m < 1.5$). The optical air mass $1.0 \leq m < 7.0$ range includes all of the data; however, these AOD difference magnitudes will be constrained by the improved AOD measurements at large optical air mass and influenced toward Northern hemisphere winter mid-latitude sites when AOD tends to be low. The optical air mass $1.0 \leq m < 1.5$ range includes data will provide AOD measurements near solar noon and these measurements are generally less accurate ($\delta\tau \cdot m$) than at larger optical air mass. In addition, optical air mass $1.0 \leq m < 1.5$ range data include a greater influence of tropical locations and data from the mid-latitude summer when AOD tends to be moderate to high.

Figure 19 shows the AOD average differences for the $1.0 \leq m < 7.0$ range indicate a positive bias in which the AOD for the pre-field only calibration tends to be on average $+0.003$ to $+0.009$ higher than the AOD using the interpolated calibration. Similarly, AOD average differences for the $1.0 \leq m < 1.5$ range show a positive bias and similar wavelength variations but up to two times larger differences than for the $1.0 \leq m < 7.0$ range. The largest



average differences and standard deviations are for the UV wavelengths, which have greater uncertainty as discussed in Sect. 2. The AOD differences for the wavelengths longer than 500nm have about less than half the bias of the UV wavelengths. The Level 1.5 algorithm performance improves with increased data availability such as a greater number of wavelength or number of days. When an instrument deployment begins, some of the Level 1.5 algorithm steps such as multi-day removal schemes are not available until several days into the deployment producing larger differences in the near real-time AOD with respect to the final product. While wavelength dependent biases of +0.003 to +0.009 for the $1.0 \leq m < 7.0$ range and +0.006 to +0.015 for the $1.0 \leq m < 1.5$ range exist when only the pre-field calibration is applied, the difference can vary significantly depending on each instrument deployment necessitating continued post-field calibration and maintenance effort.

When an instrument is deployed in the field, the pre-field calibration is used constantly until the post-field calibration is assessed and applied to the data using linear interpolation. The difference of pre-field calibration AOD minus the post-field calibration AOD average difference and standard deviation are computed in day bins for the number of days since the pre-field calibration. Figure 20 shows the AOD 500nm average difference for the optical air mass ranges: $1.0 \leq m < 7.0$ and $1.0 \leq m < 1.5$. Instruments typically operate in the field between 12 and 18 months from the pre-field calibration date; however, the instrument deployment may be delayed and the instrument may not begin operation for a few months after the pre-field calibration. Thus, the number of AOD measurements in the days since pre-field calibration bins increase to a maximum at about 100 days. Some instruments may operate longer in the field to support field campaigns and other scientific priorities. Figure 20 shows that the AOD average difference and the standard deviation slowly but steadily increase for each optical air mass range. At about 1.5 years after pre-field calibration (~550 days), the AOD average difference is about +0.010 with a standard deviation of 0.015 for optical air mass $1.0 \leq m < 7.0$ range and +0.017 with a standard deviation of 0.021 for $1.0 \leq m < 1.5$. For the UV wavelengths, the average differences and standard deviations tend to increase slightly while the longer visible and near infrared wavelengths tend to decrease slightly. Therefore, the quality of the Level 1.5 near real-time AOD changes with time with high quality data at the start of the deployment but up to a +0.02 bias and 0.02 uncertainty for data collected more than 1.5 years since pre-field calibration.

4.3 Multi-year Monthly Comparisons of Version 3 Level 2.0 to Version 2 Level 2.0 Databases

Long-term average differences between the Version 3 and Version 2 Level 2.0 data sets provide insight into the changes to be expected across most AERONET sites. The analysis of the Version 3 and Version 2 data sets shows mainly the differences in the AOD, $AE_{440-870nm}$, precipitable water (PW) in cm, and the number of days are clustered near zero (Fig. 21). Note that precipitable water data quality depends on the quality of the input wavelengths (675nm and 870nm) and no further quality control is made on the 935nm wavelength. The increases in the Version 3 Level 2.0 multi-year monthly average AOD are often due to the increased presence of fine mode particles from high aerosol loading events as well as aerosols in near cloud environments (Eck et al., 2018). The decrease in the multi-year monthly average AOD is due to the improved removal of clouds in the Version 3 quality control algorithm.



1126 Generally, the results should be very similar between Version 3 and Version 2 in AOD calculation since the
1127 temperature characterizations as well as NO₂ absorption contributions typically have relatively minor contributions.

1128
1129 Other factors affecting the AOD calculation include the adjustment of site coordinates and elevation information for
1130 about 100 AERONET sites utilizing GPS or digital elevation model. A few rare extreme coordinate adjustments of
1131 more than 25 km included Petrolina_SONDA (9.0691° S, 40.3201° W), Ilorin (8.4841° N, 4.6745° E), and
1132 Ouagadougou (12.4241° N, 1.4872° W). A large site coordinate adjustment can complicate satellite matchups for
1133 these few cases but the review of all AERONET sites showed that less than a 5 km distance adjustment and less than
1134 100-meter elevation adjustment was needed for most of these 100 suspected sites.

1135
1136 Figure 22 shows similar plots to Fig. 21 except that the observations used for the multi-year monthly averages in
1137 both data sets the instantaneous observations are time matched, hence, each data set has the same number of
1138 observations and number of days. The time matched long-term average comparison provides insight into the AOD
1139 calculation differences rather than impacts due to cloud screening and instrument quality controls applied in Level
1140 1.5. Table 5 shows the multi-year monthly overall standard deviation and AOD maximum to minimum range is
1141 significantly reduced compared to the data set without time-matched observations. Figure 22a shows a slight
1142 decreasing trend of Version 3 AOD for increasing Version 2 AOD and most of the larger AOD deviations are for
1143 sites in Asia where the impact of the OMI NO₂ corrections may be contributing to the slight shift of up to 0.02 for a
1144 few months and sites.

1145
1146 For unmatched or time matched data sets in Table 5, the precipitable water climatology changed on average
1147 insignificantly. The multi-year monthly overall days difference (Table 5) for the unmatched precipitable water data
1148 set was near zero and the standard deviation was near 25 days while the maximum of +150 and minimum of -130
1149 days indicate significant variability due to the differences in quality controls between the algorithms. Overall, the
1150 changes from Version 2 to Version 3 in precipitable water are generally negligible in terms of the contribution to the
1151 calculation of the AOD.

1152
1153 Overall, the multi-year monthly overall average difference between Version 3 and Version 2 for unmatched data is
1154 +0.002 and time matched data is -0.002 indicating remarkable consistency between the long-term average quality
1155 assured data sets. For example, the NASA GSFC AERONET site multi-year monthly average (Fig. 23) located 20
1156 km north of Washington, D.C., shows minor variations in the AOD and increase in AE due to removal of cirrus
1157 clouds during the winter months and increasing AOD in the summer months due to the greater abundance of cloud
1158 processed or near cloud aerosols (Eck et al., 2014).

1159
1160 Comparison of AE_{440-870nm} in Fig. 21b and Fig. 22b show significantly lower values for Version 3 than Version 2
1161 Level 2.0 at low optical depth. An analysis of long-term average data at Lulin, Taiwan (23.47° N, 120.87° E)
1162 identified significant reduction of Version 3 AE relative to Version 2 AE at very low AOD due to temperature



characterization that resulted in improved AOD spectral dependence (Fig. 24). The Lulin site is a high altitude mountain station located in south central Taiwan, and this site is affected episodically by trans-boundary aerosol plumes from East and Southeast Asia (Lin et al., 2013; Wang et al., 2013). In eastern China, multi-year monthly averages from the XiangHe site (39.75° N, 116.96° E) show a significant Version 3 AOD increase of 0.2, while maintaining nearly the same AE and increasing the number of days up to near 40% for the multi-year monthly average in July and August (Fig. 25). The XiangHe site is located to the east of Beijing and is routinely impacted by urban pollution and episodically by biomass burning and desert dust events (Li et al., 2007). The significant increase in the AOD for XiangHe is likely due to the retention of highly variable fine mode aerosol events particularly at very high AOD, which were removed by the Version 2 cloud screening wavelengths utilizing large triplets less than 675nm (Eck et al., 2018). Additionally, some very high AOD events at XiangHe were previously removed by the Version 2 mid-visible low signal threshold but are now retained in Version 3, but often only for wavelengths longer than 675nm, so the statistics for these days are not accounted for in the 500nm data shown in Fig. 25.

At the Mongu (15.25° S, 23.15° E) site (Fig. 26), the biomass burning smoke typically occurs during the dry season from April through November due to biomass fuel cooking and agricultural burning (Eck et al., 2003). Comparisons of multi-year monthly averages for the Mongu site shows small deviations for AOD up to ± 0.01 with slight increases in Version 3 AE during December through March due to enhanced cirrus cloud removal from the solar aureole check. Notably, the number of days for the Mongu multi-year monthly averages significantly decreased by 10% to 25% in Version 3 due to improved cloud screening and sensor head temperature anomalies affecting instrument performance. In Cinzana, Mali (Fig. 27), the aerosol loading is dominated by background dust aerosol with episodic contributions to the aerosol loading from biomass burning smoke from November to March (Cavalieri et al., 2010). The AERONET IER-Cinzana site (13.28° N, 5.93° W) multi-year monthly averages show generally 0.03 lower AOD for Version 3 than Version 2 and nearly the same AE for both versions. The number of days for each month is 7% to 25% lower in Version 3 when compared to Version 2 mainly due to improved cirrus cloud screening.

5 Summary

The Aerosol Robotic Network (AERONET) has adopted a new automated quality assurance algorithm called Version 3. The significant impacts of the Version 3 algorithm are updated and improved cloud screening and quality control methods, which are powerful tools in quality assuring the Sun photometer AOD data. Comparisons between the quality assured data sets of Version 3 and Version 2 show excellent agreement. Deviations can be explained by known algorithm differences such as changes in the cloud screening triplet variability, cirrus cloud detection and removal, implementation of temperature characterization, updates to NO₂ climatology, modification of site coordinates and elevation, and identification of instrument anomalies such as aerosol optical depth (AOD) diurnal dependence, AOD spectral dependence, and instrument electrical and temperature stability.



1199

1200 Major highlights of this work include (not listed in priority):

- 1201 1. An automatic quality control algorithm significantly reduces the necessity of analysts to inspect millions of
1202 AERONET measurements. The AERONET Version 3 algorithm applied in near real-time provides high
1203 quality AOD for data assimilation applications. The Version 3 Level 2.0 data is provided within 30 days of
1204 the post-field calibration evaluation after the instrument deployment, improving the timeliness of quality
1205 assured data.
- 1206 2. Improvements to the total AERONET database cloud screening results in about 60% removal of clouds
1207 from the complete Sun photometer database and this value is similar to the coverage of clouds globally of
1208 about 68% (Rossow and Schiffer 1999). Autonomous Cimel Sun photometers can view gaps and nearby
1209 regions of the clouds and become inactive during rain periods due to wet sensor activation and AERONET
1210 sites are dominated by land locations which generally have lower cloud cover on average; therefore, these
1211 factors would reduce the difference between total AERONET cloud removal percentage and global satellite
1212 observations. Over 36% of the total data were removed by the 4-quadrant solar tracker sensitivity check
1213 due to less accuracy in tracking the Sun in cloudy conditions, while about 23% of the removal was due to
1214 the variability of clouds with respect to more homogeneous aerosol loading.
- 1215 3. Utilizing the shape of the solar aureole radiances with scattering angle, a cirrus detection algorithm was
1216 developed by leveraging MPLNET LIDAR cloud detection capabilities. The solar aureole cirrus algorithm
1217 eliminates ~5% of the Level 1.0 AOD data to reduce the bias of optically thin cirrus clouds in AERONET
1218 database.
- 1219 4. Spectral temperature correction has been implemented for all AERONET instruments using the sensor head
1220 temperature sensor reading. The temperature characterization shows significant AOD deviation ± 0.01
1221 variation between -25°C and $+50^{\circ}\text{C}$ for the Silicon 1020nm, since this wavelength is on the edge of the
1222 Silicon detector sensitivity range. Other wavelengths in the 440nm to 1640nm range have weak
1223 temperature dependence from -25°C and $+30^{\circ}\text{C}$ with a few wavelengths having greater temperature
1224 dependence at higher temperatures.
- 1225 5. New automated instrument anomaly screening provides a systematic and objective scheme to remove entire
1226 measurements or individual wavelengths from the AERONET AOD database. Importantly, obstructions to
1227 the instrument optics are now removed automatically using an AOD diurnal dependence algorithm based
1228 on the optical air mass. The AOD diurnal dependence technique employs several conditions that were
1229 developed to mitigate the removal of true diurnal dependence conditions while maximizing the removal of
1230 data significantly impacted by anomalies affecting the instrument optics.
- 1231 6. Bias and uncertainty estimates for near real-time AOD are computed by using the difference of the pre-
1232 field calibration AOD minus the interpolated calibration AOD. The near-real time AERONET data have
1233 an estimated bias up to +0.02 and one-sigma uncertainty up to 0.02; these values have slightly higher
1234 uncertainty for shorter wavelengths and slightly lower uncertainty for longer wavelengths.



- 1235 7. The AERONET Version 3 and Version 2 AOD quality controlled databases are analyzed to have a long-
1236 term monthly average difference of $+0.002$ with ± 0.02 standard deviation and greater agreement for time-
1237 matched observations with average difference of -0.002 with ± 0.004 standard deviation. The high
1238 statistical agreement in multi-year monthly averaged AOD validates the advanced automatic data quality
1239 control algorithms and suggests that migrating research to the Version 3 database will corroborate most
1240 Version 2 research results and likely lead to some more accurate results.
- 1241 8. Examination of long-term sites in various aerosol source regions indicates mainly subtle changes in AOD,
1242 AE and the number of days available; however, in some months, improved cloud screening, high aerosol
1243 loading retention, and improved instrument anomaly screening not attained by Version 2 explain larger
1244 deviations in these parameters.

1245
1246 AERONET Version 3 has evolved into a database with unparalleled presence in Sun photometry. Future algorithms
1247 could include improvements to the detection of cirrus clouds in polar environments, where the ice crystal size is
1248 approaching the size of large non-cloud aerosols, the determination of anomalies in high aerosol loading conditions,
1249 and the identification of true AOD diurnal dependence versus one generated by an instrument anomaly. Cimel
1250 radiometers will also measure the moon to derive lunar AOD (Berkoff et al., 2011). For example, current lunar
1251 measurement protocols do not include lunar aureole measurements analogous to the solar aureole measurements,
1252 hence the lack of these measurements potentially reduces the ability of the algorithm to remove cirrus clouds at
1253 night, and thus a variation of the quality control methodology may need to be developed. Other surface-based
1254 remote sensing networks such as MAN (Smirnov et al., 2009), SKYNET (Takamura and Nakajima 2004), and
1255 PANDORA (Herman et al., 2009) may benefit by implementing applicable quality control methods established by
1256 AERONET.

1257
1258 *Data Availability.* Version 3 AOD data are available from the AERONET web site (<https://aeronet.gsfc.nasa.gov>)
1259 and the web site provides these data freely to the public. Data may be acquired by utilizing several download
1260 mechanisms including site-by-site download tools and web service options for near real-time data acquisition.

1261
1262 *Author contributions.* For five years, the AERONET staff (listed from DG to BH) worked individually and
1263 collaboratively drawing on their decades of project scientific, engineering and programming expertise to develop
1264 and assess the Version 3 AOD processing system presented herein. Traditional assignment of co-authorship is not
1265 possible. Aside from the first author, contributing AERONET staff is listed in reverse chronological order based on
1266 their start date with the project. JL, JC, and EW provided LIDAR data for development of the cirrus curvature
1267 methodology. SK and AL provided gaseous and water vapor absorption coefficients based on radiative transfer
1268 models.

1269
1270 *Competing interests:* The authors declare that they have no conflict of interest.

1271



1272 *Acknowledgements.* The AERONET and MPLNET projects at NASA GSFC are supported by the Earth Observing
1273 System Program Science Office Cal-Val, Radiation Science program at NASA headquarters, and various field
1274 campaigns. NCEP Reanalysis data are obtained routinely from the U.S. National Weather Service Climate
1275 Prediction Center. We would like to thank Edward Celarier for several discussions and providing the OMI NO₂
1276 monthly climatology. Fred Espenak and Chris O'Byrne (NASA GSFC) provided solar and lunar eclipse predictions
1277 and the Eclipse Explorer software.

1278

1279 We thank the MPLNET PIs for their effort in establishing and maintaining the sites: Arnon Karnieli
1280 (SEDE_BOKER); Sachi Tripathi (Kanpur); Greg Schuster (COVE); Margarita Yela Gonzalez (Santa Cruz
1281 Tenerife); and John Barnes (Trinidad Head).

1282

1283 The authors thank the AERONET calibration facilities in the USA (NASA GSFC, NOAA Mauna Loa Observatory,
1284 and NEON), France (PHOTONS), and Spain (RIMA and Izana). We thank the following AERONET PIs and their
1285 staff for maintaining the sites and contributing aerosol data: Norm O'Neill, Ihab Abboud and Vitali Fioletov
1286 (PEARL, Toronto, Bratts Lake); Itaru Sano (Osaka); Paulo Artaxo (Rio Branco); Neng-Huei Lin (Lulin); Pucai
1287 Wang and Xiangao Xia (XiangHe); Mikhail Panchenko (Ussurisyk); Arnon Karnieli (SEDE BOKER); Emilio
1288 Cuevas-Agullo (Santa Cruz Tenerife); Joseph Prospero (Ragged Point); Soo-Chin Liew and Santo Salinas Cortijo
1289 (Singapore); S. N. Tripathi (Kanpur); Francisco Reyes (Malaga); and Jean Rajot and Beatrice Marticorena (IER-
1290 Cinzana). A special acknowledgement is given to the AERONET principal investigators and their site staff around
1291 the world who participate in monitoring aerosols to expand our scientific understanding of the Earth.



1292 References

- 1293 Andrews, E., Ogren, J. A., Kinne, S., and Samset, B.: Comparison of AOD, AAOD and column single scattering
1294 albedo from AERONET retrievals and in situ profiling measurements, *Atmos. Chem. Phys.*, 17, 6041–
1295 6072, <https://doi.org/10.5194/acp-17-6041-2017>, 2017.
- 1296 Ångström, A.: Apparent solar constant variations and their relation to variability of atmospheric transmission,
1297 *Tellus*, 22, 205–218, <https://doi.org/10.3402/tellusa.v22i2.10215>, 1970.
- 1298 Berkoff, T.A., Sorokin, M., Stone, T., Eck, T.F., Hoff, R., Welton, E., and Holben, B.: Nocturnal Aerosol Optical
1299 Depth Measurements with a Small-Aperture Automated Photometer Using the Moon as a Light Source. *J.*
1300 *Atmos. Ocean. Tech.*, 28, 1297–1306, <https://doi.org/10.1175/JTECH-D-10-05036.1>, 2011.
- 1301 Bodhaine, B. A., Wood, N. B., Dutton, E. G., Slusser, J. R.: On Rayleigh Optical Depth Calculations, *J. Atmos.*
1302 *Ocean. Tech.*, 16, 1854–1861, [https://doi.org/10.1175/1520-0426\(1999\)016%3C1854:ORODC%3E2.0.CO;2](https://doi.org/10.1175/1520-0426(1999)016%3C1854:ORODC%3E2.0.CO;2), 1999.
- 1304 Boersma, K. F., H. J. Eskes, and E. J. Brinksma: Error analysis for tropospheric NO₂ retrieval from space, *J.*
1305 *Geophys. Res.*, 109, D04311, <https://doi.org/10.1029/2003JD003962>, 2004.
- 1306 Boersma, K. F., Jacob, D. J., Eskes, H. J., Pinder, R. W., Wang, J., and van der A, R. J.: Intercomparison of
1307 SCIAMACHY and OMI tropospheric NO₂ columns: Observing the diurnal evolution of chemistry and
1308 emissions from space, *J. Geophys. Res.*, 113, D16S26, <https://doi.org/10.1029/2007JD008816>, 2008.
- 1309 Bruegge, C. J., Conel, J. E., Green, R. O., Margolis, J. S., Holm, R. G., and Toon, G.: Water vapor column
1310 abundance retrievals during FIFE, *J. Geophys. Res.*, 97(D17), 18759–18768,
1311 <https://doi.org/10.1029/92JD01050>, 1992.
- 1312 Burrows, J. P., Dehn, A., Deters, B., Himmelmann, S., Richter, A., Voigt, S. and Orphal, J.: Atmospheric Remote-
1313 Sensing Reference Data from GOME: Part 1. Temperature-Dependent Absorption Cross-sections of NO₂
1314 in the 231–794 nm Range, *JQSRT*, 60, 1025–1031, [https://doi.org/10.1016/S0022-4073\(97\)00197-0](https://doi.org/10.1016/S0022-4073(97)00197-0), 1998.
- 1315 Burrows, J. P., Richter, A., Dehn, A., Deters, B., Himmelmann, S., Voigt, S. and Orphal J.: Atmospheric remote-
1316 sensing reference data from GOME – 2. Temperature-dependent absorption cross sections of O₃ in the 231–
1317 794 nm range, *J. Quant. Spectrosc. Ra.*, 61, 509–517, [https://doi.org/10.1016/S0022-4073\(98\)00037-5](https://doi.org/10.1016/S0022-4073(98)00037-5),
1318 1999.
- 1319 Cachorro, V. E., Romero, P. M., Toledano, C., Cuevas, E., and de Frutos, A. M.: The fictitious diurnal cycle of
1320 aerosol optical depth: A new approach for “in situ” calibration and correction of AOD data series,
1321 *Geophys. Res. Lett.*, 31, L12106, <https://doi.org/10.1029/2004GL019651>, 2004.
- 1322 Campbell, J.R., Hlavka, D. L., Welton, E. J., Flynn, C. J., Turner, D. D., Spinhirne, J. D., Scott, V.S., and Hwang,
1323 I.H.: Full-time, Eye-Safe Cloud and Aerosol Lidar Observation at Atmospheric Radiation Measurement
1324 Program Sites: Instrument and Data Processing, *J. Atmos. Ocean. Tech.*, 19, 431–442,
1325 [https://doi.org/10.1175/1520-0426\(2002\)019%3C0431:FTESCA%3E2.0.CO;2](https://doi.org/10.1175/1520-0426(2002)019%3C0431:FTESCA%3E2.0.CO;2), 2002.
- 1326 Campbell, J. R., Vaughan, M. A., Oo, M., Holz, R. E., Lewis, J. R., and Welton, E. J.: Distinguishing cirrus cloud
1327 presence in autonomous lidar measurements, *Atmos. Meas. Tech.*, 8, 435–449, <https://doi.org/10.5194/amt-8-435-2015>, 2015.



- 1329 Cavalieri, O., Cairo, F., Fierli, F., Di Donfrancesco, G., Snels, M., Viterbini, M., Cardillo, F., Chatenet, B.,
1330 Formenti, P., Marticorena, B., and Rajot, J. L.: Variability of aerosol vertical distribution in the Sahel,
1331 Atmos. Chem. Phys., 10, 12005–12023, <https://doi.org/10.5194/acp-10-12005-2010>, 2010.
- 1332 Chew, B. N., Campbell, J. R., Reid, J. S., Giles, D. M., Welton, E. J., Salinas, S. V., and Liew, S. C.: Tropical cirrus
1333 cloud contamination in sun photometer data, Atmos. Environ., 45, 6724–6731,
1334 <https://doi.org/10.1016/j.atmosenv.2011.08.017>, 2011.
- 1335 Clough, S. A., F. X. Kneizys, and R. W. Davies: Line shape and the water vapor continuum, Atmos. Res., 23, 229–
1336 241, [https://doi.org/10.1016/0169-8095\(89\)90020-3](https://doi.org/10.1016/0169-8095(89)90020-3), 1989.
- 1337 Coddington, Lean, O., J., Pilewskie, P., Snow, M., and Lindholm, D.: A solar irradiance climate data record, Bull.
1338 Amer. Meteor. Soc., <https://doi.org/10.1175/BAMS-D-14-00265.1>, 2016.
- 1339 DeVore, J.G., Stair, A.T., LePage, A., Rall, D., Atkinson, J., Villanucci, D., Rappaport, S.A., Joss, P.C., and
1340 McClatchey, R.A.: Retrieving Properties of Thin Clouds from Solar Aureole Measurements. J. Atmos.
1341 Oceanic Technol., 26, 2531–2548, <https://doi.org/10.1175/2009JTECHA1289.1>, 2009.
- 1342 DeVore, J. G., Stair Jr., A. T., LePage, A. J., and Villanucci, D.: Using scattering calculations to compare MODIS
1343 retrievals of thin cirrus optical properties with SAM solar disk and aureole radiance measurements, J.
1344 Geophys. Res., 117, D01204, <https://doi.org/10.1029/2011JD015858>, 2012.
- 1345 Dubovik, O. V., Lapyonok, T. V. and Oshchepkov, S. L.: Improved technique for data inversion: optical sizing of
1346 multicomponent aerosols, Appl.Opt., 34, 8422–8436, <https://doi.org/10.1364/AO.34.008422>, 1995.
- 1347 Dubovik, O. and King, M. D.: A flexible inversion algorithm for retrieval of aerosol optical properties from Sun and
1348 sky radiance measurements, J. Geophys. Res., 105, 20 673–20 696, <https://doi.org/10.1029/2000JD900282>,
1349 2000.
- 1350 Eck, T. F., Holben, B. N., Reid, J. S., Dubovik, O., Smirnov, A., O'Neill, N. T., Slutsker, I., and Kinne, S.:
1351 Wavelength dependence of the optical depth of biomass burning, urban, and desert dust aerosols, J.
1352 Geophys. Res., 104(D24), 31333–31349, <https://doi.org/10.1029/1999JD900923>, 1999.
- 1353 Eck, T. F., Holben, B. N., Reid, J. S., Arola, A., Ferrare, R. A., Hostetler, C. A., Crumeyrolle, S. N., Berkoff, T. A.,
1354 Welton, E. J., Lolli, S., Lyapustin, A., Wang, Y., Schafer, J. S., Giles, D. M., Anderson, B. E., Thornhill, K.
1355 L., Minnis, P., Pickering, K. E., Loughner, C. P., Smirnov, A., and Sinyuk, A.: Observations of rapid
1356 aerosol optical depth enhancements in the vicinity of polluted cumulus clouds, Atmos. Chem. Phys., 14,
1357 11633–11656, doi: 10.5194/acp-14-11633-2014, 2014.
- 1358 Eck, T. F., Holben, B. N., Reid, J. S., Xian, P., Giles, D. M., Sinyuk, A., Smirnov, A., Schafer, J. S., Slutsker, I.,
1359 Kim, J., Koo, J.-H., Choi, M., Kim, K. C., Sano, I., Arola, A., Sayer, A. M., Levy, R. C., Munchak, L. A.,
1360 O'Neill, N. T., Lyapustin, A., Hsu, N. C., Randles, C. A., Da Silva, A. M., Burchard, V., Govindaraju, R.
1361 C., Hyer E., Crawford, J. H., Wang, P., and Xia, X.: Observations of the interaction and transport of fine
1362 mode aerosols with cloud and/or fog in Northeast Asia from Aerosol Robotic Network and satellite remote
1363 sensing, J. Geophys. Res. Atmos., 123, 5560–5587. <https://doi.org/10.1029/2018JD028313>, 2018.
- 1364 Eiden R.: Calculations and measurements of the spectral radiance of the solar aureole, Tellus, 20:3, 380–399, doi:
1365 10.3402/tellusa.v20i3.10017, 1968.



- 1366 Espenak, F., and Meeus, J.: Five Millennium Cannon of Solar Eclipses: –1999 to +3000 (2000 BCE to 3000 CE),
1367 NASA Technical Publication TP-2006-214141, NASA, Greenbelt, MD, 2006.
- 1368 Gamache, R. R., Roller, C., Lopes, E., Gordon, I. E., Rothman, L. S., Polyansky, O. L., Zobov, N. F., Kyuberis, A.
1369 A., Tennyson, J., Yurchenko, S. N., Csaszar, A. G., Furtenbacher, T., Huang, X., Schwenke, D. W., Lee, T.
1370 J., Drouin, B. J., Tashkun, S. A., Perevalov, V. I., Kochanov, R. V.: Total internal partition sums for 166
1371 isotopologues of 51 molecules important in planetary atmospheres: Application to HITRAN2016 and
1372 beyond, *J. Quant. Spectrosc. Ra.*, <https://doi.org/10.1016/j.jqsrt.2017.03.045>, 2017.
- 1373 Giles, D. M., Holben, B. N., Eck, T. F., Sinyuk, A., Smirnov, A., Slutsker, I., Dickerson, R. R., Thompson, A. M.,
1374 and Schafer, J. S.: An analysis of AERONET aerosol absorption properties and classifications
1375 representative of aerosol source regions, *J. Geophys. Res.*, 117, D17203,
1376 <https://doi.org/10.1029/2012JD018127>, 2012.
- 1377 Haapanala, P., Räisänen, P., McFarquhar, G. M., Tiira, J., Macke, A., Kahnert, M., Nousiainen, T.: Disk and
1378 circumsolar radiances in the presence of ice clouds, *Atmos. Chem. Phys.*, 17(11), 6865–6882, doi:
1379 <https://dx.doi.org/10.5194/acp-17-6865-2017>, 2017.
- 1380 Halthore, R. N., Eck, T. F., Holben, B. N., and Markham, B. L.: Sun photometric measurements of atmospheric
1381 water vapor column abundance in the 940-nm band, *J. Geophys. Res.*, 102(D4), 4343–4352,
1382 <https://doi.org/10.1029/96JD03247>, 1997.
- 1383 Hamonou, Chazette, E., P., Balis, D., Dulac, F., Schneider, X., Galani, E., Ancellet, G., and Papayannis, A.:
1384 Characterization of the vertical structure of Saharan dust export to the Mediterranean basin, *J. Geophys.*
1385 *Res.*, 104(D18), 22257–22270, <https://doi.org/10.1029/1999JD900257>, 1999.
- 1386 Herman, J., Cede, A., Spinei, E., Mount, G., Tzortziou, M., and Abuhassan, N.: NO₂ column amounts from ground-
1387 based Pandora and MFDOAS spectrometers using the direct-sun DOAS technique: Intercomparisons and
1388 application to OMI validation, *J. Geophys. Res.*, 114, D13307, <https://doi.org/10.1029/2009JD011848>,
1389 2009.
- 1390 Holben, B. N., Vermote, E., Kaufman, Y. J., Tanre, D. and Kalb, V.: Aerosol retrieval over land from AVHRR data-
1391 application for atmospheric correction, *IEEE T. Geosci. Remote*, 30, 212–222,
1392 <https://doi.org/10.1109/36.134072>, 1992.
- 1393 Holben, B. N., Eck, T. F., Slutsker, I., Tanre, D., Buis, J. P., Setzer, A., Vermote, E., Reagan, J. A., Kaufman, Y.,
1394 Nakajima, T., Lavenue, F., Jankowiak, I., and Smirnov, A.: AERONET–A federated instrument network
1395 and data archive for aerosol characterization, *Remote Sens. Environ.*, 66, 1–16,
1396 [https://doi.org/10.1016/S0034-4257\(98\)00031-5](https://doi.org/10.1016/S0034-4257(98)00031-5), 1998.
- 1397 Holben, B. N., Tanre, D., Smirnov, A., Eck, T. F., Slutsker, I., Abuhassan, N., Newcomb, W. W., Schafer, J.,
1398 Chatenet, B., Lavenue, F., Kaufman, Y., Vande Castle, J., Setzer, A., Markham, B., Clark, D., Frouin, R.,
1399 Halthore, R., Karnieli, A., O’Neill, N. T., Pietras, C., Pinker, R. T., Voss, K. and Zibordi, G.: An emerging
1400 ground-based aerosol climatology: Aerosol optical depth from AERONET, *J. Geophys. Res.*, 106(D11),
1401 12,067–12,097, <https://doi.org/10.1029/2001JD900014>, 2001.



- 1402 Holben, B. N., Eck, T. F., Slutsker, I., Smirnov, A., Sinyuk, A., Schafer, J., Giles, D., and Dubovik, O.: Aeronet's
1403 Version 2.0 quality assurance criteria, Proc. SPIE, 6408, Conf. on Remote Sensing of the Atmosphere and
1404 Clouds, 64080Q, <https://doi.org/10.1117/12.706524>, 2006.
- 1405 Huang, J., Hsu, N., Tsay, S.-C., Jeong, M.-J., Holben, B. N., Berkoff, T. A., and Welton, E. J.: Susceptibility of
1406 aerosol optical thickness retrievals to thin cirrus contamination during the BASE-ASIA campaign, J.
1407 Geophys. Res., 116, D08214, <https://doi.org/10.1029/2010JD014910>, 2011.
- 1408 Ingold, T., Schmid, B., Mätzler, C., Demoulin, P., and Kämpfer, N.: Modeled and empirical approaches for
1409 retrieving columnar water vapor from solar transmittance measurements in the 0.72, 0.82 and 0.94- μm
1410 absorption bands, J. Geophys. Res., 105, 24,327–24,343, <https://doi.org/10.1029/2000JD900392>, 2000.
- 1411 Kahn, R. A., and Gaitley, B. J.: An analysis of global aerosol type as retrieved by MISR, J. Geophys. Res. Atmos.,
1412 120, 4248–4281, <https://doi.org/10.1002/2015JD023322>, 2015.
- 1413 Kasten, F.: A new table and approximation formula for relative optical air mass, Arch. Meteorol. Geophys.
1414 Bioklimatol. Ser. B, 14, 206–223, <https://doi.org/10.1007/BF02248840>, 1965.
- 1415 Kasten, F. and Young, A. T.: Revised optical air mass tables and approximation formula, Appl. Opt., 28, 4735–
1416 4738, <https://doi.org/10.1364/AO.28.004735>, 1989.
- 1417 Kalnay, E., Kanamitsu, M., Kistler, R., Collins, W., Deaven, D., Gandin, L., Iredell, M., Saha, S., White, G.,
1418 Woollen, J., Zhu, Y., Chelliah, M., Ebisuzaki, W., Higgins, W., Janowiak, J., Mo, K. C., Ropelewski, C.,
1419 Wang, J., Leetmaa, A., Reynolds, R., Jenne, R. and Joseph, D.: The NCEP/NCAR 40-Year Reanalysis
1420 Project, Bull. Amer. Meteor. Soc., 77, 437–471, [https://doi.org/10.1175/1520-0477\(1996\)077%3C0437:TNYRP%3E2.0.CO;2](https://doi.org/10.1175/1520-0477(1996)077%3C0437:TNYRP%3E2.0.CO;2), 1996.
- 1422 Kaufman, Y. J., Remer, L. A., Tanre, D., Li, R.-R., Kleidman, R., Mattoo, S., Levy, R. C., Eck, T. F., Holben, B. N.,
1423 Ichoku, C., Martins, J. V., and Koren, I.: A Critical Examination of the Residual Cloud Contamination and
1424 Diurnal Sampling Effects on MODS Estimates of Aerosol Over Ocean, IEEE T. Geosci. Remote, 43,
1425 <https://doi.org/10.1109/TGRS.2005.858430>, 2005.
- 1426 Kinne, S., Akerman, T. P., Shiobara, M., Uchiyama, A., Heymsfield, A. J., Miloshevich, L., Wendell, J., Eloranta,
1427 E., Purgold, C., and Bergstrom, R. W.: Cirrus cloud radiative and microphysical properties from ground
1428 observations and in situ measurements during FIRE 1991 and their application to exhibit problems in cirrus
1429 solar radiative transfer modeling, J. Atmos. Sci., 54, 2320–2344, [https://doi.org/10.1175/1520-0469\(1997\)054%3C2320:CCRAMP%3E2.0.CO;2](https://doi.org/10.1175/1520-0469(1997)054%3C2320:CCRAMP%3E2.0.CO;2), 1997
- 1431 Kline, Morris: Calculus: An Intuitive and Physical Approach, Dover. 457–461, ISBN 978-0-486-40453-0, 1998.
- 1432 Komhyr, W. D., Grass, K. D., and Leonard, R. K.: Dobson Spectrophotometer 83: a standard for total ozone
1433 measurements, 1962–1987, J. Geophys. Res., 94, 9847–9861, <https://doi.org/10.1029/JD094iD07p09847>,
1434 1989.
- 1435 Levy, R. C., Remer, L. A., Kleidman, R. G., Mattoo, S., Ichoku, C., Kahn, R., and Eck, T. F.: Global evaluation of
1436 the Collection 5 MODIS dark-target aerosol products over land, Atmos. Chem. Phys., 10, 10399–10420,
1437 <https://doi.org/10.5194/acp-10-10399-2010>, 2010.



- 1438 Levy, R. C., Mattoo, S., Munchak, L. A., Remer, L. A., Sayer, A. M., Patadia, F., and Hsu, N. C.: The Collection 6
1439 MODIS aerosol products over land and ocean, Atmos. Meas. Tech., 6, 2989–3034,
1440 <https://doi.org/10.5194/amt-6-2989-2013>, 2013.
- 1441 Lewis, J., Campbell, J., Welton, E. J., Stewart, S. A., and Haftings, P. C.: Overview of MPLNET Version 3 Cloud
1442 Detection, J. Atmos. Ocean Tech., <https://doi.org/10.1175/JTECH-D-15-0190.1>, 2016.
- 1443 Li, Z., Zhao, X., Kahn, R., Mishchenko, M., Remer, L., Lee, K.-H., Wang, M., Laszlo, I., Nakajima, T., and Maring,
1444 H.: Uncertainties in satellite remote sensing of aerosols and impact on monitoring its long-term trend: a
1445 review and perspective, Ann. Geophys., 27, 2755–2770, <https://doi.org/10.5194/angeo-27-2755-2009>,
1446 2009.
- 1447 Li, Z., Xia, X., Cribb, M., Mi, W., Holben, B., Wang, P., Chen, H., Tsay S.-C., Eck, T. F., Zhao, F., Dutton, E. G.
1448 and Dickerson, R. E.: Aerosol optical properties and their radiative effects in northern China, J. Geophys.
1449 Res., 112, D22S01, <https://doi.org/10.1029/2006JD007382>, 2007.
- 1450 Lin, N.-H., S.-C. Tsay, H. B. Maring, M.-C. Yen, G.-R. Sheu, S.-H. Wang, et al.: An overview of regional
1451 experiments on biomass burning aerosols and related pollutants in Southeast Asia: From BASE-ASIA and
1452 the Dongsha Experiment to 7-SEAS, Atmos. Environ., 78, 1–19,
1453 <https://doi.org/10.1016/j.atmosenv.2013.04.066>, 2013.
- 1454 Martins, J. V., Tanré, D., Remer, L., Kaufman, Y., Mattoo, S., and Levy, R.: MODIS Cloud screening for remote
1455 sensing of aerosols over oceans using spatial variability, Geophys. Res. Lett., 29(12),
1456 <https://doi.org/10.1029/2001GL013252>, 2002.
- 1457 McPeters, R. D., Frith, S., and Labow, G. J.: OMI total column ozone: extending the long-term data record, Atmos.
1458 Meas. Tech., 8, 4845–4850, <https://doi.org/10.5194/amt-8-4845-2015>, 2015.
- 1459 Michalsky, J.: The astronomical almanac's algorithm for approximate solar position (1950–2030), Solar Energy, 40,
1460 227–235, [https://doi.org/10.1016/0038-092X\(88\)90045-X](https://doi.org/10.1016/0038-092X(88)90045-X), 1988.
- 1461 Michalsky, J. J., J.C. Liljegren and Harrison, L. C: A Comparison of Sun Photometer Derivations of Total Column
1462 Water Vapor and Ozone to Standard Measures of Same at the Southern Great Plains Atmospheric
1463 Radiation Measurement Site, J. Geophys. Res., 100, 25995–26003, <https://doi.org/10.1029/95JD02706>,
1464 1995.
- 1465 Mlawer, E. J., V. H. Payne, J.-L. Moncet, J. S. Delamere, M. J. Alvarado and D. D. Tobin: Development and recent
1466 evaluation of the MT_CKD model of continuum absorption, Phil. Trans. Roy. Soc. A, 370, 1–37,
1467 <https://doi.org/10.1098/rsta.2011.0295>, 2012.
- 1468 Nakajima, T., Tonna, G., Rao, R., Boi, P., Kaufman, Y., and Holben, B.: Use of sky brightness measurements from
1469 ground for remote sensing of particulate polydispersions, Appl. Opt. 35, 2672–2686,
1470 <https://doi.org/10.1364/AO.35.002672>, 1996.
- 1471 Omar, A. H., Winker, D. M., Tackett, J. L., Giles, D. M., Kar, J., Liu, Z., Vaughan, M. A., Powell, K. A., and
1472 Trepte, C. R., CALIOP and AERONET aerosol optical depth comparisons: One size fits none, J. Geophys.
1473 Res. Atmos., 118, 4748–4766, <https://doi.org/10.1002/jgrd.50330>, 2013.



- 1474 O'Neill, N. T., Eck, T. F., Holben, B. N., Smirnov, A., Dubovik, O., and Royer, A.: Bimodal size distribution
1475 influences on the variation of Angstrom derivatives in spectral and optical depth space, *J. Geophys. Res.*,
1476 106, 9787–9806, <https://doi.org/10.1029/2000JD900245>, 2001.
- 1477 O'Neill, N. T., Eck, T. F., Smirnov, A., Holben, B. N., and Thulasiraman, S.: Spectral discrimination of coarse and
1478 fine mode optical depth, *J. Geophys. Res.*, 108, D17, 4559–4573, <https://doi.org/10.1029/2002JD002975>,
1479 2003.
- 1480 O'Neill, N. T., Eck, T. F., Reid, J. S., Smirnov, A., and Pancrati, O.: Coarse mode optical information retrievable
1481 using ultraviolet to short-wave infrared Sun photometry: Application to United Arab Emirates Unified
1482 Aerosol Experiment data, *J. Geophys. Res.*, 113, D05212, <https://doi.org/10.1029/2007JD009052>, 2008.
- 1483 Redemann, J., Masonis, S. J., Schmid, B., Anderson, T. L., Russell, P. B., Livingston, J. M., Dubovik, O., and
1484 Clarke, A. D.: Clear-column closure studies of aerosols and water vapor aboard the NCAR C-130 during
1485 ACE-Asia, 2001, *J. Geophys. Res.*, 108(D23), 8655, <https://doi.org/10.1029/2003JD003442>, 2003.
- 1486 Remer, L. A., Kaufman, Y. J., Tanré, D., Mattoo, S., Chu, D. A., Martins, J. V., Li, R., Ichoku, C., Levy, R. C.,
1487 Kleidman, R. G., Eck, T. F., Vermote, E., and Holben, B. N.: The MODIS Aerosol Algorithm, Products,
1488 and Validation. *J. Atmos. Sci.*, 62, 947–973, <https://doi.org/10.1175/JAS3385.1>, 2005.
- 1489 Rossow, W. B. and Schiffer, R. A.: Advances in Understanding Clouds from ISCCP. *Bull. Amer. Meteor. Soc.*, 80,
1490 2261–2288, [https://doi.org/10.1175/1520-0477\(1999\)080<2261:AIUCFI>2.0.CO;2](https://doi.org/10.1175/1520-0477(1999)080<2261:AIUCFI>2.0.CO;2), 1999.
- 1491 Russell, P. B., Livingston, J. M., Dutton, E. G., Pueschel, R. F., Reagen, J. A., DeFoor, T. E., Box, M. A., Allen, D.,
1492 Pilewskie, P., Herman, B. M., Kinne, S. A. and Hoffman, D. J.: Pinatubo and pre-Pinatubo optical-depth
1493 spectra: Mauna Loa measurements, comparisons, inferred particle size distributions, radiative effects, and
1494 relationship to lidar data, *J. Geophys. Res.*, 98(D12), 22969–22985, <https://doi.org/10.1029/93JD02308>,
1495 1993.
- 1496 Sassen, K., and Campbell, J. R.: A midlatitude cirrus cloud climatology from the Facility for Atmospheric Remote
1497 Sensing. Part I: Macrophysical and synoptic properties, *J. Atmos. Sci.*, 58, 481–496,
1498 [https://doi.org/10.1175/1520-0469\(2001\)058%3C0481:AMCCCF%3E2.0.CO;2](https://doi.org/10.1175/1520-0469(2001)058%3C0481:AMCCCF%3E2.0.CO;2), 2001.
- 1499 Sayer, A. M., Hsu, N. C., Bettenhausen, C., and Jeong, M.-J.: Validation and uncertainty estimates for MODIS
1500 Collection 6 “Deep Blue” aerosol data, *J. Geophys. Res. Atmos.*, 118, 7864–7872,
1501 <https://doi.org/10.1002/jgrd.50600>, 2013.
- 1502 Schmid, B., Thome, K.J., Demoulin, P., Peter, R., Matzler, C., and Sekler, J.: Comparison of modeled and empirical
1503 approaches for retrieving columnar water vapor from solar transmittance measurements in the 0.94 micron
1504 region, *J. Geophys. Res.*, 101, 9345–9358, <https://doi.org/10.1029/96JD00337>, 1996.
- 1505 Schmid, B., Michalsky, J. J., Slater, D. W., Barnard, J. C., Halthore, R. N., Liljegren, J. C., Holben, B. N., Eck, T. F.,
1506 Livingston, J. M., Russell, P. B., Ingold, T., and Slutsker, I.: Comparison of Columnar Water-Vapor
1507 Measurements from Solar Transmittance Methods, *Appl. Opt.* 40, 1886–1896,
1508 <https://doi.org/10.1364/AO.40.001886>, 2001.



- 1509 Shaw, G. E., Reagan, J. A., and Herman, B. M.: Investigations of atmospheric extinction using solar radiation
1510 measurements made with multiple wavelength radiometer, *J. Appl. Meteorol.*, 12, 374–380,
1511 [https://doi.org/10.1175/1520-0450\(1973\)012%3C0374:IOAEUD%3E2.0.CO;2](https://doi.org/10.1175/1520-0450(1973)012%3C0374:IOAEUD%3E2.0.CO;2), 1973.
- 1512 Shaw, G.E., Sun Photometry, *Bull. Am. Meteor. Soc.*, 64, 4-10, [https://doi.org/10.1175/1520-](https://doi.org/10.1175/1520-0477(1983)064%3C0004:SP%3E2.0.CO;2)
1513 [0477\(1983\)064%3C0004:SP%3E2.0.CO;2](https://doi.org/10.1175/1520-0477(1983)064%3C0004:SP%3E2.0.CO;2), 1983.
- 1514 Sinyuk, A., Holben, B. N., Smirnov, A., Eck, T. F., Slutsker, I., Schafer, J. S., Giles, D. M., and Sorokin, M.:
1515 Assessment of error in aerosol optical depth measured by AERONET due to aerosol forward scattering,
1516 *Geophys. Res. Lett.*, 39, L23806, <https://doi.org/10.1029/2012GL053894>, 2012.
- 1517 Smirnov, A., Holben, B. N., Eck, T. F., Dubovik, O., and Slutsker, I.: Cloud screening and quality control
1518 algorithms for the AERONET database, *Rem. Sens. Env.*, 73, 337-349, [https://doi.org/10.1016/S0034-](https://doi.org/10.1016/S0034-4257(00)00109-7)
1519 [4257\(00\)00109-7](https://doi.org/10.1016/S0034-4257(00)00109-7), 2000.
- 1520 Smirnov, A, Holben, B.N., Lyapustin A., Slutsker, I. and Eck, T.F.: AERONET processing algorithms refinement,
1521 AERONET 2004 Workshop, El Arenosillo, Spain, May 10–14, 2004.
- 1522 Smirnov, A., Holben, B. N., Slutsker, I., Giles, D. M., McClain, C. R., et al.: Maritime Aerosol Network as a
1523 component of Aerosol Robotic Network, *J. Geophys. Res.*, 114, D06204,
1524 <https://doi.org/10.1029/2008JD011257>, 2009.
- 1525 Takamura, T, T. Nakajima and SKYNET community group: Overview of SKYNET and its Activities, *Proceedings*
1526 *of AERONET workshop, El Arenosillo., Optica Pura y Aplicada*, 37, 3303–3308, 2004.
- 1527 Toledano, C., González, R., Fuertes, D., Cuevas, E., Eck, T. F., Kazadzis, S., Kouremeti, N., Gröbner, J., Goloub,
1528 P., Blarel, L., Román, R., Barreto, Á., Holben, B. N., and Cachorro, V. E.: Assessment of Sun photometer
1529 Langley calibration at the high-elevation sites Mauna Loa and Izaña, *Atmos. Chem. Phys. Discuss.*,
1530 <https://doi.org/10.5194/acp-2018-430>, in review, 2018.
- 1531 Tzortziou, M., Herman, J. R., Cede, A., and Abuhassan, N.: High precision, absolute total column ozone
1532 measurements from the Pandora spectrometer system: Comparisons with data from a Brewer double
1533 monochromator and Aura OMI, *J. Geophys. Res.*, 117, D16303, <https://doi.org/10.1029/2012JD017814>,
1534 2012.
- 1535 USNO: Approximate Solar Coordinates derived from The Astronomical Almanac, pg. C5:
1536 <http://aa.usno.navy.mil/faq/docs/SunApprox.php>.
- 1537 Wang S.-H., Tsay, S.-C., Lin, N.-H., Chang, S.-C., C. L., Welton, E. J., Holben, B. N., Hsu, N. C., Lau, W. K. M.,
1538 Lolli, S., Kuo, C.-C., Chia, H.-P., Chiu, C.-Y., Lin, C.-C., Bell, S. W., Ji, Q., Hansell, R. A., Sheu, G.-R.,
1539 Chi, K.-H., and Peng, C.-M.: Origin, transport, and vertical distribution of atmospheric pollutants over the
1540 northern South China Sea during the 7-SEAS/Dongsha Experiment, *Atmospheric Environment*, 78, 124–
1541 133, <https://doi.org/10.1016/j.atmosenv.2012.11.013>, 2013.
- 1542 Welton, E. J., Voss, K. J., Gordon, H. R., Maring, H., Smirnov, A., Holben, B., Schmid, B., Livingston, J. M.,
1543 Russell, P. B., Durkee, P. A., Formenti, P., and Andreae, M. O.: Ground-based Lidar Measurements of
1544 Aerosols During ACE-2: Instrument Description, Results, and Comparisons with other Ground-based and
1545 Airborne Measurements, *Tellus B*, 52, 635–650, <https://doi.org/10.1034/j.1600-0889.2000.00025.x>, 2000.



- 1546 Welton, E.J., and Campbell, J.R.: Micro-pulse Lidar Signals: Uncertainty Analysis, J. Atmos. Oceanic Technol., 19,
1547 2089–2094, [https://doi.org/10.1175/1520-0426\(2002\)019%3C2089:MLSUA%3E2.0.CO;2](https://doi.org/10.1175/1520-0426(2002)019%3C2089:MLSUA%3E2.0.CO;2), 2002.
- 1548 Zibordi, G., Holben, B., Melin, F., D'Alimonte, D., Berthon, J.-F., Slutsker, I., and Giles, D.: AERONET-OC: an
1549 overview, Can. J. Remote Sens., 36, 5, <https://doi.org/10.5589/m10-073>, 2010.
- 1550



Table 1. Nominal AERONET wavelengths for ion assisted deposition filters used for aerosol remote sensing and spectral corrections or components for each channel.

Nominal Central Wavelengths (nm)	Filter Bandpass (nm)	Spectral Corrections/Components
340	2	Rayleigh, NO ₂ , O ₃
380	2	Rayleigh, NO ₂
440	10	Rayleigh, NO ₂
500	10	Rayleigh, NO ₂ , O ₃
675	10	Rayleigh, O ₃
870	10	Rayleigh
935	10	Rayleigh, Aerosol
1020	10	Rayleigh, H ₂ O
1640	25	Rayleigh, H ₂ O, CO ₂ , CH ₄



1555 **Table 2.** Summary of Cloud Screening Related Quality Control Changes from Version 2 to Version 3.

Algorithm/Parameter	Version 2	Version 3
Very High AOD Restoration	N/A	$\tau_{870} > 0.5$; $\alpha_{675-1020} > 1.2$ or $\alpha_{870-1020} > 1.3$, restore if eliminated by cloud screening
Optical Air Mass Range	Maximum of 5.0	Maximum of 7.0
Number of Potential Measurements	$N_{\text{remain}} < 3$, reject all measurements in the day	After all checks applied, reject all measurements in the day if $N_{\text{remain}} < \text{MAX}\{3 \text{ or } 10\% \text{ of } N\}$
Triplet Criterion	All wavelengths checked; AOD Triplet Variability $> \text{MAX}\{0.02 \text{ or } 0.03 * \tau_{\text{aerosol}}\}$	Check only wavelengths 675, 870, and 1020nm; AOD Triplet Variability $> \text{MAX}\{0.01 \text{ or } 0.015 * \tau_{\text{aerosol}}\}$
Ångstrom Exponent (AE) Limitation	N/A	If $\text{AE}_{440-870\text{nm}} < -1.0$ or $\text{AE}_{440-870\text{nm}} > 3.0$, then eliminate triplet measurement.
Smoothness Check	$D < 16$	For AOD _{500nm} (or 440nm) $\Delta\tau_{\text{aerosol}} > 0.01$ per minute, then remove larger τ_{aerosol} in pair. Repeat condition for each pair until points are not removed.
Solar Aureole radiance Curvature Check (Sect. 3.2.2)	N/A	Using 1020nm solar aureole radiances, compute the curvature (k) between 3.2° and 6.0° scattering angle (φ) at the smallest scattering angle. If $k < 2.0E-5 \varphi$ and if slope of curvature (M) is greater than 4.3 (empirically determined), then radiances are cloud contaminated. For sky scan measurements, all τ_{aerosol} measurements are removed within 30 minutes of the sky measurement. For Model T, special aureole scan measurements will remove all τ_{aerosol} within a two minute period superseding any sky scan aureole measurements.
Standalone Measurements	N/A	If no data exists within 1 hour of a measurement, then reject it unless $\text{AE}_{440-870\text{nm}} > 1.0$.
AOD Stability Check	Same as Version 3	Daily averaged AOD 500nm (or 440nm) has σ less than 0.015, then do not perform 3- σ check.
3- σ Check	Same as Version 3	AOD 500nm and $\text{AE}_{440-870\text{nm}}$ should be within the $\text{MEAN} \pm 3\sigma$; otherwise, the points are rejected.

1556

1557



1558 **Table 3.** AERONET and MPLNET sites and date ranges used for assessing cirrus and non-cirrus cloud presence

Site	Latitude	Longitude	Elevation (meters)	Date Range
GSFC	38.9925° N	76.8398° W	87	May 2001–Jan 2013
COVE	36.9000° N	75.7100° W	37	May 2004–Jan 2008
Kanpur	26.5128° N	80.2316° E	123	May 2009–Jan 2013
SEDE_BOKER	30.8550° N	34.7822° E	480	Nov 2007–Apr 2013
Santa_Cruz_Tenerife	28.4725° N	16.2473° W	52	Nov 2005–Jan 2013
Singapore	1.2977° N	103.7804° E	30	Aug 2009–Jan 2013
Ragged_Point	13.1650° N	59.4320° W	40	Jun 2008–Jan 2013
Trinidad_Head	41.0539° N	124.1510° W	105	May 2005–Feb 2013

1559

1560



Table 4. Thresholds used to determine the independent and dependent AOD diurnal dependence. Satisfying both the slope and correlation coefficient (R) conditions would constitute the possible removal of all measurements for a day.

Day Removal Type	AOD Diurnal Shape	Analyzed Period	Slope Threshold	R Threshold
Independent	Concave	AM, PM, Day	>0.25	>0.974
Dependent	Concave	AM, PM	>0.04	>0.94
Dependent	Concave	Day	>0.1	>0.94
Dependent	Convex	AM, PM, Day	<-0.02	<-0.94
Dependent – $\tau_{\text{avg}} < 0.1$	Convex	AM, PM, Day	<-0.1	<-0.94
Independent – 2 or more Silicon wavelengths (440, 675, 870, 1020nm) or 1640nm InGaAs	Concave	AM, PM, Day	>0.1 Day or AM & PM > 0.02	>0.94



Table 5. Statistics corresponding to Fig. 21 and Fig. 22 for AOD interpolated to 500nm, Ångström exponent 440–870nm, precipitable water (cm), and the number of days. Version 3 Level 2.0 and Version 2 Level 2.0 data are compared for the same multi-year monthly averages when sites have a total of more than 1000 days for all months and more than 30 days in each month. Data represented as “Matched” indicates the further condition that the exact observations were matched in Version 2 and Version 3 Level 2.0 multi-year monthly average data sets. Note that PW values for the “Matched” data set are approximately the same as the unmatched data set.

Parameter	AOD _{500nm}	AE _{440-870nm}	PW (cm)	Days	AOD _{500nm}	AE _{440-870nm}
	(V3–V2)	(V3–V2)	(V3–V2)	(V3–V2)	(V3–V2)	(V3–V2)
	Unmatched	Unmatched	Unmatched	Unmatched	Matched	Matched
Average	0.002	–0.01	–0.02	–0.4	–0.002	–0.03
Standard Deviation	0.022	0.10	0.06	24.8	0.004	0.10
Maximum	0.247	0.29	0.34	150	0.015	0.35
Minimum	–0.166	–1.54	–0.45	–130	–0.029	–1.63
Number of Months	2953	2953	2953	2953	2514	2514

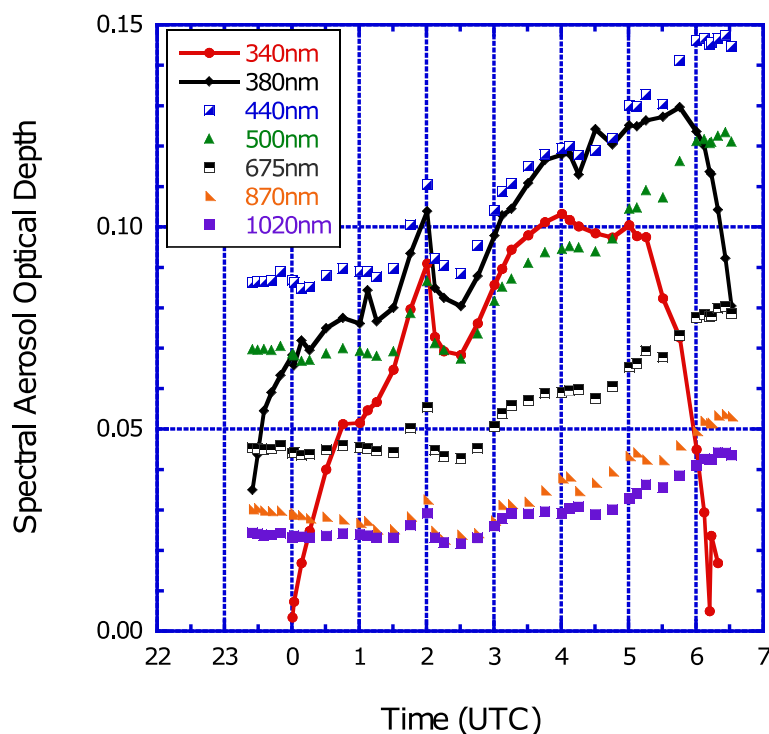


Figure 1. Aerosol optical depth (AOD) data from AERONET Ussuriysk site (43.70° N, 132.16° E) on 30 November 2005 shows electronic instability. For the Cimel Model 4 instruments, the electronic sensitivity of the UV AOD data (340nm and 380nm) can be high due to a bad amplifier. The resulting AOD data for the UV channels are out of spectral dependence the entire day with a maximum error for large optical air mass due to large dark current values. The UV channels (identified by line plots) are removed by the quality control while preserving other wavelengths that are not affected by this condition.

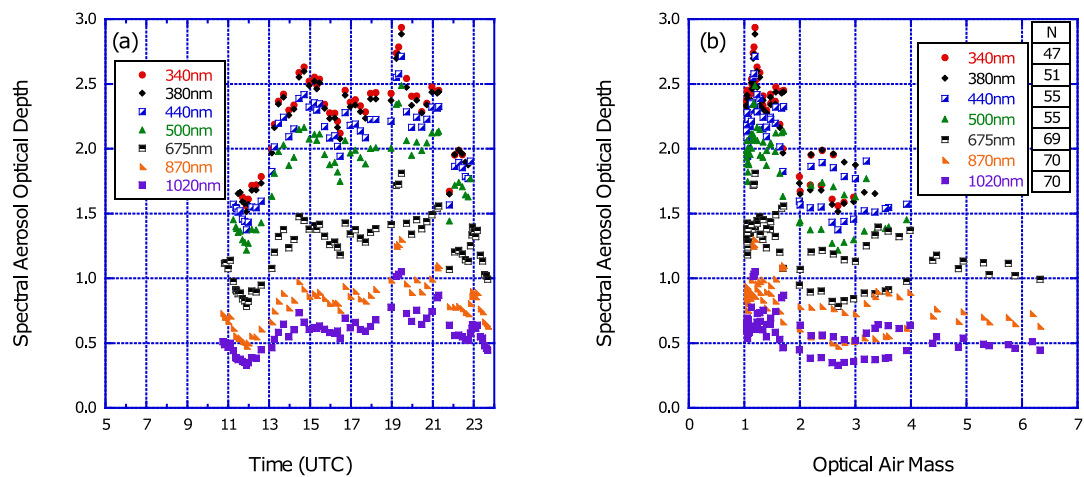


Figure 2. Spectral dependent low digital number removal at NASA Goddard Space Flight Center (GSFC; 38.99°N, 76.84°W). (a) Level 1.0 AOD data from GSFC on 8 July 2002 are plotted for the Quebec forest fire smoke event. Significantly fewer Level 1.0 AOD data are available for the shorter wavelengths near local sunrise (~11 UTC) and sunset (~23:30 UTC). (b) The distribution of the AOD measurements with respect to optical air mass clearly shows the removal of short wavelengths for large air mass in this fine mode aerosol event. The high aerosol loading due to smoke and haze results in significant extinction at UV and visible wavelengths, which corresponds to low digital counts. The low digital count quality control removes AOD measurements impacted by diffuse radiation scattered into the instrument field of view (Sinyuk et al., 2012).

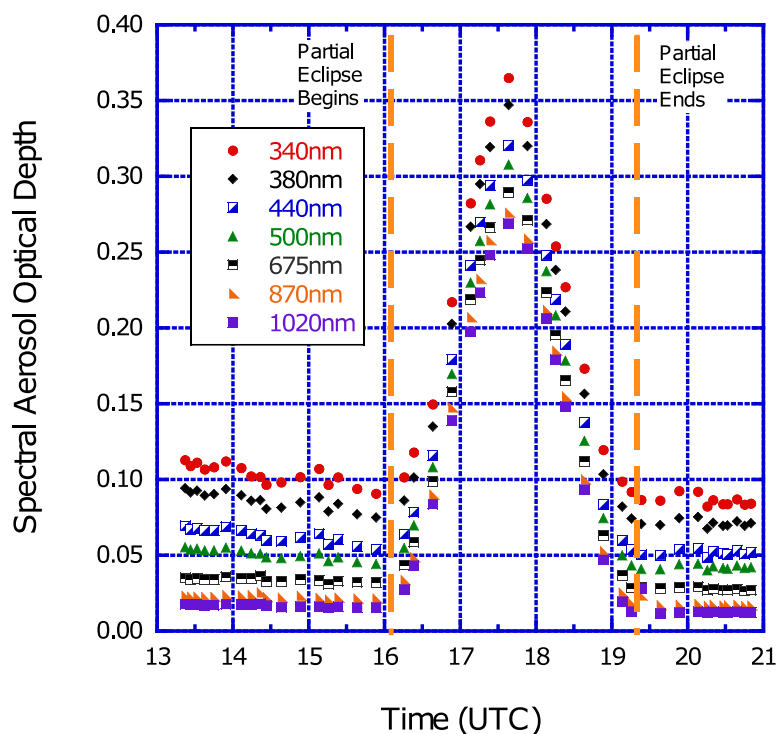


Figure 3. Eclipse circumstance at the NASA Goddard Space Flight Center (GSFC; 38.99° N, 76.84° W) on 25 December 2000 between 16:04:13 UTC and 19:16:25 UTC. The maximum AOD during the eclipse occurs at the maximum obscuration of 0.42, which results in a change of ~0.28 for AOD 500nm compared to data before and after the solar eclipse. Utilizing the NASA Solar Eclipse database, the AOD measurements are removed between the partial eclipse first contact and partial eclipse last contact as denoted by the vertical dashed lines.

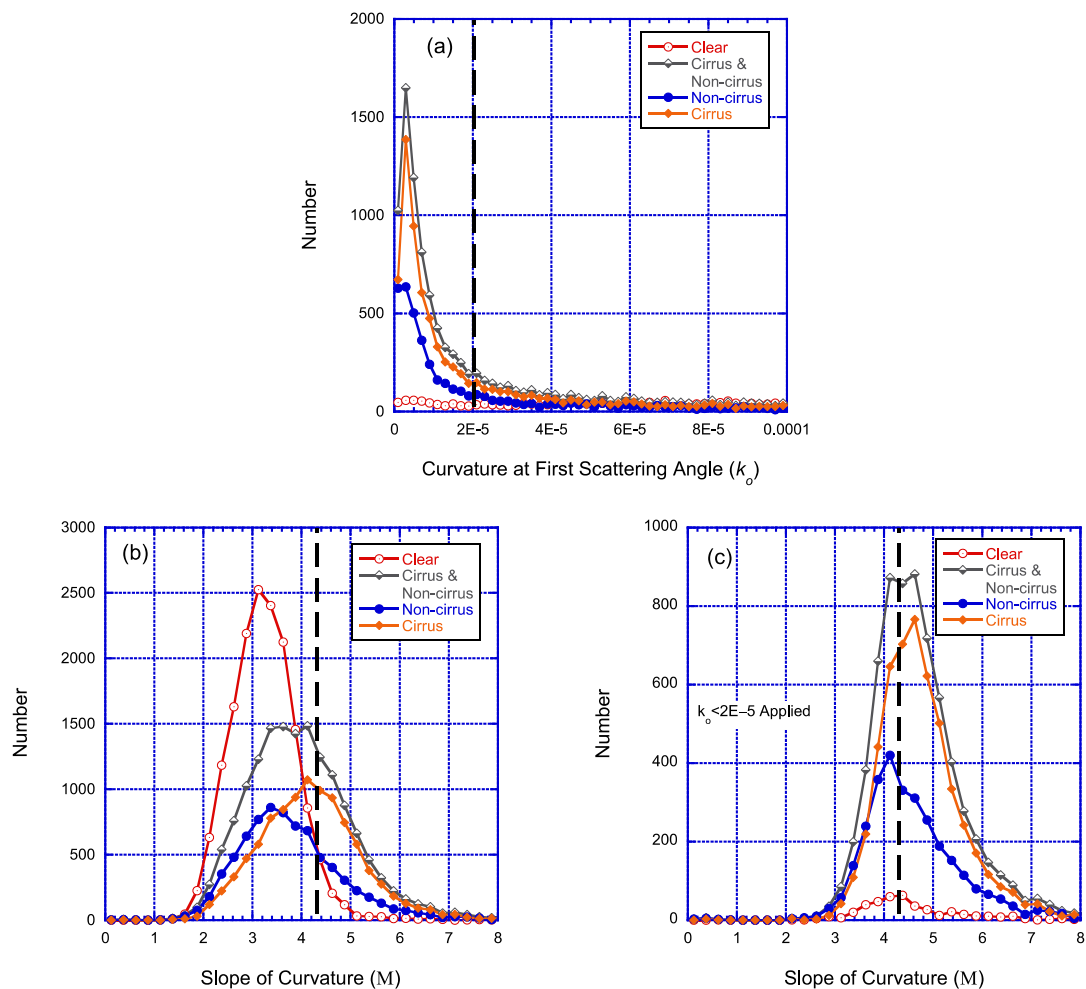


Figure 4. NASA Goddard Space Flight Center (GSFC; 38.99° N, 76.84° W) AERONET data coincident with MPLNET LIDAR derived sky condition categories (Clear, both Cirrus and Non-cirrus clouds, Non-cirrus clouds, and Cirrus clouds) from 2001–2013. The AERONET solar aureole 1020nm radiances are used to calculate the curvature at the first scattering angle (k_o) and the slope of curvature (M) between 3.2° and 6.0° scattering angles. (a) The number distribution of k_o is shown and the dashed vertical line at k_o equals 2E–5 indicates the threshold where values less than 2E–5 are considered possibly cirrus cloud contaminated (the x-axis is truncated at 1E–4 for viewing purposes). (b) The number distribution of M is shown and M greater than 4.3 are considered to be possibly cirrus cloud contaminated (the dashed vertical line indicates the threshold of 4.3). (c) Similar to panel (b) except that the k_o threshold ($k_o < 2E-5$) is applied first and, as a result, data greater than 4.3 in this panel are considered to be cirrus cloud contaminated.

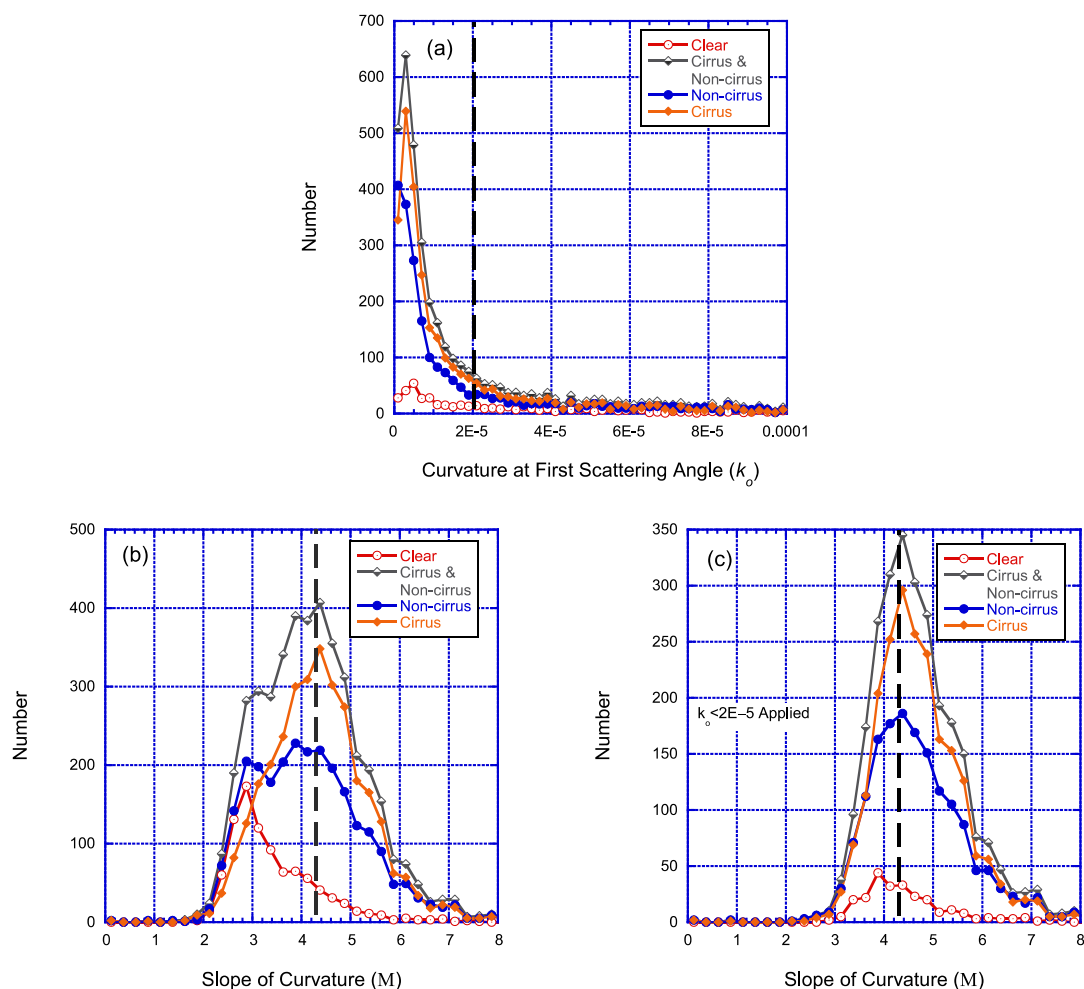


Figure 5. Similar to Fig. 4, except for Singapore (1.29° N, 103.78° E) from 2009–2013.

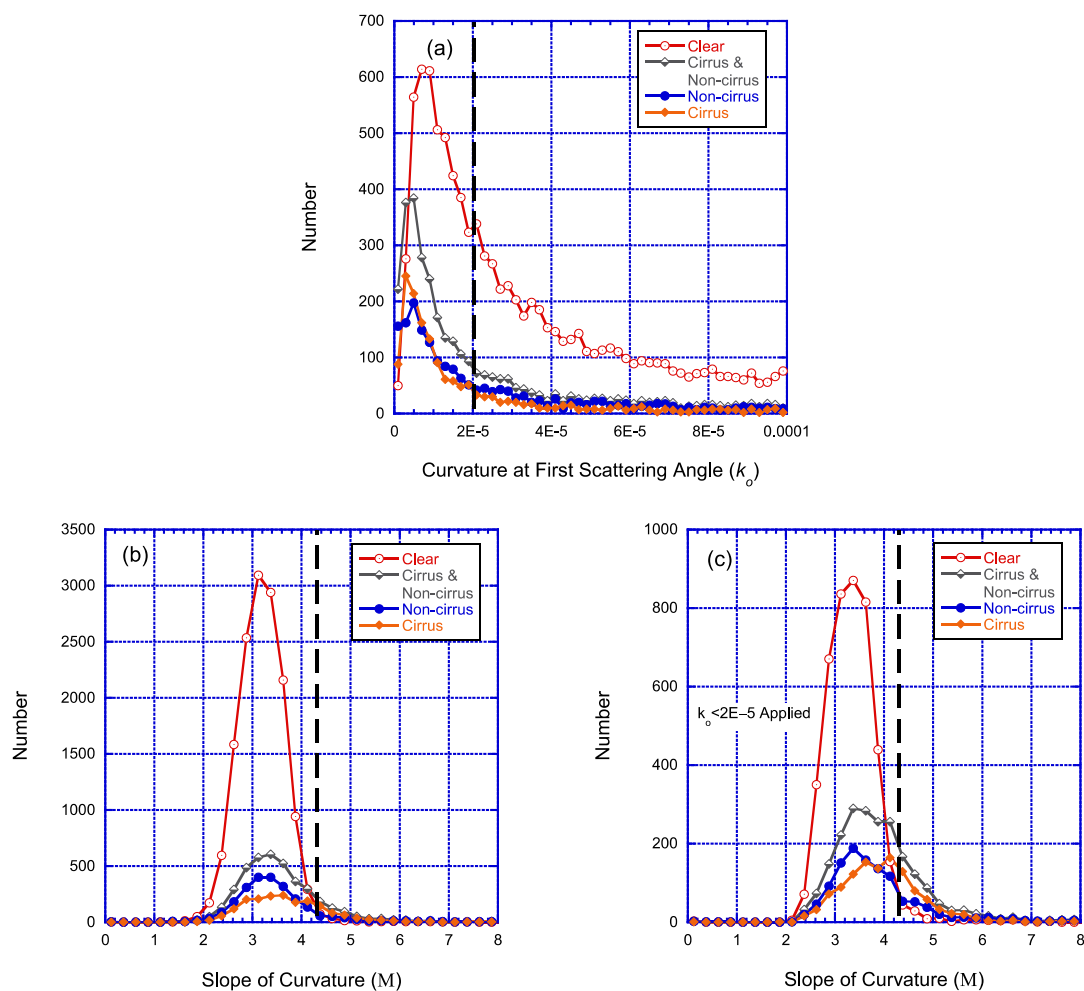


Figure 6. Similar to Fig. 4, except for SEDE BOKER (30.85° N, 34.78° E) from 2007–2013.

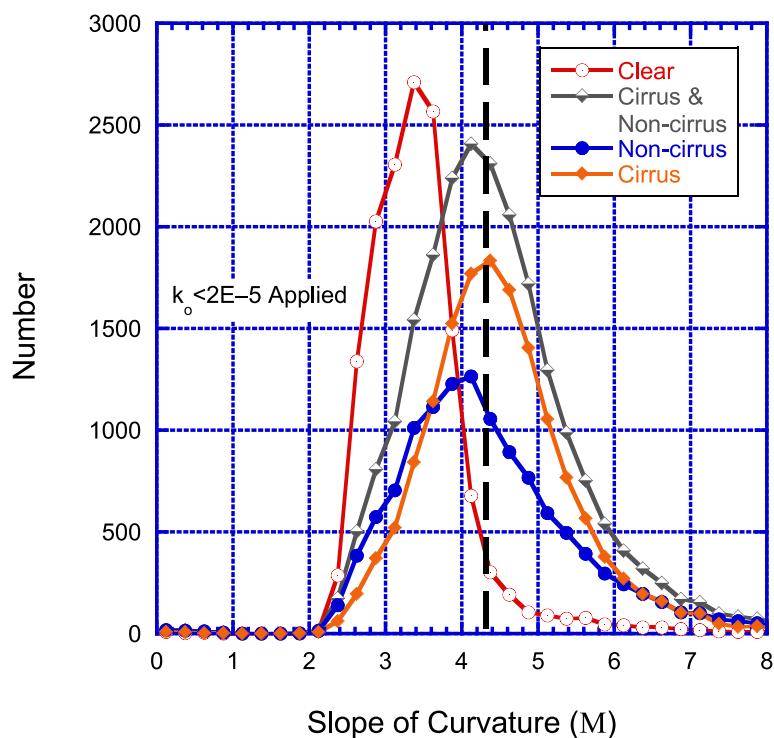


Figure 7. Similar to Fig. 4c including all analyzed sites in Table 3.

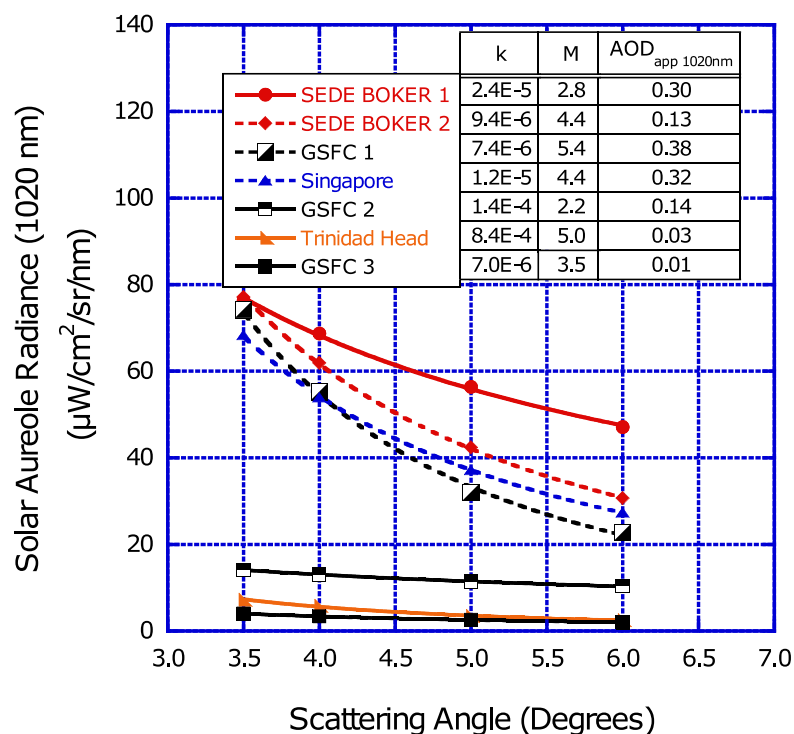


Figure 8. The solar aureole 1020nm radiance versus the scattering angle in degrees for selected sites. Data plots with the dashed lines (i.e., SEDE BOKER 2, GSFC 1, and Singapore) all qualify for the removal of data due to optically thin homogeneous cloud contamination.

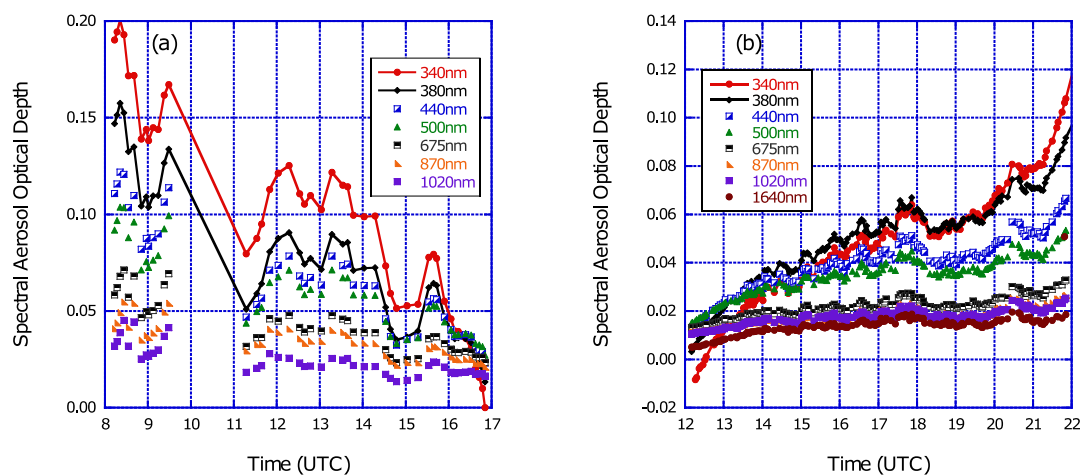


Figure 9. Time shifted aerosol optical depth (AOD) data examples at Malaga (36.72° N, 4.48° W) and Toronto (43.79° N, 79.47° W). Note the line plot is used to emphasize the 340nm and 380nm AOD impact for the time shift. (a) The Level 1.5 AOD cloud screened only data measured at the Malaga site on 30 January 2014. These data show the time shifted AOD especially at short wavelengths represent the instrument clock is too fast. (b) The Level 1.5 AOD cloud screened only data measured at the Toronto site on 24 September 2013. The time shifted aerosol optical depth especially at short wavelengths represent when the instrument clock was too slow. Panel (a) also shows the algorithm can be used with data gaps and lower temporal resolution measurement interval compared to panel (b).

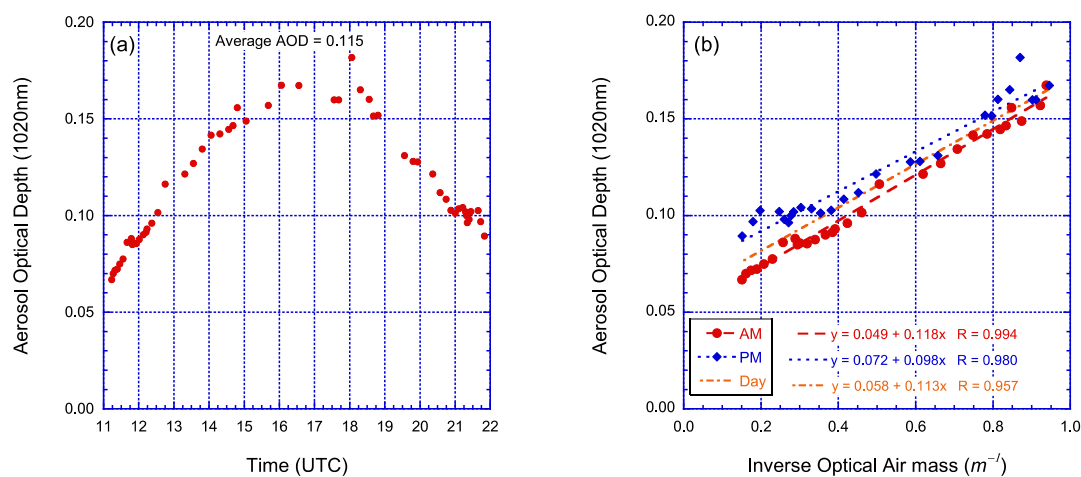


Figure 10. AERONET data collected at Rio Branco (9.96 °S, 67.87° W) on 30 August 2011. The AOD 1020nm Level 1.5 with only the cloud screening algorithm applied to the data. (a) The AOD diurnal dependence presents a concave shape during the solar day. (b) The AOD 1020nm and the inverse optical air mass show a highly correlated linear fit and the slope is significant for the full day (day) and morning (AM), and afternoon (PM). Data separation for AM and PM is defined by the local solar noon, which is 16:31:28 UTC at Rio Branco.

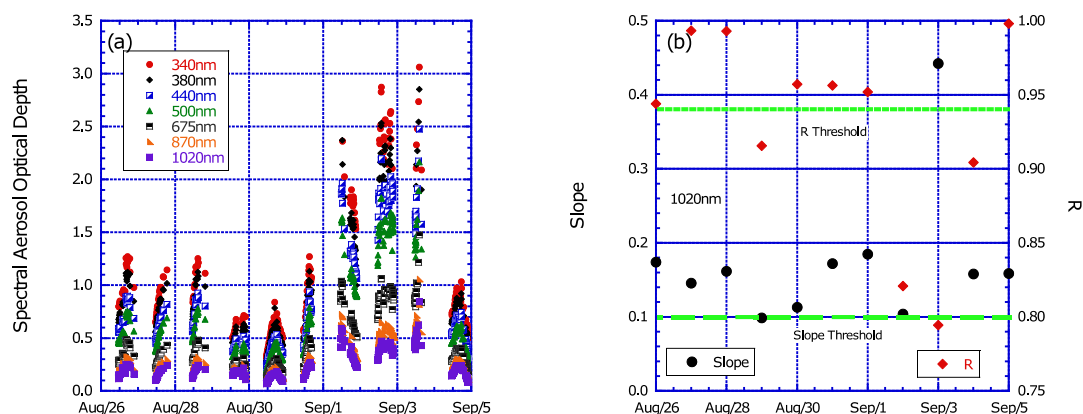


Figure 11. AERONET data collected at Rio Branco (9.96° S, 67.87° W) from 15 August to 30 September 2011. (a) The time series of Level 1.5 spectral AOD (cloud screened only) data is plotted from 26 August to 5 September 2011 and shows repeated diurnal dependence for varying magnitudes of AOD. (b) The robust linear fit slope and correlation coefficient (R) is calculated from the AOD 1020nm versus the inverse of the optical air mass (m^{-1}). For the full day evaluation, the green dashed line indicates the threshold for the slope parameter at 0.1 and the solid green line indicates the threshold for the correlation coefficient ($R = 0.94$). Both the slope and R must exceed these thresholds for at least three days scanning from the current day to the last occurrence within the 20-day period to remove the spectral AOD, and in this circumstance, all of the data are removed for the period for Levels 1.5 and 2.0.

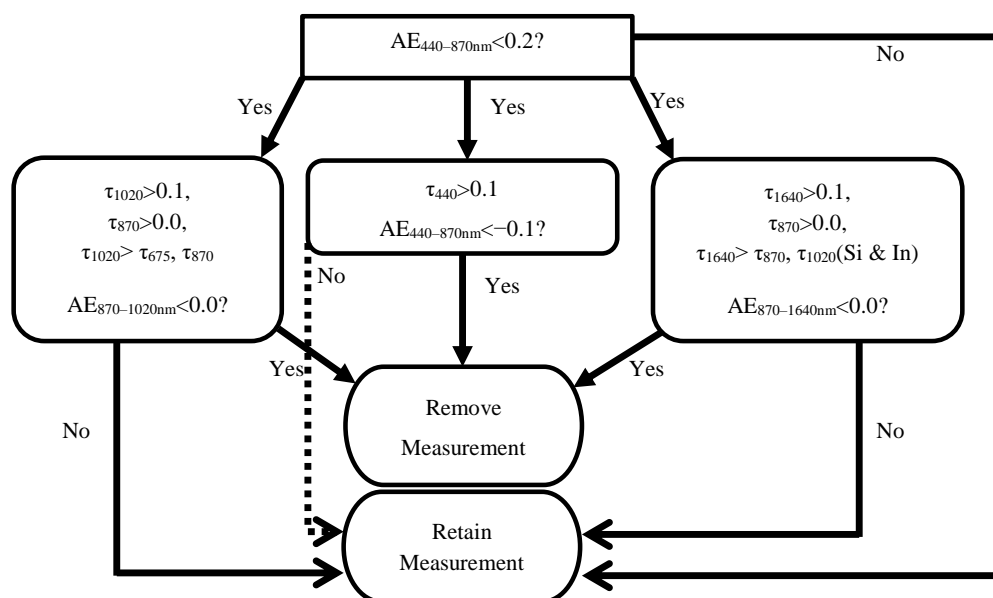


Figure 12. Flowchart of the reverse spectral dependence algorithm used to remove cloud contamination artifacts and instrument anomalies. The 1640nm wavelength is available on some Cimel Model 5 instruments and all Model T instruments.

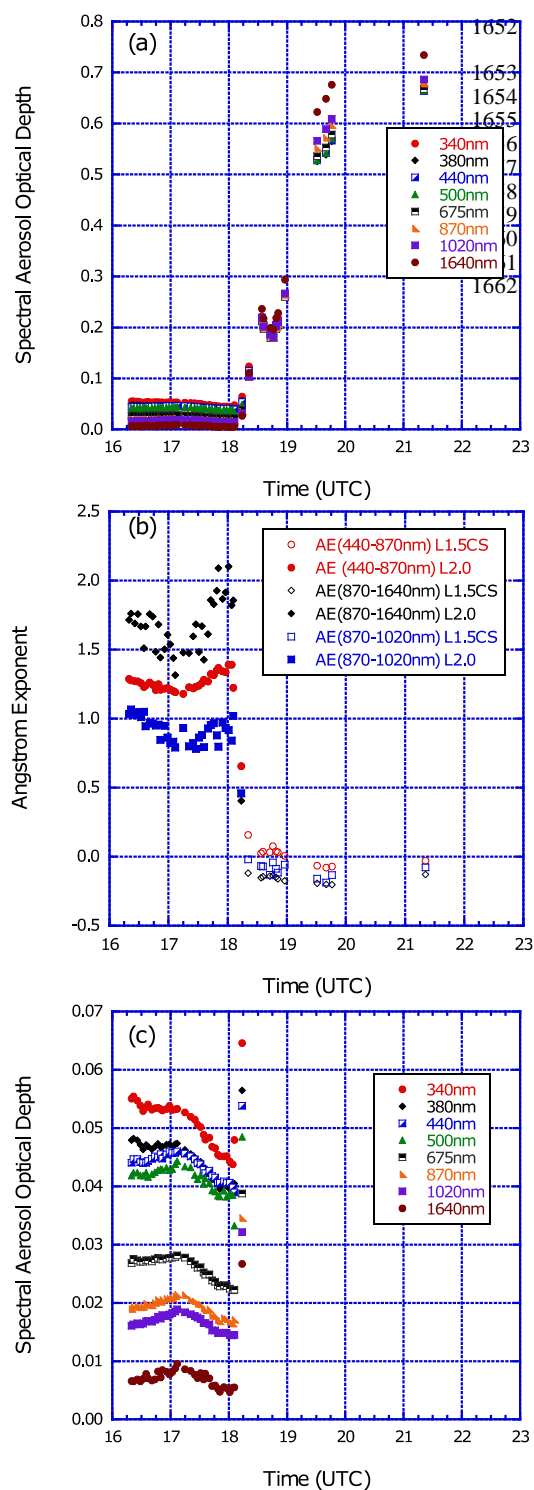


Figure 13. Data from Bratts Lake (50.20° N, 104.71° W) on 7 January 2007. **(a)** The Level 1.5 data with only the cloud screening (CS) algorithm applied shows cloud contaminated data remain after 18:10 UTC. **(b)** For the same period as (a), the Ångström exponent values decreased significantly to a level where coarse mode aerosol particles are not expected. **(c)** The final Level 1.5 and Level 2.0 data series after the reverse spectral dependence quality control or additional cloud screening method has been applied to the standalone Level 1.5 CS data.

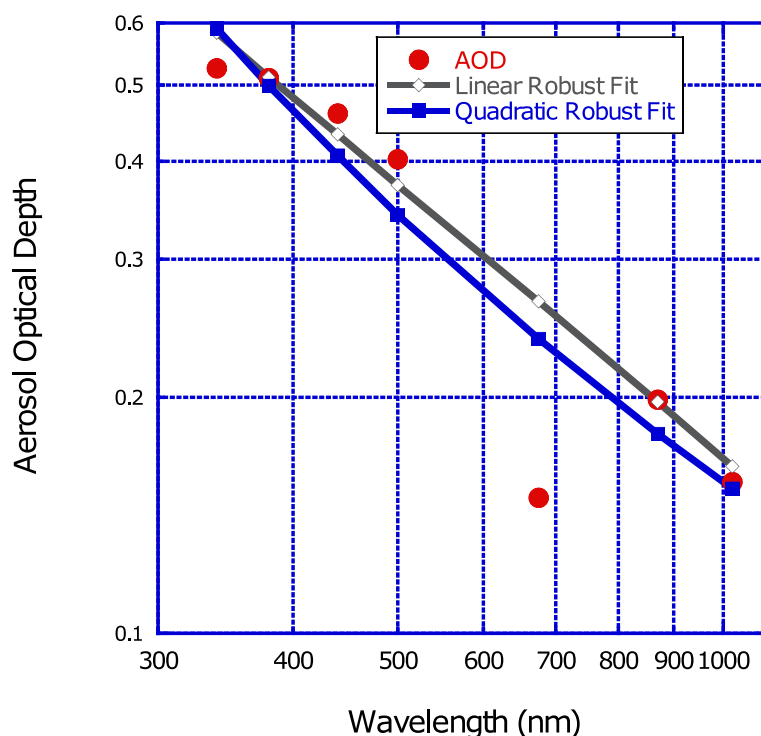


Figure 14. AERONET data from the Osaka (34.65° N, 135.59° E) site on 16 October 2006 at 22:02:11 UTC. The plot shows AOD versus the wavelength with lines identifying the linear and quadratic robust regression fits on logarithmic scale used by the AOD spectral dependence algorithm. The 675nm channel is clearly anomalous with fits differing by 0.12 for linear and 0.09 for quadratic. In addition, the AOD 340nm appears anomalous with deviations of 0.06 from linear fit and 0.07 from quadratic fit. While both wavelengths exceed their respective AOD thresholds (0.023 for 675nm and 0.051 for 340nm), the algorithm determines the maximum deviation for linear and quadratic fits and removes the AOD 675nm measurement. A subsequent scan by the algorithm determined that the remaining AOD measurements from 340nm to 1020nm were within the established fit deviation thresholds.

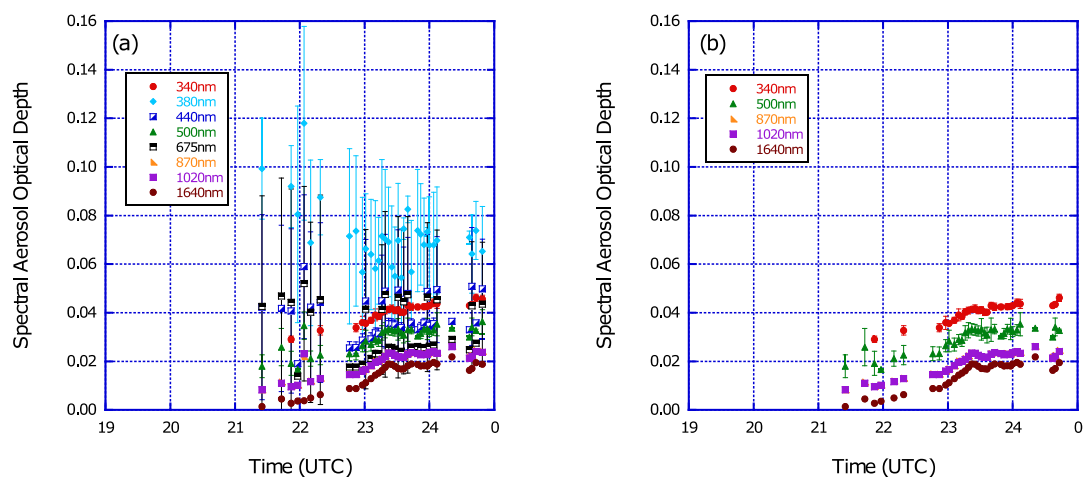
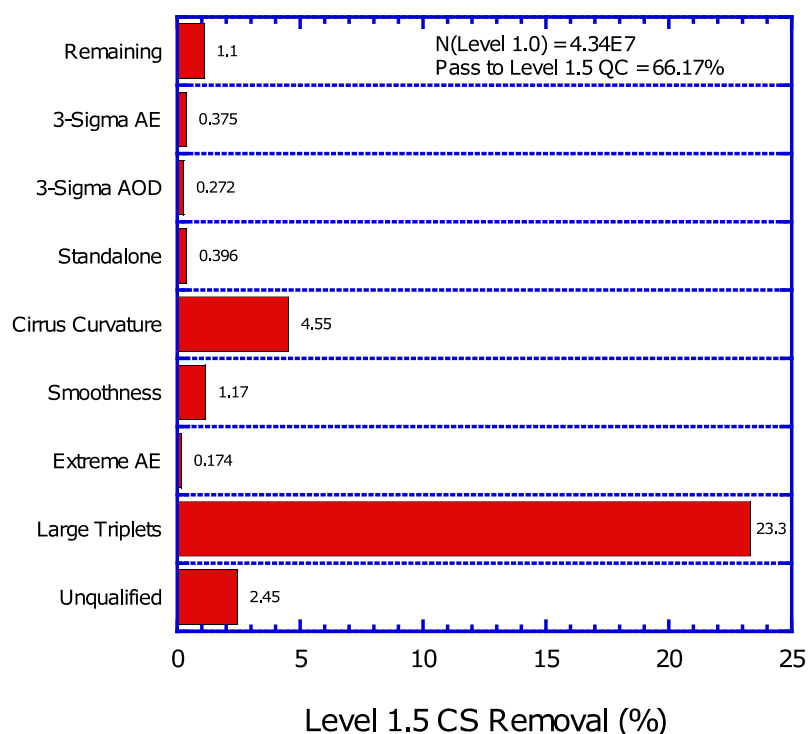


Figure 15. Spectral AOD exhibiting large triplet variability at PEARL (80.05° N, 86.42° W) on 25 August 2013. **(a)** Version 3 Level 1.5 cloud screened only data is plotted with large triplet variability and these data were not removed by the cloud screening. The error bars represent the triplet variability (AOD Max – AOD Min) divided by 2 so the full range represents the AOD triplet variability. The large triplet variability occurs mainly at shorter wavelengths than 675nm. **(b)** Data affected by large triplet variability (i.e., AOD 380nm, AOD 440nm, and AOD 675nm) are removed by using the Level 1.5 large triplet variability quality controls.



1681



1682

1683 **Figure 16.** The Level 1.0 AOD measurement removal by the Level 1.5 cloud screening algorithm from 1993 to 2018. The plot
 1684 shows the impact of the major cloud screening steps in the Level 1.5 cloud screening algorithm and removal of these data applies
 1685 to all wavelengths. The triplet criterion removes more than 23% of the Level 1.0 data. Nearly 5% of the Level 1.0 data are
 1686 removed due to cirrus cloud contamination. The “Remaining” category indicates the check performed after each cloud screening
 1687 step to determine if enough measurements are available and do not meet the high AOD retention criteria. The “Unqualified”
 1688 category indicates data that are negative or lack sufficient channels to participate in the cloud screening algorithm.

1689

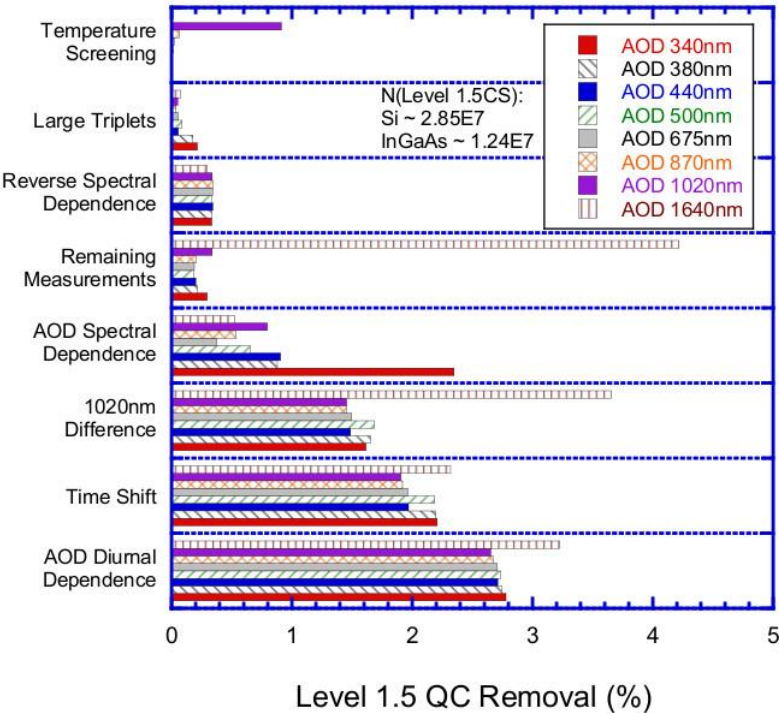


Figure 17. Level 1.5 quality control algorithm wavelength dependent impacts for each major step for the period analyzed from 1993–2018. The most significant removal for most channels is due to AOD diurnal dependence, time shift, and difference between AOD 1020nm on the Silicon and InGaAs detectors (resulting from collimator inconsistency). The AOD 340nm has significant removal of AOD spectral dependence. The 1640nm InGaAs channel has significant removal by “Remaining Measurements” since this wavelength cannot be checked for quality when the Silicon channels are not available. Temperature screening mostly applies to the 1020nm Silicon wavelength due to its strong temperature dependence near the edge of the signal sensitivity of the Silicon photodiode detector.

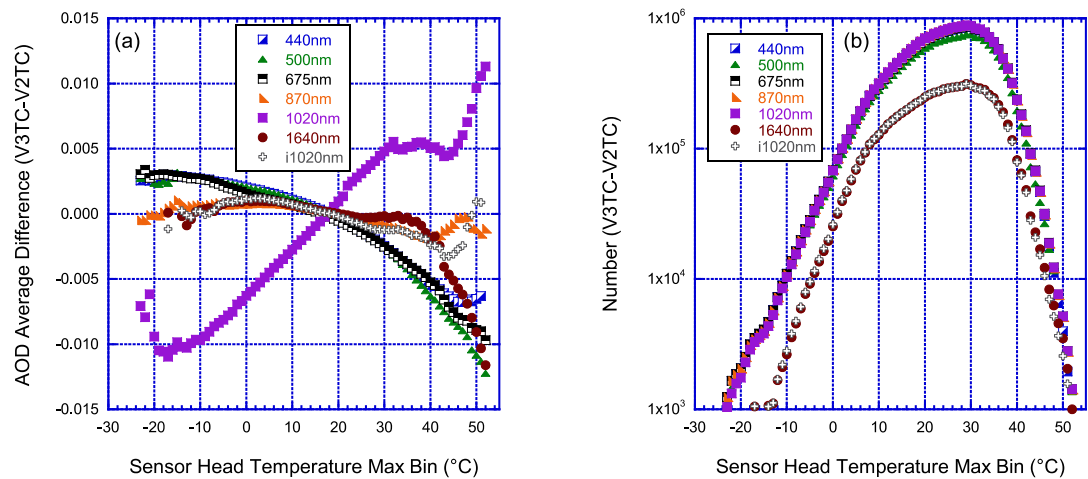


Figure 18. Difference in AOD response between Version 3 and Version 2 temperature correction applied to Version 3 AOD data based on the sensor head temperature from 1993–2018. The Version 2 temperature correction assumes temperature ranges for 1020nm and no temperature correction for all other wavelengths, while Version 3 temperature correction characterizes the temperature response for each filter or set of default filters for each instrument for wavelengths $\geq 400\text{nm}$. (a) The AOD average difference plotted for each 1°C temperature bin from -25°C to $+55^\circ\text{C}$. The AOD 1020nm exhibits an opposite trend compared to the other wavelengths varying from -0.01 at low temperatures and up to $+0.01$ at high temperatures. Other wavelengths have slight differences at cold temperatures but apparent dependencies at high temperatures greater than 40°C possibly due to extrapolation of the temperature coefficients to higher temperatures. (b) The number of measurements plotted for each 1°C temperature bin with a minimum of 1000 observations.

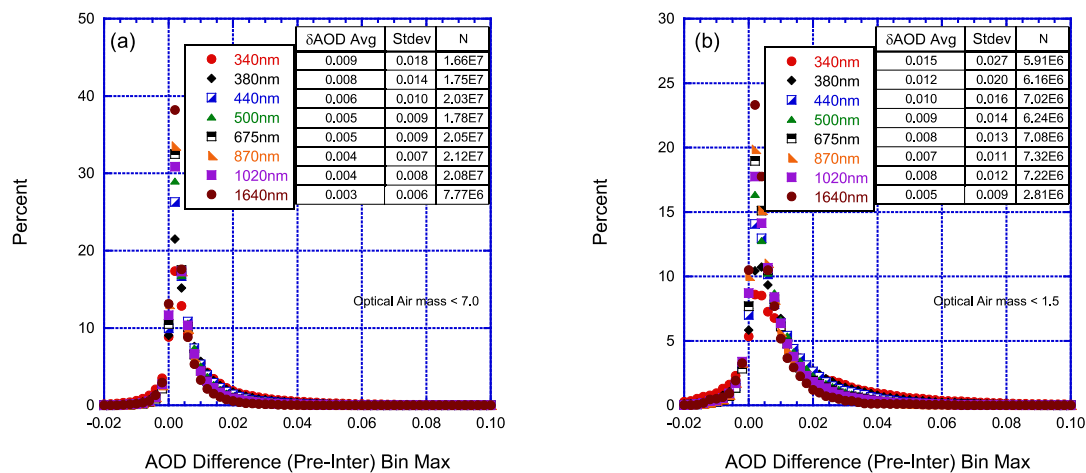


Figure 19. Using data qualified as Version 3, Level 2.0, aerosol optical depth (AOD) average difference comparing measurements only with the pre-field calibration applied versus instruments with both the pre-field and post-field calibrations applied from 1993–2018. Calibration sites are excluded from the analysis. The histogram of AOD differences is provided for the optical air mass $1.0 \leq m < 7.0$ range in panel (a) and $1.0 \leq m < 1.5$ range in panel (b). The average difference is largest for the UV wavelengths and smallest for the longer wavelengths.

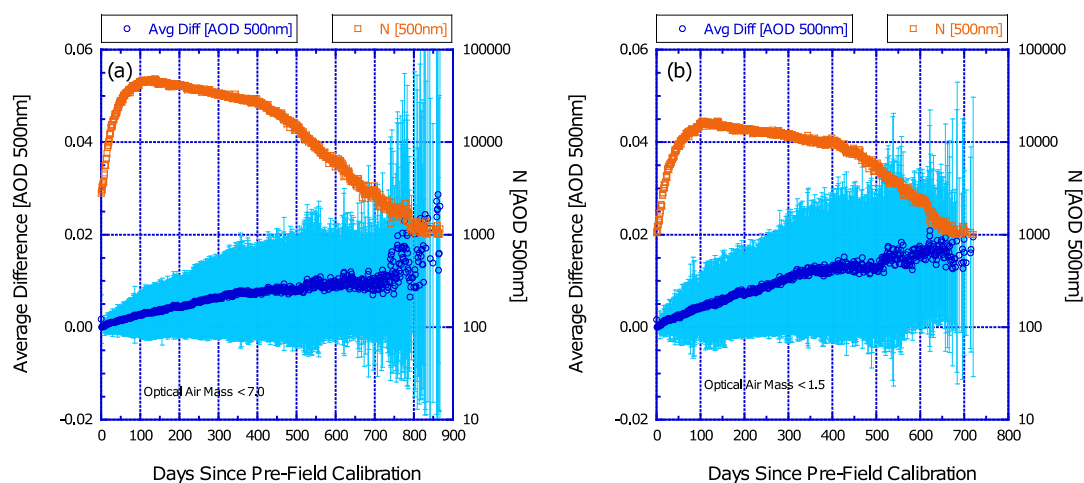


Figure 20. Using data qualified as Version 3 Level 2.0 aerosol optical depth (AOD) 500nm average difference comparing measurements only with the pre-field calibration applied versus instruments with both the pre-field and post-field calibrations applied from 1993–2018. The AOD average differences are provided for the optical air mass $1.0 \leq m < 7.0$ range in panel (a) and $1.0 \leq m < 1.5$ range in panel (b). Vertical bars represent the standard deviation for each day bin. The secondary y-axis in logarithmic scale represents the number of measurements of AOD 500nm for each day bin.

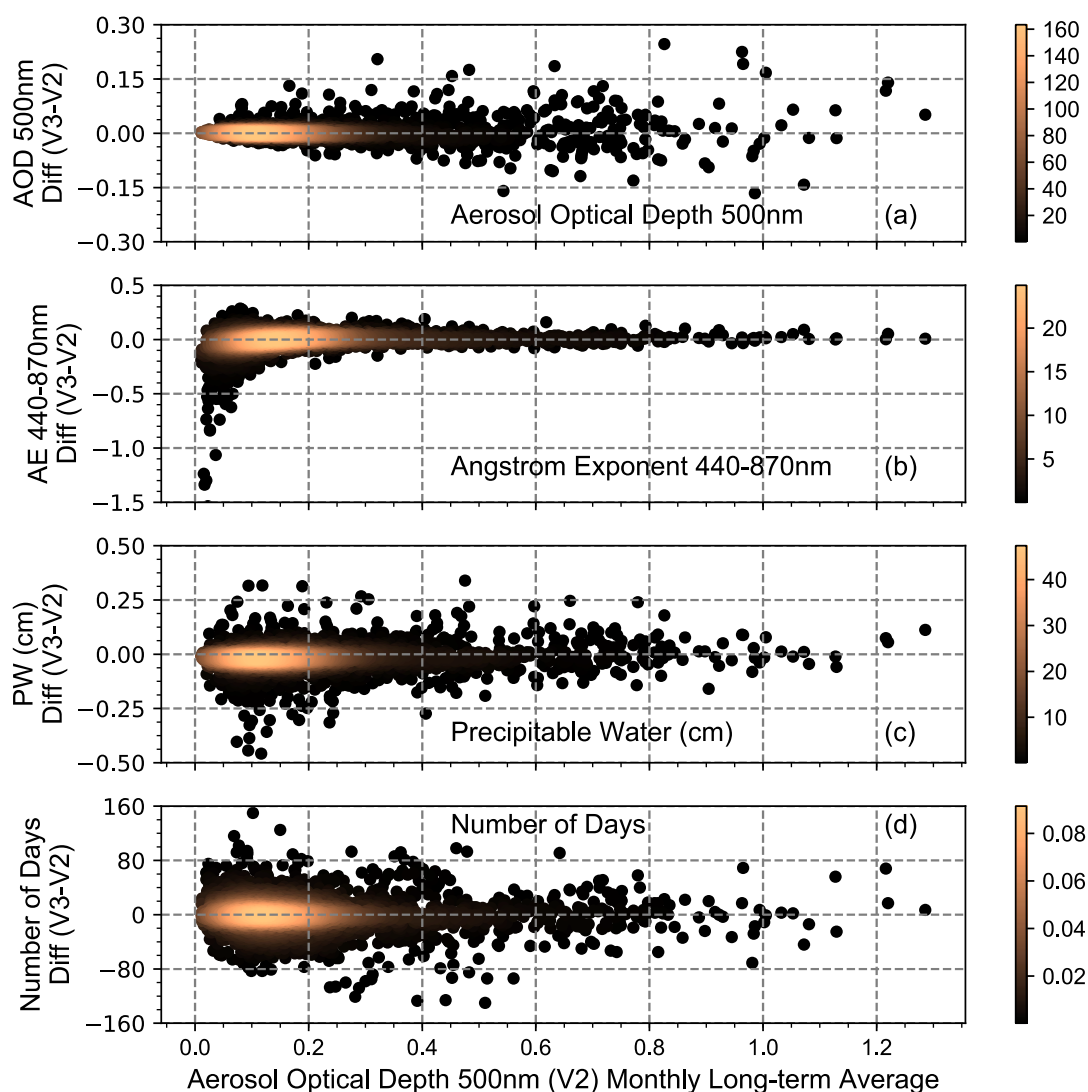


Figure 21. Comparison of Version 3 and Version 2 Level 2.0 multi-year monthly average data sets. (a) The aerosol optical depth (AOD) interpolated to 500nm to include data from instruments without 500nm. (b) The Ångström exponent (AE) is calculated utilizing the inclusive ordinary least squares regression fit from 440–870nm. (c) The precipitable water in cm is derived from the 935nm water vapor channel. (d) The difference in the number of days is determined for each monthly long-term average.

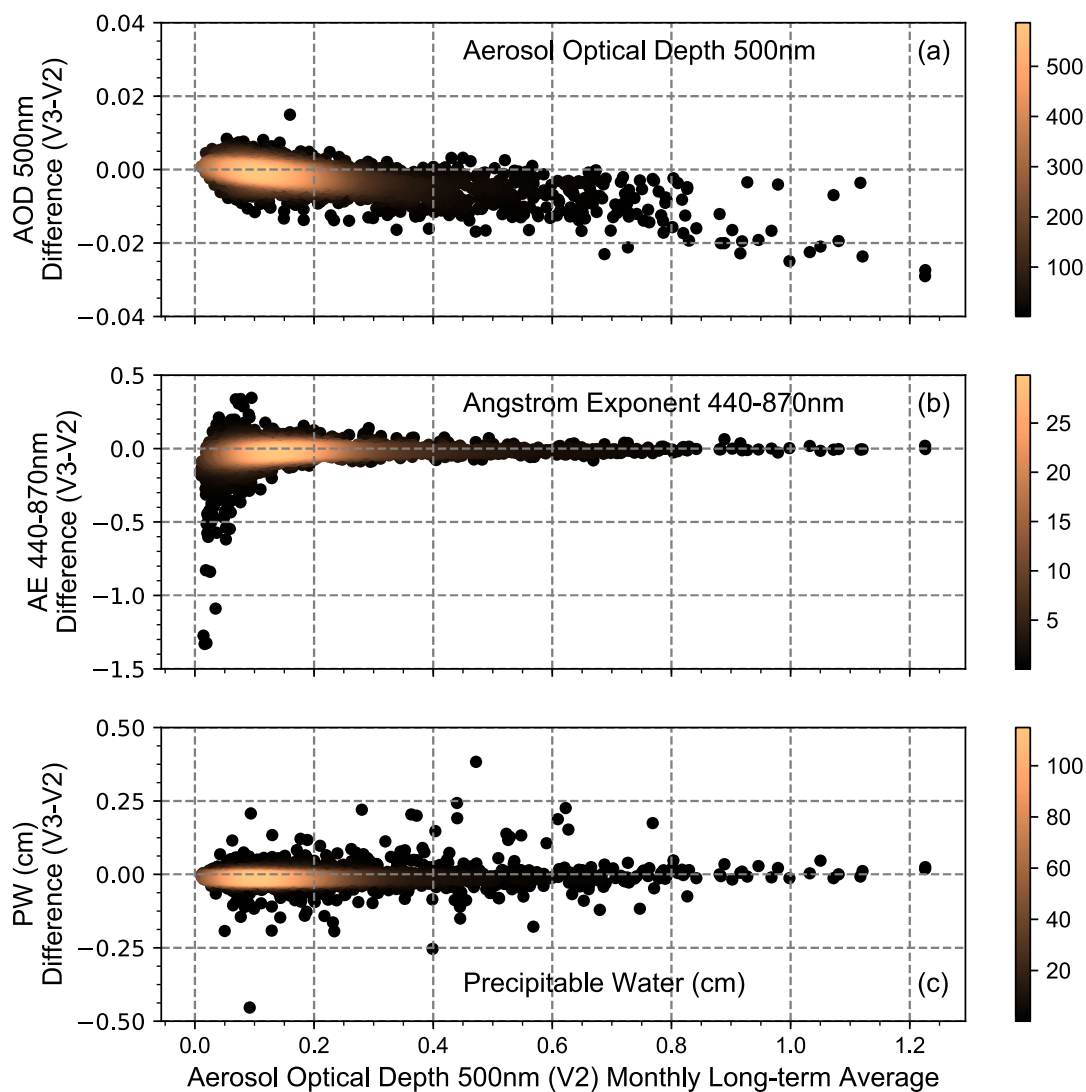


Figure 22. Comparison of Version 3 and Version 2 Level 2.0 multi-year monthly average data sets for time matched instantaneous observations in both data sets. The panels are similar to those in Fig. 21.

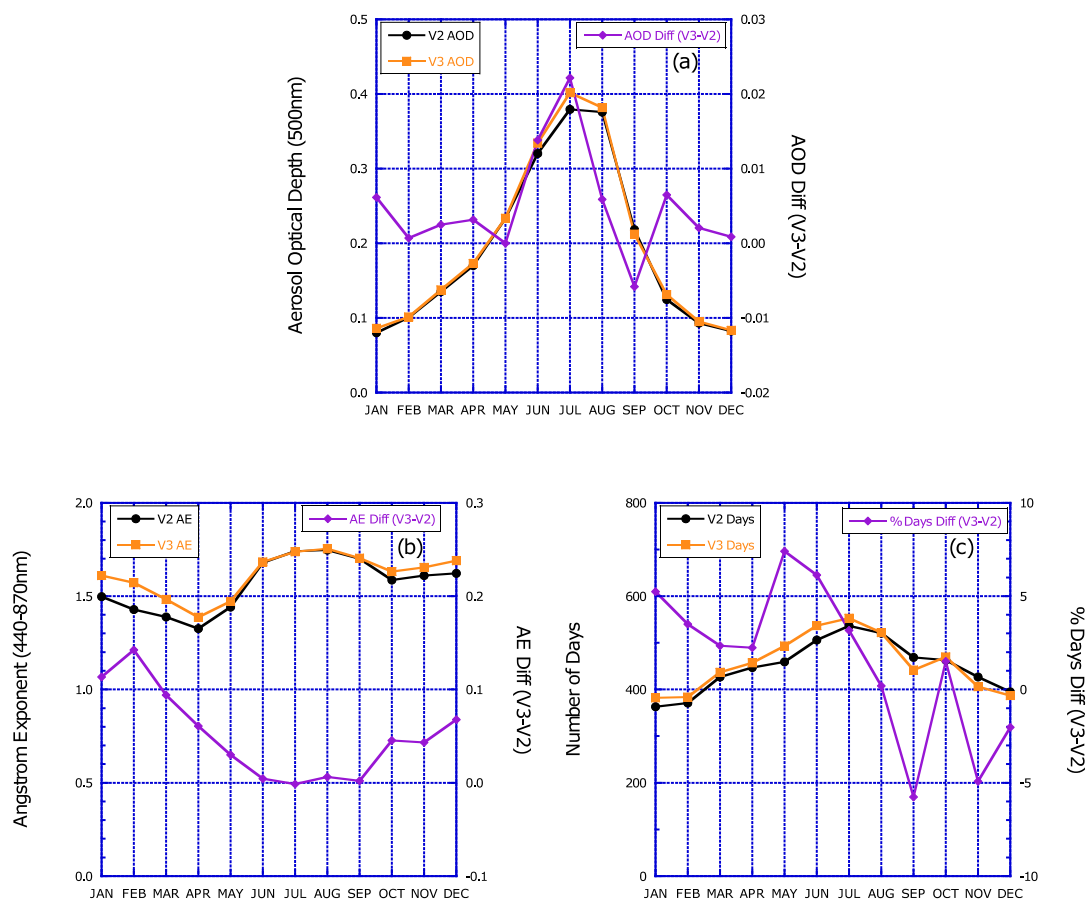


Figure 23. Long-term multi-year (1993–2016) monthly average comparisons of the Version 3 and Version 2 Level 2.0 data sets at the NASA Goddard Space Flight Center (GSFC), Maryland, USA. The panel (a) provides the AOD interpolated to 500nm for each version on the primary y-axis and differences on the secondary y-axis. The panels (b) and (c) are plotted similarly for the AE_{440–870nm} and the number of days in the multi-year monthly average, respectively.

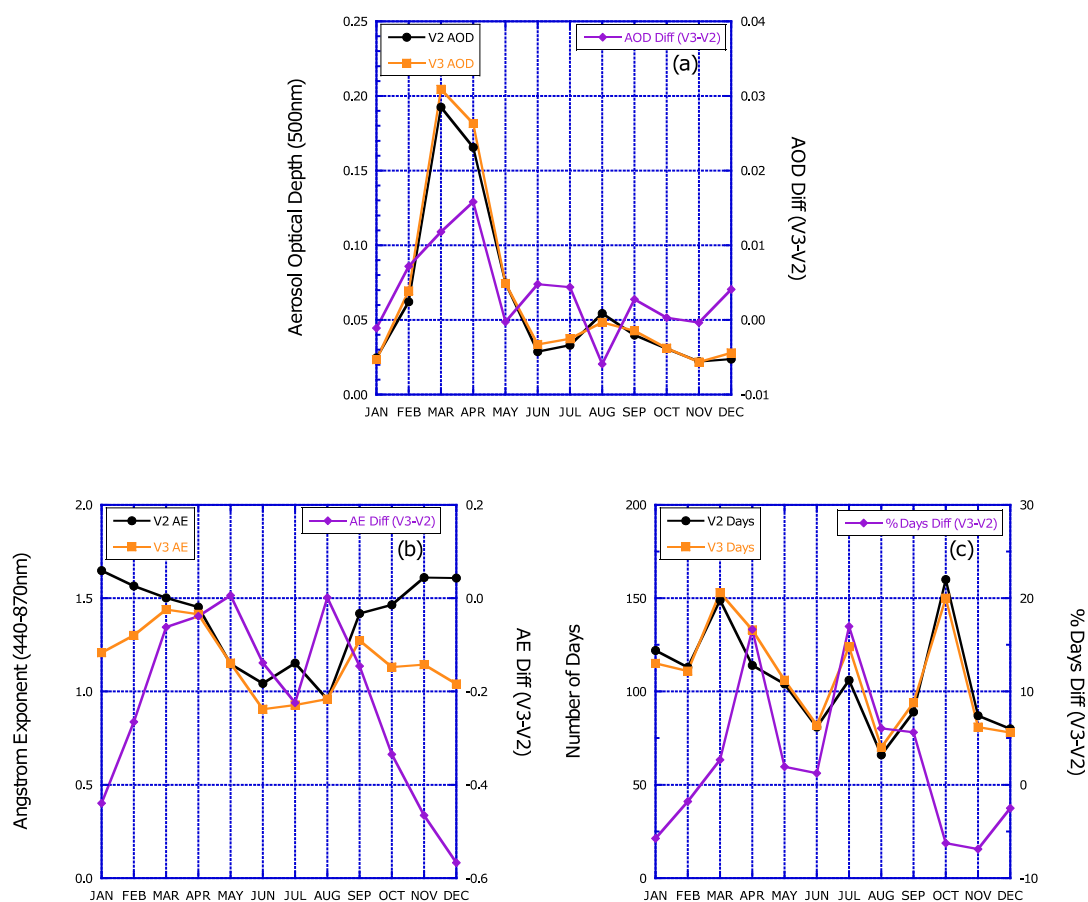


Figure 24. Similar to Fig. 23 except for Lulin, Taiwan (23.47° N, 120.87° E) from 2006–2017.

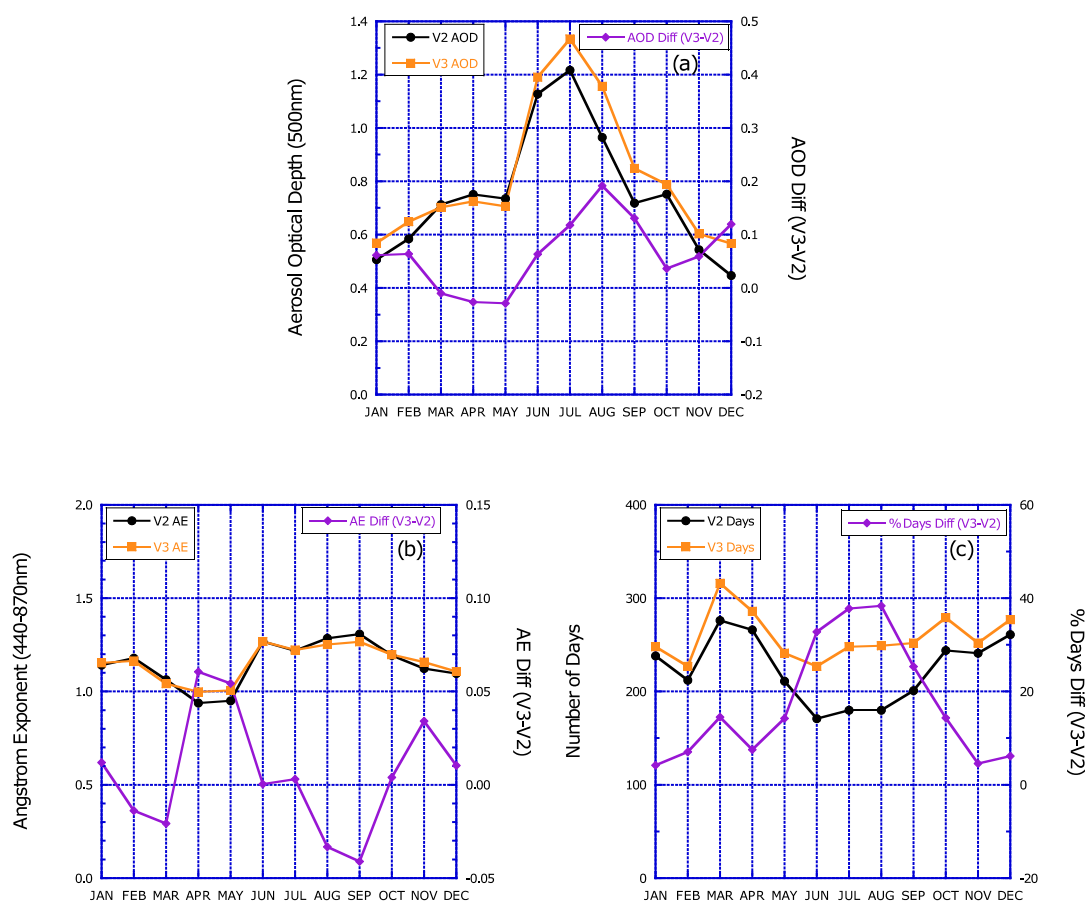


Figure 25. Similar to Fig. 23 except for XiangHe, China (39.75° N, 116.96° E) from 2001–2017, except 2009.

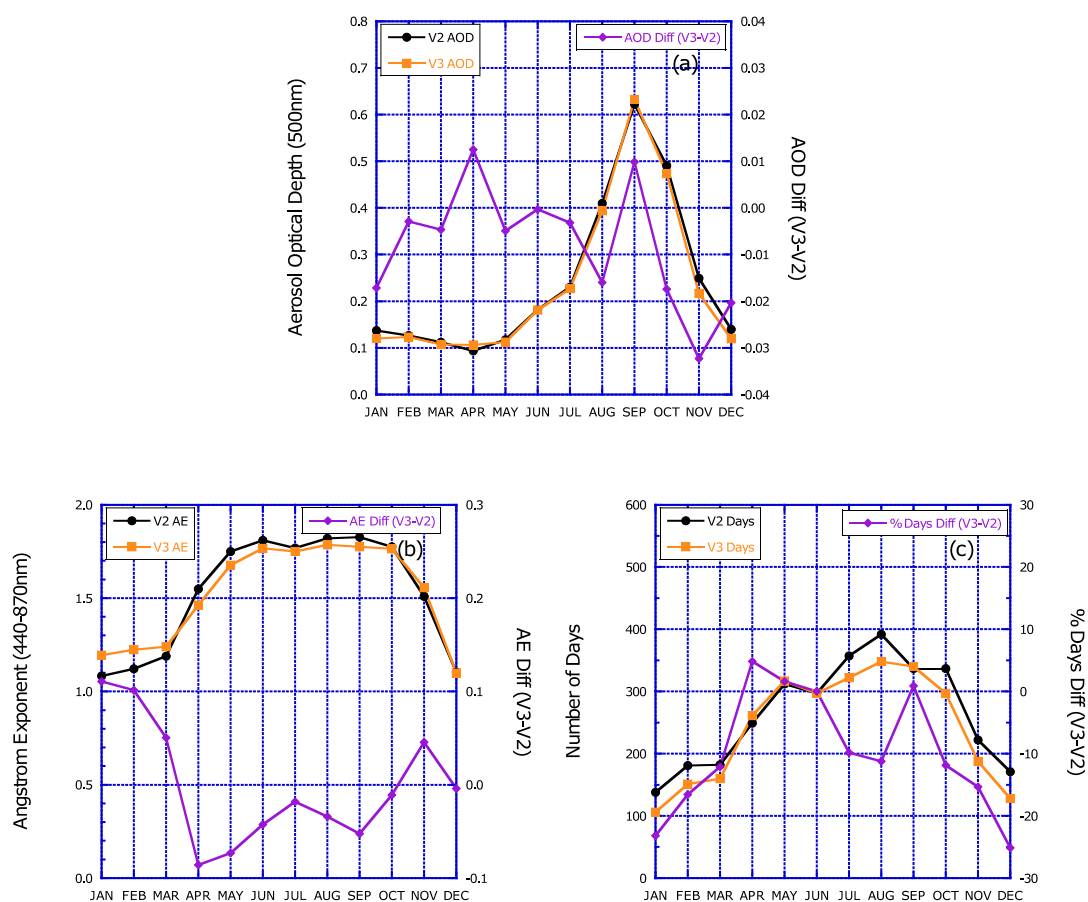


Figure 26. Similar to Fig. 23 except for Mongu, Zambia (15.25° S, 23.15° E) from 1997–2010.

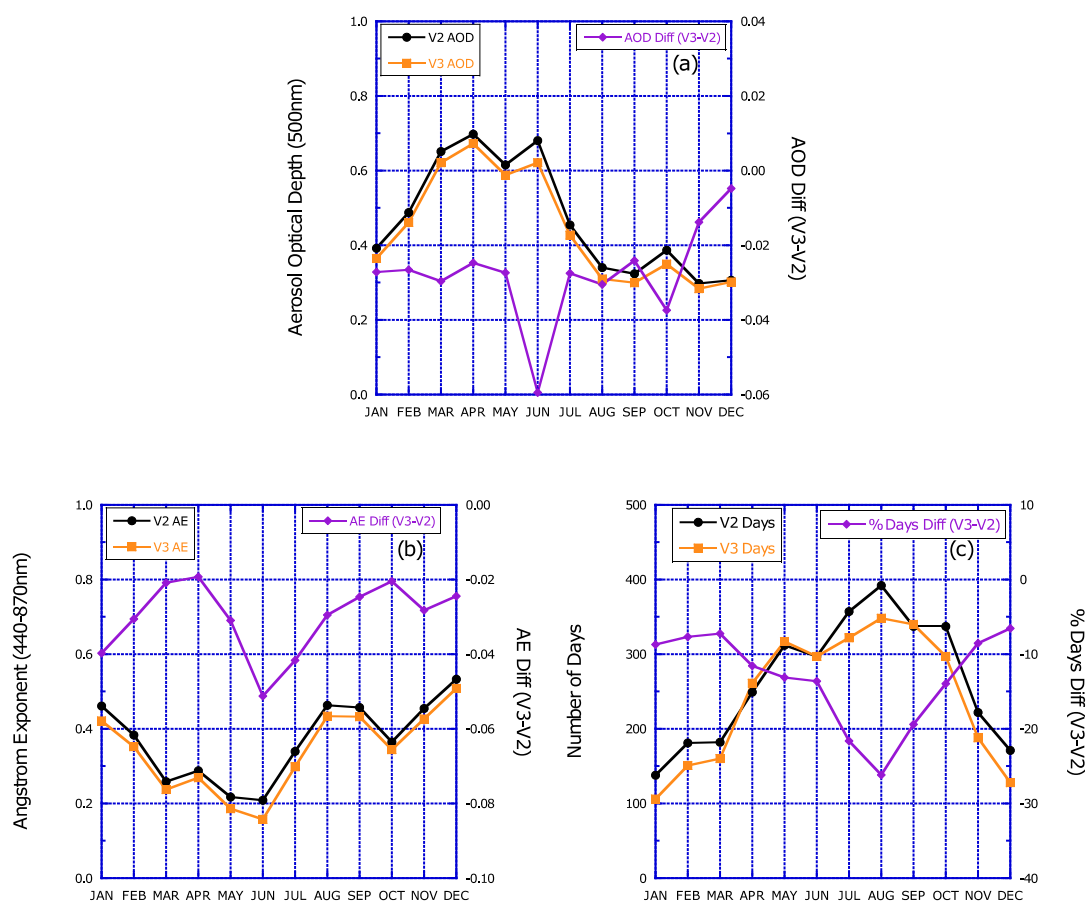


Figure 27. Similar to Fig. 23, except for IER-Cinzana, Mali (13.28° N, 5.93° W) from 2004-2017.